ELECTRONIC STRUCTURE OF LANTHANUM HYDRIDE AND ZIRCONIUM NITRIDE MOLECULES AND RADIATIVE LIFETIME MEASUREMENTS IN La ATOM

By

SURESH YARLAGADDA

(PHYS01200904018)

Bhabha Atomic Research Centre, Mumbai

A thesis submitted to the Board of Studies in

Physical Sciences

In partial fulfillment of requirements

For the Degree of

DOCTOR OF PHILASOPHY

OF

HOMI BHABHA NATIONAL INSTITUTE

January, 2015

Homi Bhabha National Institute

Recommendations of the Viva Voce Committee

As members of the Viva Voce committee, we certify that we have read the dissertation prepared by **Mr. Suresh Yarlagadda** entitled **“Electronic structure of lanthanum hydride and zirconium nitride molecules and radiative lifetime measurements in La atom.”** and recommend that it may be accepted as fulfilling the thesis requirement for award of Degree of Doctor of Philosophy.

Chairman - Prof. B.N. Jagatap Date: 25/05/2015

Guide / Convener – Prof. S.G. Nakhate Date: 25/05/2015

K. Viswanathan 25/5/15

Examiner-Prof. K.S. Viswanathan Date: 25/05/2015

Member – Prof. T. Kundu Date: 25/05/2015

Member – Prof. K.G. Manohar Date: 25/05/2015

Final approval and acceptance of this thesis is contingent upon the candidate’s submission of the final copies of the thesis to HBNI.

I hereby certify that I have read this thesis prepared under my direction and recommend that it may be accepted as fulfilling the thesis requirement.

Date: May 25, 2015

Place: Mumbai

Prof. S. G. Nakhate

STATEMENT BY AUTHOR

This dissertation has been submitted in partial fulfillment of requirements for an advanced degree at Homi Bhabha National Institute (HBNI) and is deposited in the Library to be made available to borrowers under rules of the HBNI.

Brief quotations from this dissertation are allowable without special permission, provided that accurate acknowledgement of source is made. Requests for permission for extended quotation from or reproduction of this manuscript in whole or in part may be granted by the Competent Authority of HBNI when in his or her judgment the proposed use of the material is in the interests of scholarship. In all other instances, however, permission must be obtained from the author.

Suresh Yarlagadda

DECLARATION

I, hereby declare that the investigation presented in the thesis has been carried out by me. The work is original and has not been submitted earlier as a whole or in part for a degree / diploma at this or any other Institution / University.

Suresh Yarlagadda

List of publications included in the thesis

Journals:

1. "Radiative lifetime measurements in neutral lanthanum using time-resolved laser-induced fluorescence spectroscopy in supersonic free-jet",

Suresh Yarlagadda, Sheo Mukund, S.G. Nakhate, *J. Opt. Soc. Am. B* **28** ,1928 (2011).

2. "Jet-cooled laser-induced fluorescence spectroscopy of LaH: Observation of new excited electronic states",

Suresh Yarlagadda, Sheo Mukund, S.G. Nakhate, *Chem. Phys. Lett*. **537**, 1 (2012).

3. "Energy linkage between the singlet and triplet manifolds in LaH, and observation of new low-energy states",

Sheo Mukund, **Suresh Yarlagadda**, Soumen Bhattacharyya, S. G. Nakhate, *J. Chem. Phys*. **137**, 234309 (2012).

4. "Observation of a new Ω=1 excited state in LaH",

Suresh Yarlagadda, Sheo Mukund, Soumen Bhattacharyya, S.G. Nakhate, *J. Mol. Spectrosc*. **289**, 1 (2013).

5. "Observation of two $\Omega=0^+$ excited states of jet cooled LaH",

Suresh Yarlagadda, Sheo Mukund, Soumen Bhattacharyya, S.G. Nakhate, *J. Quant. Spectrosc. Radiat. Transfer*. **145**, 17 (2014).

6. "Extended analysis of the $B^2\Sigma^+$-$X^2\Sigma^+$ and $A^2\Pi$-$X^2\Sigma^+$ systems of ZrN",

Soumen Bhattacharyya, Sheo Mukund, **Suresh Yarlagadda,** S.G. Nakhate, *J. Quant.Spectrosc. Radiat. Transfer*. **148**, 13 (2014).

Conferences/Symposia:

1. “Radiative lifetime measurements in neutral lanthanum using time-resolved laser-induced fluorescence in supersonic free-jet”,

Sheo Mukund, **Suresh Yarlagadda**, Soumen Bhattacharyya, S.G. Nakhate; proceedings in DAE-BRNS Symposium on Atomic, Molecular and Optical Physics (AMOP-2011)) held at Karnatak University, Dharwad during February 22-25, 2011, Pg. 56.

2. “Observation of two $\Omega = 0^+$ excited electronic states in the jet-cooled LaH”,

Suresh Yarlagadda, Sheo Mukund, Soumen Bhattacharyya, S.G. Nakhate; proceedings in 69th meeting on International Symposium on Molecular Spectroscopy (ISMS) held at University of Illinois at Urbana-Champaign, during June 16-20, 2014 Pg. 145.

Suresh Yarlagadda

Dedicated to……………..

My Beloved Family and

My Teachers

ACKNOWLEDGEMENT

First and foremost I would like to express my deep and sincere gratitude to my supervisor Prof. S.G. Nakhate for his invaluable guidance, constant encouragement, unstinted inspiration, keen interest and good wishes. His ability to explain things simply and clearly are something I have admired right from my first day in lab, and continue to remain in awe even today. I greatly appreciate his contributions, comments and insights during the course of writing this Thesis. His patience and support has helped me get through some challenging moments. For this, and much more, I remain indebted.

I must thank to Dr. Somen Bhattacharyya and Mr. Sheo Mukund for their innumerous help during the experiments and data analysis and their suggestions even in my personal life. Without their continuous support I could not be much happy during the course of time. I would like to express my sincere thanks to my doctoral committee members, Prof. B.N. Jagatap, Prof. T. Kundu and Prof. K.G. Manohar for their critical comments and suggestions during annual review presentations.

I would like to express my sincere thank to Dr. N.K. Sahoo, who used to always give suggestions whenever I met him and his incredible support, ceaseless encouragement and enthusiasm about my research. I take the opportunity to express my heartful thanks to Dr. Manoj, Dr. A.P. Mishra, Dr. Kshirsagar, Dr. Aparna, Dr. Uduppa, Dr. D. Bhattacharyya, Dr. Sunanda and Dr. Pushpa Rao for their suggestions and support during my course of research.

I wish to show my sincere gratitude to Prof. R. Shanker, who motivated me to choose the research career in field of Spectroscopy. I would like to thanks my school teachers Sri V.S.S.R. Anjaneyulu, Sri A. Srinivas and Sri Ramarao who motivated me to pursue higher studies from my childhood onwards. It would be very difficult for me coming from a farmer family of a remote village to this stage, without their continuous encouragement and support. I am immensely indebted and express my deep sense of gratitude and heart full thanks to all my teachers, who have added different dimensions to my life at different stages.

My special thanks go to my childhood friends Anil, Kantharao, Seshu, M.N.R, Raheem, Venu, Narasimharao, Pushpa, Kittu and Rani for their support and cooperation in various aspects and cheered me up during difficult times. I also thank all my M.Sc friends especially Avinash, Prasad, Vinay, lokesh and Anuradha, who have always encouraged me in all aspects.

I would like to express my heartful thanks to my best friend Rajesh for his support, encouragement and constructive criticism during my research work. He is the one who always make fun with me. I would like to express my sincere thanks to Hajarudhin, who is good well wisher of me and helped financially during my M.Sc time.

Words fail me to express my appreciation to my roommate Dilip who shared all my thoughts, sorrows, happiness and frustrations. He made me all time cheer and confident. I would like to express my sincere thanks to my all other roommates Venky, Rajamoorthy, Ahmed, Abdulla, Khaisar, Kamal, GM and Suma, Yusuf and Jasna, Vivek and Anju, Satish and Anusha and Naresh and Vani for their unwavering support during my difficult time and homely feeling at Mumbai. I always cherish the time spent with all of you during these years. I also extend thanks to my batch mates Nitya, Mithali, Priyanka , Sohini, Soumya and Shuvendu.

I cannot begin to express my gratitude toward my parents. They have been my pillars of support and strength for as long as I can remember. I am convinced, I could not have made it this far without their love and encouragement. I am indebted to my Sister, Bhavani and my Brother-in-law and their Children for their support and encouragement. I am indebted to my would-be, Maithri, who encouraged me and supported me in every aspect right from the beginning of our relation.

Finally, I would like to thank the Department of Atomic Energy for funding my Doctoral research work.

Date: Suresh Yarlagadda

CONTENTS

Synopsis

The study of electronic structure of transition-metal containing diatomic molecules shed light on the role played by the *d* electrons in a molecular bond. However, this presents a serious challenge for both theorist and experimentalist because of the complex electronic structure arising from the partial occupation of open *d* orbital. Due to the presence of the unpaired *d* electrons in the transition metals, the molecules containing these metals tend to have high density of excited electronic states with high-spin and orbital angular momenta. Configuration interactions between these excited states result in local and global perturbations, which are often responsible for many misinterpretations of the spectra. The study of the bonding trends of the transition-metal containing diatomic molecules provide a benchmark for the theoretical chemists to test the validity of their approximations and accordingly develop robust theoretical methods capable of accurately describing the electronic structure and geometry of larger systems. Over the past decades, significant progress has been made towards understanding the nature of the chemical bond in transition-metal containing diatomic molecules [1]. On the theoretical front, new and improved methods for electronic structure calculations have been developed. These *ab initio* calculations account for configuration interaction, electron correlation, exchange and relativistic effects in their treatment which are very important for the molecules containing transition metal atoms [2]. However, on the experimental front, the study of diatomic molecules has been benefitted from the numerous developments made in the recent past. Prior to the development of lasers and molecular beam techniques, emission or absorption spectra recorded on photographic plate served as the main source of spectroscopic data. Conventionally, the metals were vaporized in high temperature ovens, and were allowed to react with various gases to form the desired molecular species [3].

Thus due to the high temperature conditions necessary for metal vapour production, the obtained molecular spectra were often complex and congested which many times led to misleading assignments [4-6]. The application of laser radiation sources in the 1970's led to revolutionary developments in the field of molecular spectroscopy. The high spectral resolution and sensitivity brought about by the advent of laser sources allowed investigation of subtle and intricate structures present in the spectra of molecules, even at very low concentrations. The development of experimental technique of laser ablation followed by supersonic expansion, creating a molecular beam of refractory material at low temperature wherein most of the population remained in few rotational levels of the ground state, simplified the spectra dramatically. This simplified spectra led to an unambiguous assignment of character of the ground and excited electronic states [7] which is very important for understanding the nature of the transition metal-main group element bond.

This thesis presents the experimental study of electronic structure of two diatomic molecules lanthanum hydride (LaH) and zirconium nitride (ZrN) in the gas phase using laser-induced fluorescence (LIF) spectroscopy. Transition-metal containing diatomic molecules play an important role in many fields, such as catalysis [8], organometallics [9], surface science [10], and astrophysics [11]. The lanthanide hydrides have recently attracted much interest due to their use in semiconducting and magnetic materials [12,13]. Lanthanide metals are also being considered as materials for hydrogen storage [14]. It is therefore important to study small lanthanide hydrides to extend our knowledge of hydrogen chemistry of these compounds. The diatomic transition metal nitrides are simple model systems for fixation of nitrogen in industrial, inorganic, and biological systems [15,16]. Transition metal nitrides also have astrophysical importance and so far have not been detected in the stellar atmospheres, partly due to the lack of precise spectroscopic data required for their meaningful search in the complex stellar spectra. Radiative lifetimes of neutral lanthanum (La I) atom are also included in this thesis. Transition probability data is useful for determination of elemental abundances in stellar atmosphere, validating the atomic structure calculations and also for understanding of the radiative properties of La I needed for few applications like that in the lighting industry. In the present work, both LaH and ZrN molecules are produced at low temperature in pulsed supersonic free-jet apparatus. A rotating and translating metal rod is ablated with the third harmonic beam (354.7 nm, ~10–15 mJ/pulse) of a Nd: YAG laser focused to ~1 mm^2 spot. The laser produced metal plasma reacted with 2% ammonia seeded in He gas emerging from a pulse valve under a backing pressure of 275 kPa. The products of the reaction are expanded into vacuum, cooling the internal degrees of freedom of the molecules and are probed at right angle to the supersonic expansion axis about 50 mm downstream of the nozzle by a XeCl excimer pumped pulsed tunable dye laser. The resulting laser-induced fluorescence is imaged on an entrance slit of a monochromator equipped with a Peltier cooled photomultiplier tube. An output signal from the photomultiplier is amplified by a 1 GHz bandwidth amplifier, integrated by a gated integrator and stored on to a computer. Transition wavenumbers are calibrated by using a laser wavelength calibration facility of the dye laser utilizing neon optogalvanic spectral lines as well as by known atomic lines appearing in the spectra with an absolute precision of ~0.1 cm^{-1}. The molecular constants such as rotational constant, bond length, vibrational frequency, term energy are determined by using nonlinear least-squares fitting procedure of the observed transition wavenumbers to the energy level expression of the involved electronic states. The spectra are also fitted and simulated using Pgopher program [17].

The thesis is organized in six chapters. Chapter 1 presents a brief introduction and a theoretical background required to understand the electronic structure of a molecule with special emphasis on the diatomic molecule [18-22]. This chapter contains an introduction to Born-Oppenheimer approximation which separates electronic and nuclear motions. The information on rotational and vibrational structure of diatomic molecules is presented. Electronic structure of diatomic molecules including different angular momenta, molecular term symbols, Hund's coupling cases, spin-orbit components, parity and perturbation in the spectra of diatomic molecules is discussed in detail. This chapter, thus, provides both the introduction as well as theoretical background required to understand the work presented in the subsequent chapters.

Chapter 2 describes the experimental setup and the methodologies used in the present work. Production of a wide variety of metal-containing molecules of refractory nature and clusters became possible after the development of "Smalley source" in 1981[23]. The capability of the pulsed laser to vaporize elements of refractory nature in conjunction with supersonic expansion in free-jet allows formation of exotic species in the beam. Supersonic expansion is a well-known technique for cooling the internal degrees of freedom of molecules thereby simplifying the spectrum. This chapter describes the experimental setup which involves laser vaporization source, pulse valve, supersonic free-jet, tunable laser, fluorescence imaging and detection system, signal processing and data collection system. The classic technique of laser spectroscopy called Laser-Induced Fluorescence (LIF) is used in the present work. LIF spectra are recorded in two formats: fluorescence excitation spectrum and wavelength resolved fluorescence (WRF) or dispersed fluorescence (DF) spectrum. A fluorescence excitation spectrum is recorded by scanning the tunable dye laser frequency and recording the fluorescence intensity through the monochromator which is used as a broad band filter. The monochromator is set at the fixed wavelength corresponding to the strongest fluorescence terminating either to a ground or an excited state. However, wavelength resolved or dispersed fluorescence spectroscopy involves the scanning of monochromator set at high-spectral resolution while the laser frequency fixed to a selected transition to a particular ro-vibronic level. The fluorescence excitation spectra provide information about the lower and upper electronic states involved in the transition. However, the resolved fluorescence spectra provide information about the vibrational structure of ground state and the wealth of information on low-lying electronic states. These techniques are discussed in detail. This chapter thus provides the consolidated view of experimental techniques used in the present work.

Chapter 3 presents the study of ground and high-energy excited electronic states of LaH molecules. The rotationally-resolved excitation spectra provided information on symmetry and molecular constants of the ground and the excited electronic states. Prior to this work there was no direct confirmation of ground state symmetry of LaH molecule, which is essential for understanding the bonding in the molecule. Bacis and Bernard were the first to report the electronic spectra of LaH in the hallow cathode discharge source [24], a hot source where the excited electronic states are populated. They identified $^3\Phi_4$-$^3\Delta_3$, $^3\Phi_3$-$^3\Delta_2$, $^1\Delta$-$^1\Pi$, and $^1\Sigma$-$^1\Pi$ electronic transitions [25] and assigned $^3\Delta$ to be the ground state based on the erroneous *ab initio* calculations on isovalent ScH [4] and their observation of transitions originating from $^3\Delta$ state. Later, high level *ab initio* calculations by Das and Balasubramanian [26] which include relativistic and electron correlation effects predicted $^1\Sigma$ state as the ground state with a low-lying $^3\Delta$ as the first excited state. The observation of $A^1\Pi$-$X^1\Sigma^+$ band along with $d^3\Phi$-$a^3\Delta$, by Ram and Bernath [27] supported the predicted $^1\Sigma^+$ ground state symmetry of LaH [26]. However, their result is not a direct confirmation of ground state symmetry since they observed these bands in discharge source. In order to confirm the identity of the ground state and to get information on excited electronic states of LaH, we carried out LIF spectroscopic investigations in the energy range 13300-22500 cm^{-1}. The LaH molecules are produced in jet-cooled molecular beam by reaction of laser produced lanthanum metal plasma with 2% ammonia seeded in helium. A number of new excited electronic states are observed. The combination difference (CD) method confirmed that the lower state involved in these transition is the same as observed earlier by Ram and Bernath [27]. Since our spectra are obtained in a jet-cooled molecular beam where the major population exists in the ground state, we are entitled to conclude that the $X^1\Sigma^+$ state is indeed the ground state of the LaH molecule. In addition, the first intercombination transition in LaH is observed at 15623 cm^{-1} and assigned as $0^+(^3\Sigma^-)$–$X^1\Sigma^+$ and is discussed in detail in this chapter. The presence of P, Q, and R branch structure in bands with origin at 17398 and 17549 cm^{-1} indicated that the observed transitions are type $\Delta\Omega = \pm1$ and thus the upper states are assigned as $D1$ and $E1$. Short radiative lifetimes and strong intensities associated with these electronic states indicated that the transitions occur within the same multiplicity and thus the parent term assignment of the $D1$ and $E1$ states is $^1\Pi$. Three more electronic states with term energy at 20042, 21970 and 22100 cm^{-1} indicated the triplet character as evident from the dispersed fluorescence spectrum. However, the short radiative lifetimes of ~40 ns associated with these states contradict their triplet character. The state at 20042 cm^{-1} is assigned as $\Omega = 1$ and those at 21970 and 22100 cm^{-1} are assigned as $\Omega = 0^+$ in Hund's case(c), which is usual in heavy molecules. The molecular constants for all the newly observed excited electronic states are determined by fitting the observed set of transition wavenumbers of the excitation bands to the rotational energy level expression. The experimental results are compared with the available *ab initio* calculation. This chapter thus provides an experimental confirmation of ground state symmetry and molecular constants for several new excited electronic states of LaH molecule.

Chapter 4 presents the Dispersed Fluorescence (DF) study of LaH molecules. The principal motivation behind this study is to establish the missing energy linkage between singlet and triplet manifolds and also to determine the vibrational constants of the ground state of LaH molecule. In the absence of observation of inter-combination transition, the singlet and triplet stack of electronic states observed by earlier workers [25,27] were not placed energetically with respect to each other. This chapter provides the DF study of LaH by exciting single isolated rotational levels of excited electronic states reported in chapter 3. The DF spectrum with a moderate resolution (FWHM~50 cm^{-1}) gave information about the energies of the low-lying electronic states and their vibrations. The coarse spectra are then examined under relatively higher resolution (FWHM~15 cm^{-1}) to resolve the rotational structure, wherever possible, to confirm the identity of the lower states. The DF spectrum from $0^+(^3\Sigma^-)$ state revealed the presence of the first low-lying excited electronic state ($a^3\Delta_1$) of LaH molecule. This observation was important for establishing the missing energy link between the singlet ground state and $a^3\Delta$ state. The DF spectrum from $0^+(^3\Sigma^-)$ state also provided the vibrational constants of the ground state from the observed vibrational levels ν = 0-2. The DF spectra from the *D*1 and *E*1 electronic states revealed the presence of low-lying electronic states $a^3\Delta_2$, $b^3\Pi_0{}^{\pm}{}_{,1}$ and $B^1\Delta_2$, predicted by earlier *ab initio* studies [26]. However, $b^3\Pi_2$ low-energy electronic state was observed from the DF spectrum of $[20.0]\Omega = 1$ excited state. All the low-lying states below 11000 cm^{-1} predicted by *ab initio* calculations are observed and characterized in this chapter. Although *ab initio* studies predicted vibrations quite accurately, the term energies and spin-orbit separations are largely overestimated. In contrary to the *ab initio* prediction [26], the spin-orbit splitting of the $^3\Pi$ state is observed to be regular. These discrepancies between the present observations and earlier theoretical results may stimulate more refined *ab initio* studies leading to a better understanding of the electronic structure of LaH. The current information on the electronic structure of LaH is compared with those of isovalent ScH and YH molecules.

Chapter 5 deals with the study of excited electronic states of zirconium nitride (ZrN) molecules. Transition metal atoms have relatively high abundances in many stars [28] and several transition metal hydrides and oxides have been detected. Transition-metal nitrides (TMNs) are also possible to be present in the stellar atmosphere. However, TMNs have not been observed in the stellar atmosphere partly due to the lack of precise spectroscopic data required for their meaningful search in the complex stellar spectra. The motivation for this work is to extend the $B^2\Sigma^+$-$X^2\Sigma^+$ and $A^2\Pi$-$X^2\Sigma^+$ systems to the higher vibrational levels to improve the molecular constants at equilibrium. Bates and Dunn [29] first recorded the spectra of ZrN molecule. They observed (0,0) band of $B^2\Sigma^+$-$X^2\Sigma^+$ system and (0,0), (1,1), and (2,2) bands of $A^2\Pi$-$X^2\Sigma^+$ system using conventional emission spectroscopy. Bates and Gruen [30] confirmed the $X^2\Sigma^+$ as the ground state of ZrN. Later, Cheung and co-workers revisited the $B^2\Sigma^+$-$X^2\Sigma^+$ and $A^2\Pi$-$X^2\Sigma^+$ systems of ZrN [31-37] using laser-induced fluorescence (LIF) spectroscopy. They studied the previously observed (0,0), (1,1), and (2,2) bands [31,33 ,35] of $A^2\Pi$-$X^2\Sigma^+$ system for the various isotopomer of ZrN. Cheung and co-workers did not observe the (1,0) band in $B^2\Sigma^+$-$X^2\Sigma^+$ system, and attributed their lack of success to a very unfavorable Franck-Condon factor. However, we observed (1,0), (1,1), (2,0), (2,1), (2,3) bands with considerable intensity and a weak (3,4) band. We have also observed (3,3) band of $A^2\Pi$-$X^2\Sigma^+$ system along with the previously reported (0,0), (1,1), and (2,2) bands. Perturbations are observed in all the bands of the *B*-*X* system. The perturbed lines are removed from the fit while determining the molecular constants. The rotational perturbations are identified at several places in the (0,0), (1,1) and (2,2) sub-bands of $A^2\Pi_{3/2}$-$X^2\Sigma^+$ system in the previous works [31,33 ,35]. However, (3,3) band of the $A^2\Pi_{3/2}$-$X^2\Sigma^+$ system is found to be unperturbed in the present work and the rotational constants and the term energies of both states are determined. The *e*-parity levels of (3,3) band in the $A^2\Pi_{1/2}$-$X^2\Sigma^+$ system are found to be free from perturbation and the rotational constants are determined by fitting only the *e* levels. However, rotational perturbations are observed in the *f*-parity levels of (3,3) band in the $A^2\Pi_{1/2}$-$X^2\Sigma^+$ system. The DF spectra from various newly observed bands of the *B*-*X* system provided the vibrational energies of the ground state up to $\nu = 5$.

Chapter 6 describes the radiative lifetime measurements of neutral Lanthanum (La I) atom using time-resolved laser-induced fluorescence spectroscopy in supersonic free-jet. Measurement of laboratory radiative data of atoms like, transition probabilities, radiative lifetimes and branching fractions is of great interest. This is useful in analyzing the available stellar spectra for the quantitative determination of their abundance in the Sun and peculiar stars [38]. In addition, radiative data on rare earth elements is of commercial importance due to their usage as additives in metal halide high-intensity discharge (MH-HID) lamps which provide a pleasing white light with higher luminous efficacy as compared to conventional incandescent light sources [39]. There is a need for measurement of radiative lifetime data for many levels, particularly below 18000 cm^{-1} in La I. In the present work, the technique of laser vaporization in conjunction with supersonic expansion is used for generating a supersonic free-jet of lanthanum atoms. In supersonic free-jet, the excitation of atoms takes place in collision-free environment at a low atom number density and thus measured radiative lifetimes are free from collisional and radiation trapping effects. This study provided-radiative lifetime data, accurate within ±10%, for 63 odd-parity levels belonging to the odd $5d6s6p$, $4f6s^2$, $6s^26p$, $5d^26p$, $4f5d6s$ electronic configurations in La I in the energy range 13260 – 30965 cm^{-1}. Care was taken to minimize the influence on the lifetime measurements due to various effects like flight-out-of view, radiation trapping, saturation, and collisional depopulation. The measured lifetime values fall in the range 9.5 to 313 ns. For levels that have lifetimes longer than 80 ns, lifetimes are evaluated by fitting the observed fluorescence decay curve to a single exponential decay function. However, for the short-lived excited states, lifetimes are evaluated by fitting the observed fluorescence decay curve with a convolution between a Gaussian function which represented the excitation laser pulse and an exponential function with adjustable parameters. Lifetimes for the 45 levels among the obtained results are reported for the first time.

References:

[1] J.F. Harrison, Chem. Rev. **100**, 679 (2000).

[2] K. Balasubramanian, J. Phys. Chem. **93**, 6585 (1989).

[3] A. Lagerqvist, R. Scullman, Arkiv Fys. **32**,479 (1966).

[4] P.R. Scott, W.G. Richards, J. Phys. B **7,** 1679 (1974).

[5] A. Bernard and R. Bacis, Can. J. Phys. **55**, 1322 (1977).

[6] R. Bacis, A. Bernard, and A. Zgainsky, C. R. Hebd. Seances Acad. Sci.,Ser. A, B **280**, 77 (1975).

[7] B. Simard, P. A. Hackett, and W. J. Balfour, Chem. Phys. Lett. **230**, 103 (1994).

[8] N. Koga and K. Morokuma, Chem. Rev. **91**, 823 (1991).

[9] A. Veillard, Chem. Rev. **91**, 743 (1991).

[10] W. A. Brown, R. Kose and D. A. King, J. Mol. Catal. A **141**, 21 (1999).

[11] W. Weltner, Jr., Science **155**, 155 (1967).

[12] P.Vajda and J.N. Daou, Phys. Rev. B **49**, 3275 (1994).

[13] W. Bauhofer, W. Joss, R.K. Kremer, H. J. Mattausch, and A. Simon, J.Magn. Mater. **104**, 1243 (1992).

[14] C. Rao and J. Gopalakrishanan, New Directions in solid state Chemistry, CUP, London, 3rd edition ,1986.

[15] G.J. Leigh, Science **279**, 506 (1998).

[16] Y. Nishibayashi, S. Iwai, M. Hidai, Science **279**, 540 (1998).

[17] Western CM. PGOPHER, a program for simulating rotational structure, University of Bristol. 2010; http://pgopher.chm.bris.ac.uk.

[18] G. Herzberg, Molecular Spectra and Molecular Structure, I. Spectra of Diatomic Molecules, 2nd Edition, D. Van Nostrand, New York, 1950.

[19] H.Lefebvre-Brion, R.W.Field, The spectra and Dynamics of Diatomic Molecules, revised and enlarged edition, Elsevier Academic Press, New York, 2004.

[20] J.Brown, A.Carrington, , Rotational Spectroscopy of Diatomic Molecules ,Cambridge University Press, United Kingdom, 2003.

[21] I.Kovacs, Rotational Spectroscopy in the spectra of Diatomic Molecules Elsevier Publishing, New York, 1969.

[22] P. F. Bernath, Spectra of Atoms and Molecules, Oxford University Press, New York, 2nd edition, 2005.

[23] T. G. Dietz, M. A. Duncan, D. E. Powers, and R. E. Smalley, J. Chem. Phys. **74,** 6511 (1981).

[24] R. Bacis , A. Bernard , A. Zgainski, C.R. Acad. Sci. B **280**, 77 (1975).

[25] A.Bernard ,R. Bacis . Can .J. Phys. **54**, 1509 (1976).

[26] K.K. Das, K. Balasubramanian, Chem. Phys. Lett. **172**, 372 (1990).

[27] R.S. Ram, P.F. Bernath, J. Chem. Phys. **104,** 6444 (1996).

[28] C. Jaschek, M. Jaschek, The Behavior of Chemical Elements in Stars, Cambridge University Press, Cambridge, 1995.

[29] J.K. Bates,T.M. Dunn, Can. J. Phys. **54**,1216 (1976).

[30] J.K. Bates, D.M. Gruen, High. Temp. Sci. **18**, 27 (1978).

[31] H. Li, C.M.T. Chan, A.S.C. Cheung, J. Mol .Spectrosc. **176**, 219 (1996).

[32] C.M.T. Chan, H. Li, N.S.K. Sze, A.S.C. Cheung, J. Mol. Spectrosc. **180**,145 (1996).

[33] C.M.T. Chan, H. Li, A.S.C. Cheung, Chem .Phys .Lett. **269**, 49 (1997).

[34] H. Jiang, C. Ma, A.S.C. Cheung, Chem. Phys. Lett. **295**, 535 (1998).

[35] A.S.C. Cheung, H. Li. H. Jiang, Chen, J. Mol. Spectrosc. **210**, 84 (2001).

[36] H. Chen,Y. Li, D.K.W. Mok, A.S.C. Cheung, J. Mol. Spectrosc. **218**, 213 (2003).

[37] H. Jiang, Q. Shi, A.S.C. Cheung, J .Mol. Spectrosc. **200**, 283 (2000).

[38] E. Biémont, P.Quinet, Phys. Scr. T **105**, 38 (2003).

[39] E. A. Den Hartog, K. A. Bilty and J.E. Lawler, J.Phys. B: At. Mol. Opt. Phys. **44**, 055001 (2011).

LIST OF FIGURES

LIST OF TABLES

Chapter 1

Introduction

1.1. General Introduction

Diatomic molecules are fundamentally important because they provide the simplest model to probe the nature of a chemical bond. Experimentally, the probe is realized through the interaction of the molecule with light or through molecular spectroscopy. Molecular spectroscopy is a powerful branch of Science which can be used to study the identity and nature of not only the stable molecules but also the reactive transient species like free radicals and ions. The scientific discipline of diatomic molecular spectroscopy is rich and diverse. There are several textbooks [1-5] devoted to the subject. From a basic scientific perspective, analysis of spectra of diatomic molecules reveal information about the electronic, vibrational, rotational, fine and hyperfine structure. The study of electronic motions of a molecule can reveal a great deal of information on chemical valence. Vibrational spectra can assist in accurate calculation of inter-atomic forces as well as the dissociation energy of the molecule. From the rotational spectra, researchers can obtain knowledge about the geometrical arrangement of the nuclei in the molecule; in particular, extremely accurate values of the internuclear distances.

Transition-metal (TM) containing diatomic molecules play an important role in many fields, such as catalysis [6], organometallics [7], surface science [8], and astrophysics [9]. The 3*d* transition metals have a special place in astrophysics because of the great stability of the nuclei [10]. Oxygen also has high cosmic abundance. High dissociation energy of 3*d* metal diatomic oxides makes them stable in low-temperature stars and many of them have been detected in the spectra of cooler stars (M-type). Low-temperature astrophysics is high-temperature terrestrial chemistry and it is found that the thermodynamically stable high temperature forms of the transition metal oxides are diatomic vapors. The transition-metal containing diatomics are highly refractory materials and this makes it difficult to get them into the gas phase under non-equilibrium low temperature conditions. High temperature often complicates the spectra because of the complex electronic structure associated with them. This is the reason why the progress in the spectra of transition-metal containing diatomics was has held back in the past. Transition-metals (TMs) are proposed to play a role in astrophysical environments in both gas and solid state astrochemistry by co-determining the homogeneous/heterogeneous chemistry represented by the gas-gas and gas-dust grain interactions [11]. Recently, ExoMol project [12] provided the comprehensive spectral line lists of molecular transitions which are likely to be important in the atmospheres of extra-solar planets, cool stars and brown dwarfs. These molecular emission line data provide information on abundance and various physical processes occurring in many types of astronomical sources. Ionization potentials and dissociation energies are important fundamental quantities in the interpretation of molecular structure and spectra and in studies of the interactions between molecules and atoms [13]. These quantities are required to interpret dissociation equilibria and ionization processes in stellar and planetary atmospheres. Since the TMs are having high cosmic abundance, their atoms and those containing molecules are observed in different types of cool stars. For example, the band systems of TiO and VO completely dominate the spectra of cooler (M-type) star [14] and, NiH [15] and CrH [16-19] molecules were observed in the spectra of sunspots, while spectra of FeH [20,21] and TiH [22,23] were identified in M-type stars. There are currently over 120 different types of molecules which have been observed in interstellar space.

Lanthanum and zirconium are also identified in their oxide forms in S-type stars [9] and, their hydrides and nitrides are also possible to be present in the stellar atmosphere. However, so far these are not found in the stellar atmosphere partly due to the lack of precise spectroscopic data required for their meaningful search in the complex stellar spectra. For this purpose laboratory experimental data on astrophysical important atoms and molecules are needed. Transition-metal mono hydrides are also important because they represent the simplest metal-hydrogen bond, and their studies provide a starting point for the research on gas-surface interactions and catalytic processes. For example, the oxidative addition of the N-H bond of ammonia or amines to a transition metal center is an important reaction for the development of catalytic processes involving carbonylation or alkylation of ammonia and amines [24,25]. Transition metals play a vital role in nitrogen fixation in biological systems [26,27], industrial processes such as the production of ammonia [28], and pollution control [29]. The Haber–Bosch process for ammonia synthesis is the most important invention of the 20th century. It was the first heterogeneous catalytic process employed in the chemical industry and is still in use today. This process requires a solid catalyst and even with the best so far known catalysts it is only feasible at harsh conditions, high temperatures (650–750 K) and pressures (50–200 bar). Recently, Vojvodic *et al.*[30] examined the catalyst requirements for a new low-pressure, low-temperature for Haber–Bosch synthesis process and they showed that at a temperature of 373 K, a pressure of 1 bar this process is achievable with a rate in excess of 1 turnover per active site per second with an ideal catalyst. Therefore, a basic understanding of the chemical bonds between nitrogen and various transition metals is important. Transition-metal oxides and carbides because of high melting points are also vital to the rocket and space industries [9].

Over the past decades, significant progress has been made towards understanding the nature of the chemical bond in transition-metal containing diatomic molecules [10,31,32]. A detailed understanding of the electronic structure and bonding at the molecular level can be gained by analyzing the spectroscopic data obtained from various gas phase and matrix isolation techniques. The experimental results provide guidance for theoretical chemists to test the validity of their approximations and accordingly develop robust theoretical methods capable of accurately describing the electronic structure and geometry of larger systems. The experimental and theoretical challenges in the study of transition-metal containing molecules arise from the presence of open *d* sub-shells in their ground atomic states. Nevertheless, it is this feature that also gives rise to the unique bonding possibilities that make the transition metals such superb catalysts. It is known that the *d*-electrons associated with transition metal has large electron correlation effects and the difficulty lies in getting these effects right. Small changes in the model can lead to very different predictions for the energy order and properties of the low-lying electronic states. The relativistic and spin-orbit effects are also very important in these molecules and need to consider in *ab initio* calculations. Due to the fast advancement in the computational capability in recent times, new and improved methods for electronic structure calculations have been developed in past few years. These *ab initio* calculations which account for configuration interaction, electron correlation, exchange and relativistic effects in their treatment are very important for the molecules containing transition metal atoms [33]. On experimental front, the real problem with the spectra of transition metal containing molecules comes from the many unpaired electrons associated with transition metal atom. The open *d*-shells of these metals give rise to a large density of low- as well as high-lying excited electronic states with high spin multiplicity and orbital angular momenta. Energy proximity of these states results in wide spread perturbations in the spectra which makes it hard to analyze. In addition, transition metal nuclei with odd atomic mass numbers usually have large nuclear spin and magnetic moments and thus large spread hyperfine structure associated with these molecules complicates the spectra further. The transition metal molecules, being of refractory nature, require high temperature to bring them in gas phase for performing spectroscopic investigations. Under these high temperature conditions the molecules are thermally excited into many low-lying electronic, rotational and vibrational levels which the spectra complex to analyze and often leads to erroneous conclusions. This reason has plagued the progress in the spectra of these molecules. However, the study of transition metal containing diatomic molecules has been benefitted from the numerous developments made in the recent past. The development of experimental technique of laser ablation followed by supersonic expansion [34,35], creating a molecular beam of refractory material at low temperature wherein most of the population remained in few rotational levels of the ground state, simplified the spectra dramatically. This simplified spectra led to an unambiguous assignment of symmetry of the ground and excited electronic states [36] which is very important for understanding the nature of the transition metal-main group element bond. In our laboratory, we have undertaken an experimental investigation to understand the nature of bond between transition metal atom with main group elements like hydrogen, carbon, nitrogen, and oxygen [37-41] using laser-induced fluorescence (LIF) spectroscopy in pulsed supersonic free-jet. The present doctoral work is an outcome of above mentioned project.

This thesis presents the experimental investigation of electronic structure of two diatomic molecules lanthanum hydride (LaH) and zirconium nitride (ZrN), produced at low temperature in pulsed supersonic free-jet, using laser-induced fluorescence (LIF) spectroscopy. In addition, radiative lifetime measurements of neutral Lanthanum (La I) atom using time-resolved laser-induced fluorescence spectroscopy in supersonic free-jet also included in this thesis. Transition probability data is useful for determination of elemental abundances in stellar atmosphere, validating the atomic structure calculations and also for understanding of the radiative properties of La I needed for few applications like that in the lighting industry. The rotationally-resolved excitation spectra provided information on symmetry and molecular constants of the ground and the excited electronic states. In case of LaH molecule the ground state $^1\Sigma^+$ symmetry is confirmed, which is essential for understanding the bonding in the molecule. Observation and analysis of several new low- and high-energy excited electronic states is also reported. Dispersed fluorescence (DF) spectroscopy established the energy linkage between singlet and triplet manifolds in LaH. In addition, vibrational frequencies for ground and low-lying electronic states are also determined. While in case of ZrN molecule, we extended the observation and analysis of earlier known excited electronic states to higher vibrations to improve the molecular constants at equilibrium using LIF spectroscopy. The next section present the theoretical background in brief, required for understanding the analysis of spectroscopic data presented in the subsequent chapters.

1.2 Theoretical background for Diatomic molecules

1.2.1 Born-Oppenheimer approximation

The quantized energy levels of a molecule can be computed in principle by solving the time independent Schrödinger equation [1,5,42],

$$\hat{H}\Psi = \left(\hat{T}_N + \hat{T}_e + \hat{V}_{NN} + \hat{V}_{eN} + \hat{V}_{ee}\right)\Psi = E\Psi \qquad (1.1)$$

Here E is the total energy. It is the sum of nuclear kinetic energy ($\hat{T}_N$), electronic kinetic energy ($\hat{T}_e$), nuclear-nuclear repulsion energy ($\hat{V}_{NN}$), electron-nuclear attraction energy ($\hat{V}_{eN}$) and electron-electron repulsion energy ($\hat{V}_{ee}$). The solution of Eq. 1.1 can be simplified by the separation of the electronic and nuclear motions and is known as the Born-Oppenheimer approximation [43]. The Coulombic forces acting on nuclei and electrons are the same order of magnitude, but the masses of electrons are much smaller, and therefore they move faster. The electronic motion can therefore be separated from the much slower nuclear (vibration-rotation) motion. In the "clamped nuclei" approximation, the positions of the nuclei are held fixed at various molecular geometries ($\mathbf{r}_\alpha$), and the electronic Schrödinger equation is solved to obtain the electronic structure:

$$\hat{H}_{el}\Psi_{\mathrm{el}} = (\hat{T}_e + \hat{V}_{eN} + \hat{V}_{ee})\Psi = E_{el}\Psi_{\mathrm{el}} \tag{1.2}$$

Since the nuclear motion is frozen at each particular geometry, the nuclear-nuclear repulsion term in Eq. (1.1) is just a number, and can be added to E_{el} to give the total potential energy for a particular electronic state:

$$U(r_\alpha) = E_{el}(r_\alpha) + V_{NN}(r_\alpha) \tag{1.3}$$

This potential energy depends parametrically on the positions of the nuclei ($\boldsymbol{r}_\alpha$), and there is no general analytic function for it. The vibration and rotation parts of the nuclear motion can be further separated in a similar way. So, the total wave function is a simple product of electronic and nuclear wave functions [1,5],

$$\Psi(r_i; r_\alpha) \approx \Psi_{el}(r_i; r_\alpha)\chi_N(r_\alpha) \tag{1.4}$$

and the following two equations should be solved consecutively to obtain the energy levels:

$$(\hat{T}_e + \hat{V}_{ee} + \hat{V}_{eN} + \hat{V}_{NN})\Psi_{el}(r_i; r_\alpha) = U(r_\alpha)\Psi_{el}(r_i; r_\alpha)\ , \tag{1.5}$$

$$\left(\hat{T}_N + U(r_\alpha)\right)\chi_N(r_\alpha) = E_N\chi_N(r_\alpha) \tag{1.6}$$

Eq. (1.5) is solved first for all possible nuclear positions (r_α) to obtain $U(\boldsymbol{r}_\alpha)$,which is used in Eq. (1.6) as the potential energy function governing the motion of the nuclei. The variables $\mathbf{r}_i$ and $\mathbf{r}_\alpha$ in the above equations represent the positions of electrons and nuclei, respectively.

1.2.2 Rotational structure of diatomic molecules

The rotation of a diatomic molecule can be approximated by that of a rigid rotator, for which the energy levels are given by,

$$E(J) = hcF(J) = hcBJ(J+1) \ , \qquad J = 0, 1, 2\ldots \tag{1.7}$$

where h and c are Planck constant and speed of light respectively, and *F (J)* and rotational constant *B* are in cm^{-1} and *J* is the rotational angular momentum quantum number. The equilibrium rotational constant B_e related to moment of inertia (I_e) and to the equilibrium internuclear distance (r_e) by [1, 5],

$$\mathrm{B_e} = \frac{h}{8\pi^2 c\mathrm{I}_e} = \frac{h}{8\pi^2 c\mu r_e^2} \tag{1.8}$$

in which μ is the reduced mass and is expressed as ,

$$\mu = \frac{m_A m_B}{m_A + m_B} \tag{1.9}$$

Here m_A and m_B are masses of the atoms A and B of a diatomic molecule. The most convenient expression for rotational constant *B* is [5],

$$B = \frac{16.85762908}{I/(u\text{Å}^2)} cm^{-1} \tag{1.10}$$

The molecule, of course, is not completely rigid, and as it rotates the centrifugal forces cause the internuclear distance to elongate slightly. The rotational-level energy expression thus has to have the terms that account for the effect of centrifugal forces, and it is customary to express the rotational energy as a power series in $J(J+1)$,

$$F(J) = BJ(J+1) - D[J(J+1)]^2 + H[J(J+1)]^3 + L[J(J+1)]^4 + \cdots \tag{1.11}$$

where *D*, *H* and *L* are centrifugal distortion constants.

1.2.3 Vibrational structure of diatomic molecules

The most commonly used function for representing the parametric dependence of potential energy, U on internuclear distance, r was first introduced by Dunham [44], and is a Taylor series expansion about the equilibrium internuclear distance (r_e). At the bottom of the potential energy curve, both $U(r_e)$ and the first derivative of $U(r)$ are equal to zero. Therefore, $U(r)$ is expressed by the following equation,

$$U(r) = \frac{1}{2} k_2 (r - r_e)^2 + \frac{1}{6} k_3 (r - r_e)^3 + \frac{1}{24} k_4 (r - r_e)^4 + \ldots\ldots \quad (1.12)$$

in which k_n is the nth derivative of the potential energy function evaluated at r_e. The leading term on the right of Eq. (1.12) is the well-known potential energy function of a harmonic oscillator. The harmonic oscillator solution is obtained for the non rotating molecule,

$$E(v) = hcG(v) = hc\omega_e \left(v + \frac{1}{2}\right), \quad v = 0, 1, 2 \ldots \quad (1.13)$$

$G(v)$ and ω_e have units of cm^{-1}, and ν is the vibrational quantum number. However, since the potential energy curve of a diatomic molecule is always anharmonic, it is customary to express the vibrational energy as a power series in $(\nu+1/2)$,

$$G(v) = \omega_e \left(v + \frac{1}{2}\right) - \omega_e x_e \left(v + \frac{1}{2}\right)^2 + \omega_e y_e \left(v + \frac{1}{2}\right)^3 + \cdots \quad (1.14)$$

in which ω_e is harmonic frequency and $\omega_e x_e$ and $\omega_e y_e$ are anharmonic frequencies. The value of the rotational constant B depends on the vibrational state of the molecule, since $B \propto \frac{1}{r^2}$, the vibrational dependence of B can be modeled by the following expression [1,5],

$$B_v = B_e - \alpha_e \left(v + \frac{1}{2}\right) + \gamma_e \left(v + \frac{1}{2}\right)^2 + \cdots \quad (1.15)$$

where B_e is the equilibrium rotational constant and α_e and γ_e are rotation-vibration interaction coefficients.

Another expression for potential energy of diatomic molecule given by Morse [45],

$$U(r) = D[1 - \exp\left(-\beta(r - r_e)\right)]^2 \tag{1.16}$$

here, D is the dissociation energy relative to the bottom of the potential, and β is the Morse potential parameter. If one uses the Morse function for $U(r)$, it's analytical solution for the non rotating molecule,

$$G(v) = \omega_e \left(v + \frac{1}{2}\right) - \omega_e x_e \left(v + \frac{1}{2}\right)^2 \tag{1.17}$$

The first anharmonicity constant ($\omega_e x_e$) appears naturally in the energy level expression obtained from the Morse potential [45], but the higher order constants in Eq. (1.12) are all identically zero for this case. A popular expression for the energy levels of the vibrating rotor was introduced by Dunham [46] by using the first-order semi-classical quantization condition from WKB (Wentzel, Kramers, Brillouin) theory,

$$E_{v,J}(cm^{-1}) = \sum_{m=0} \sum_{l=0} Y_{l,m} \left(v + \frac{1}{2}\right)^l [J(J+1)]^m \tag{1.18}$$

The coefficients Y_{lm} can be related to the conventional spectroscopic constants [1, 5]

$$Y_{1,0} = \omega_e \qquad Y_{0,1} = B_e \qquad Y_{0,2} = D_e$$

$$Y_{2,0} = \omega_e x_e \qquad Y_{1,1} = \alpha_e$$

The spectroscopic constants associated with vibration and rotation depends on the reduced mass; therefore, their values are different for different isotopologues of the same molecule. The isotopic dependence of the spectroscopic constants can be conveniently generalized for the Dunham Y_{lm} constants as,

$$Y_{l,m} \propto \mu^{-(\frac{1+2m}{2})} \tag{1.19}$$

Therefore, within the Born-Oppenheimer approximation, the parameters associated with different isotopologues are related as,

$$Y_{l,m}^{(\alpha)} = Y_{l,m}^{(\beta)} (\frac{\mu_\beta}{\mu_\alpha})^{m+1/2} \tag{1.20}$$

Where μ_β is the reduced mass of the reference isotopologue and μ_α is the reduced mass of isotopologue-α. Since the Born-Oppenheimer and the first-order WKB approximations can break down, especially for light diatomic molecules, it is often necessary to add small correction terms to Eq. (1.19). These terms are generally referred to as the "Born-Oppenheimer breakdown correction parameters".

1.2.4 Electronic structure of diatomic molecules

1.2.4.1 Angular momentum

To understand the electronic spectrum of diatomic molecules, it is important to consider their angular momenta and the interaction between these momenta. For diatomic molecules, with exclusion of nuclear spin, the total angular momentum **J** is the vector sum of electron orbital **L**, electron spin **S**, nuclear rotation **R** angular momenta as shown

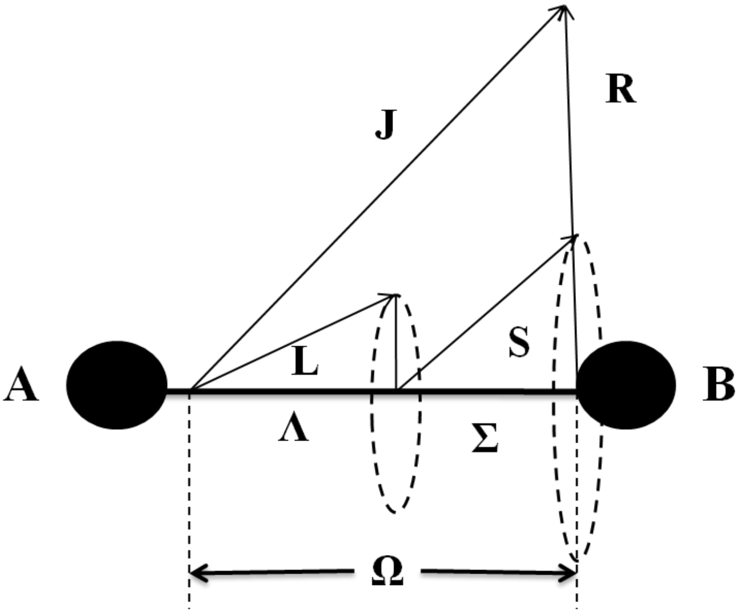

Figure 1.1. Angular momenta in diatomic molecules.

Table 1.1. Angular momenta in diatomic molecules.

Angular momentum	**Projection on molecular axis (units of ħ)**
J	$\Omega=\Lambda+\Sigma$
L	Λ
S	Σ
R	-
N = R+L	Λ

Note: Here the Σ is completely different from the Σ state arises from $\Lambda=0$.

in Fig.1.1. The total angular momentum **J** and various other angular momenta and their projections on molecular axis are given in Table 1.1.

1.2.4.2 Molecular term symbols

The molecular term symbol is a shorthand expression for the approximately good quantum numbers. A review of term symbols for diatomic molecules can be found in Ref [1, 5]. The states of a molecule can be specified by molecular term symbols which label these states and specify the total spin and orbital angular momenta of the molecule, along with various other symmetries. The general form for the electronic term symbol of linear molecules is written as:

$$^{2S+1}|\Lambda|^{(+/-)}_{(\Omega \quad or \quad g/u)} \tag{1.21}$$

Where

(1) $2\boldsymbol{S}+1$ is the multiplicity, $\boldsymbol{S}$ is the total spin angular momentum quantum number, formed from the individual electrons spin quantum numbers, $s_i=1/2$. For example, for one unpaired electron, $\boldsymbol{S}=s_1=1/2$ (a doublet state with $2\boldsymbol{S}+1=2\times1/2+1=2$); for two unpaired

electrons the possible values are $\boldsymbol{S}=s_1+s_2=1$ or $\boldsymbol{S}=s_1-s_2=0$, giving a triplet ($2\boldsymbol{S}+1=2\times1+1=3$) or a singlet ($2\boldsymbol{S}+1=2\times0+1=1$) state, etc.;

(2) Λ is the quantum number for the projection of total orbital angular momentum, **L** of the electrons along the internuclear axis. Unlike in atoms, the cylindrical symmetry created by the strong electric field of the nuclei in a linear molecule destroys the relationship $[\boldsymbol{H}, \boldsymbol{L}^2] = 0$, and so $\boldsymbol{L}$, the total electronic orbital angular momentum, ceases to be a good quantum number. Instead, we can use the quantum number Λ, corresponding to the component of $\boldsymbol{L}$ along the internuclear (z-)axis:

$$\Lambda = \sum_i \lambda_i \tag{1.22}$$

Where λ_i is equal to 0 for σ electrons and ±1 for a π electron. $|\Lambda| = 0, 1, 2, 3\ldots$is written Σ,Π,Δ, Φ….

The Λ is defined as,

$$\hat{L}_z \Psi^{el} = \Lambda \Psi^{el} \tag{1.23}$$

(3) Ω is the total electronic angular momentum ($\Omega = \Sigma+\Lambda$), along the internuclear axis, which is defined as,

$$\hat{J}_Z \Psi^{el} = \Omega \Psi^{el} \tag{1.24}$$

Here, Σ is the projection of the electric spin angular momentum, S along the internuclear axis. Because $[S^2, \hat{S}_Z] = 0$, the Σ is defined as,

$$\hat{S}_z \Psi^{el} = \Sigma \Psi^{el} \tag{1.25}$$

(4) The *g/u* subscripts is the parity which applies only to molecules with a center of symmetry and labels the symmetry of the electronic wavefunction with respect to inversion symmetry through this center, which is defined as ,

$$\hat{\imath} \Psi^{el} = \pm \Psi^{el} \tag{1.26}$$

Here, *g* and *u* represent +1 and -1, respectively.

(5) The +/- superscript reflects symmetry along an arbitrary plane containing the internuclear axis , which applies only to Σ states, and labels the symmetry of the electronic wavefunction with respect to reflection in a plane containing the nuclei, which can be expressed as,

$$\hat{\sigma}\Psi^{el} = \pm\Psi^{el} \tag{1.27}$$

The operators, $\hat{L}_z$, $\hat{S}^2$, $\hat{S}_z$, and $\hat{J}_z$ are assumed eigen operators of the wavefunction with good quantum numbers, Λ, **S**, Σ, and Ω. This is true only when spin-orbit interactions are ignored. The selection rules for possible electronic transition among the energy levels in diatomic molecules are,

1. ΔΛ = 0,±1 The transitions like Π-Π, Δ-Φ, Π-Σ are allowed.
2. ΔS = 0 Transitions within same multiplicity are only allowed.
3. ΔΣ = 0
4. ΔΩ = 0,±1
5. $+ \leftrightarrow +, - \leftrightarrow -$ and $+ \not\leftrightarrow -$ Transitions only allowed within same symmetry.

1.2.4.3 Hund's coupling cases

The spectra of diatomic molecules recorded for a specific band system are modeled by an effective Hamiltonian operator with a series of variable spectroscopic parameters. These parameters are obtained to characterize the electronic structure of the molecules. The electronic spectra of molecules that do not have closed electron shells are usually quite complex because of the interaction of different angular momenta. In the absence of nuclear spin there are three fine structure interactions associated with the magnetic moments due to electrons, which are summarized in Table 1.2.

The effective Hamiltonian for a diatomic molecule can be therefore written as,

$$\hat{H}_{eff} = \hat{H}_{vib} + \hat{H}_{rot} + \hat{H}_{SO} + \hat{H}_{SR} + \hat{H}_{SS} + \hat{H}_{LD} \tag{1.28}$$

Where, $\widehat{H}_{SO} = A\boldsymbol{L}.\boldsymbol{S},$ (1.28(a))

$$\widehat{H}_{SR} = \gamma\boldsymbol{N}.\boldsymbol{S}, \tag{1.28(b)}$$

$$\widehat{H}_{SS} = \frac{2}{3}\lambda(3\boldsymbol{S}_z^2 - \boldsymbol{S}^2), \tag{1.28(c)}$$

The λ-doubling of high spin multiplicity electronic states with Λ≠0 has been discussed by Brown *et al.* [47–50] .The effective Hamiltonian operator of a Π state may be written as:

$$\widehat{H}_{LD} = \frac{1}{2}(o + p + q)(S_+^2 + S_-^2) - \frac{1}{2}(p + 2q)(J_+S_+ + J_-S_-) + \frac{1}{2}q(J_+^2 + J_-^2) \tag{1.28(d)}$$

Hund [51] considered five coupling situations that could arise for different strengths of the couplings between the rotation and electron angular momenta, which subsequently known as Hund's coupling cases (a), (b), (c), (d) and (e) [1]. In the present thesis, first three coupling schemes are used for characterizing the electronic states which will be discussed in the following sections.

Table 1.2. Coupling of angular momenta.

Interaction term	Designation	Description
R.S	Spin-Rotation (SR)	Total electron spin interacting with the magnetic fields created by nuclear motion
L.S	Spin-Orbit (SO)	Electron spin interacting with the magnetic fields created by electron motion
S.S	Spin-Spin (SS)	Interaction between magnetic moments of different unpaired electrons

1.2.4.3.a Hund's case (a)

In Hund's case (a), it is assumed that the interaction of the nuclear rotation with the electronic motion (spin as well as orbital) is very weak, whereas the electronic motion itself is coupled very strongly to the line joining the nuclei [1] i.e. $A >> BJ$, where A is spin orbit constant. The vector diagram of Hund's case (a) is shown in Fig.1.2. The electron orbital angular momentum **L** and electron spin angular momentum **S** are coupled strongly to internuclear axis and formed their projections Λ and Σ respectively. The total electronic angular momentum about the internuclear axis, denoted by Ω is obtained by adding Λ+ Σ, i.e.

$$\Omega = \Lambda + \Sigma \tag{1.29}$$

The total electronic angular momentum Ω about the internuclear axis is again coupled to the nuclear rotational angular momentum **R**. The total angular momentum **J** excluding nuclear spin is then produced:

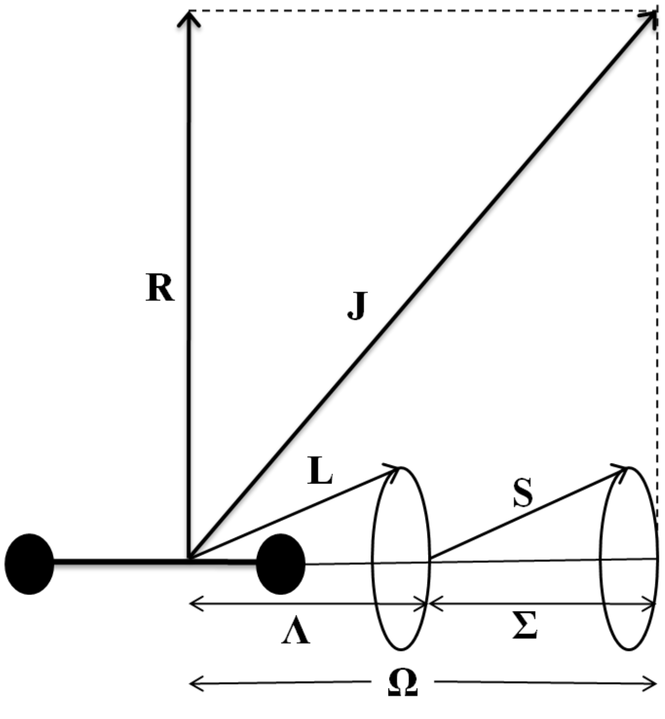

Figure 1.2. The vector diagram for Hund's case (a).

$$\mathbf{J} = \mathbf{\Omega} + \mathbf{R} \tag{1.30}$$

For a given Ω we have,

$$\mathbf{J} = \Omega, \Omega+1, \Omega+2\ldots\ldots \tag{1.31}$$

The "good" quantum number in Hund's case (a) are Λ, **S**, Σ, **J** and Ω. In a pure case (a) there are 2**S** +1 spin components, each with their own Ω value, and each of these spin components has a pattern of rotational energy levels given by $B_{\Omega\, eff}\, J(J + 1)$, with the lowest level having **J** = Ω. Each **J** is doubly degenerate (for Ω > 0), corresponding to *e* and *f* parities. Although Λ = 0 for Σ states, second order spin-orbit coupling can split a $^{2S+1}\Sigma$ state into **S**+1 spin components [52] and is referred as Hund's coupling case (a') [53].

1.2.4.3.b Hund's case (b)

In Hund's case (b), the spin-orbit coupling is small ($A << BJ$); therefore **S** is only weakly coupled to the internuclear axis. **L** has the same significance as for case (a). The vector diagram for Hund's case (b) shown in Fig.1.3. The projection of **L**, i.e. Λ (when Λ ≠ 0) is first coupled with **R** to form the total rotational angular momentum of the molecule, denoted by **N**,

$$\mathbf{N} = \mathbf{R} + \mathbf{L} \tag{1.32}$$

This **N** is then coupled with **S** to form the total angular momentum excluding nuclear spin **I**,

$$\mathbf{J} = \mathbf{N} + \mathbf{S} \tag{1.33}$$

The quantum numbers Ω and Σ are not defined in this scheme. The "good" quantum numbers in Hund's case (b) are Λ, **N**, **S** and **J**. The energy of the rotational levels is given

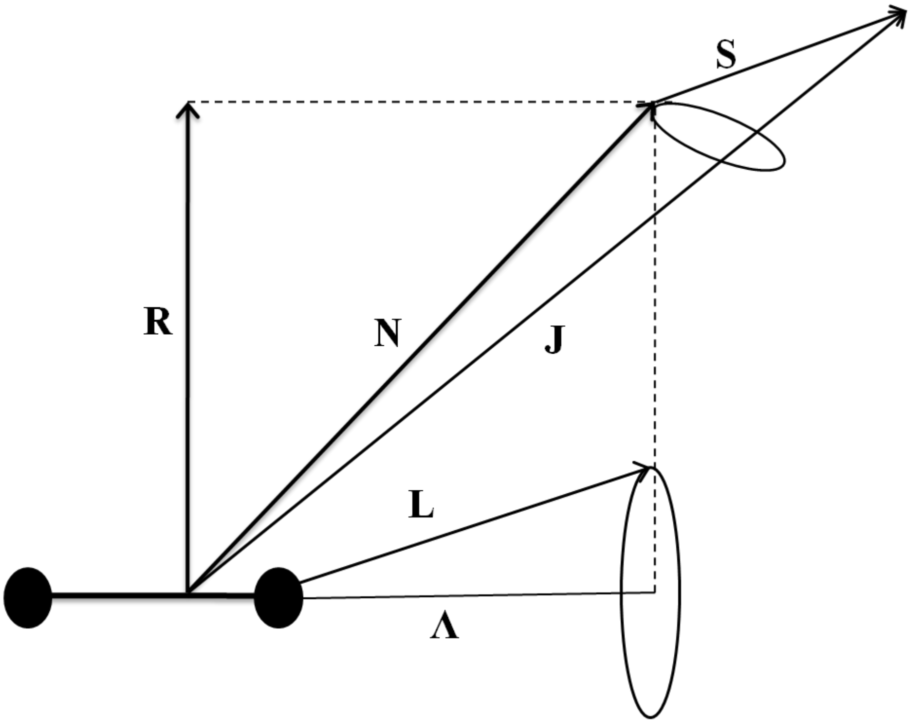

Figure 1.3. The vector diagram for Hund's case (b).

by *BN (N + 1)*, and each N-level is split into 2(2**S** + 1) or 2**S** + 1 spin components for $\Lambda \neq 0$ and $\Lambda = 0$, respectively. Hund's cases (a) and (b) are extreme cases, and there are many examples of electronic states that do not obey either coupling approximation closely. These states can be described as intermediate coupling cases.

1.2.4.3.c Hund's case (c)

In Hund's case (c), the interaction between **L** and **S** is so stronger than the interaction with internuclear axis, particularly in heavy molecules i.e. $A >> \Delta E_{\text{states}}$, here ΔE_{state} is separation between electronic states. The vector diagram for Hund's case (c) is shown in Fig.1.4. In this case Λ and Σ are not defined, rather **L** and **S** coupled to form $\mathbf{J}_a$ whose projection on internuclear axis is Ω. The Ω is then coupled to **R** to form total

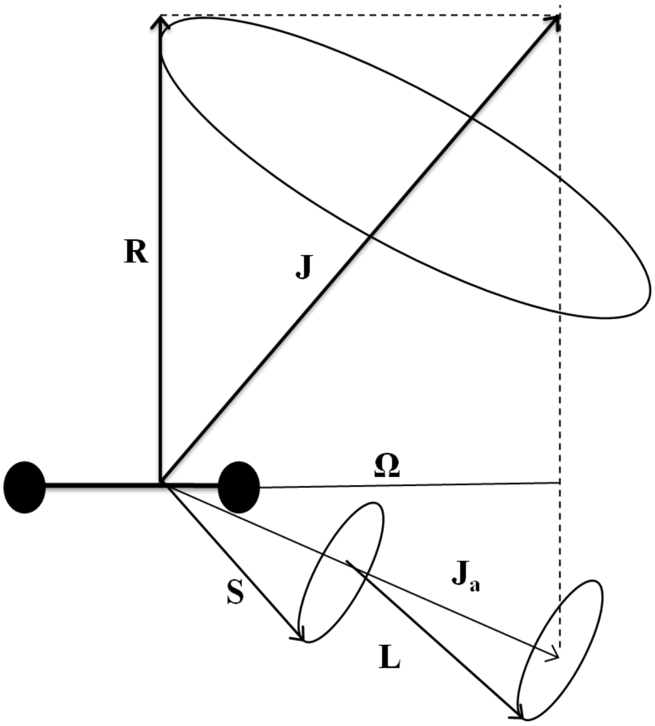

Figure 1.4.The vector diagram for Hund’s case (c).

angular momentum **J**. The "good" quantum number in Hund’s case (c) is Ω and **J**. The $^{2S+1}\Lambda_{\Omega}$ spin components of a given $^{2S+1}\Lambda$ term can be considered as independent electronic states, because these components are usually a mixture of many $^{2S+1}\Lambda_{\Omega}$ basis functions coming from different electronic states. The spectroscopic constants for different components of the same $^{2S+1}\Lambda$ term can be quite different. In fact, because of the aforementioned mixing of basis functions, the $^{2S+1}\Lambda_{\Omega}$ notation is not very appropriate for Hund's case (c) and the notation suggested by Linton *et al.* [54] is commonly used. In this notation states are labeled by $[T_0]\Omega$, where $[T_0]$ is the energy of the state in thousands of wavenumbers.

1.2.4.4 Spin-orbit components

The Hund's coupling case (a) scheme describes an angular momentum vector, Ω, which is the sum of two other vectors, Λ and Σ. It should be noted that Λ and Σ can take a range of values depending on the magnitude of **L** and **S**. For a given value of Λ, Ω can range from $| \Lambda + \Sigma |$, $| \Lambda + (\Sigma - 1) |$, $| \Lambda - \Sigma |$. Therefore, for a given value of Λ, a molecular state can be said to have 2**S**+1 spin-orbit components. As an example, for a molecular state with $\Lambda = 2$ and $S = 1$, the molecular state will be $^3\Delta_{\Omega.}$ There will be $2(1) + 1 = 3$ spin-orbit components, $|2+1| = 3$, $|2+0| = 2$, and $|2-1| = 1$ i.e., $^3\Delta_3$, $^3\Delta_2$, and $^3\Delta_1$ states. As **S** interacts with the magnetic field produced by **L** the resultant Ω vectors are forced into configurations with different energies. This can be seen pictorially in Fig.1.5. In general,

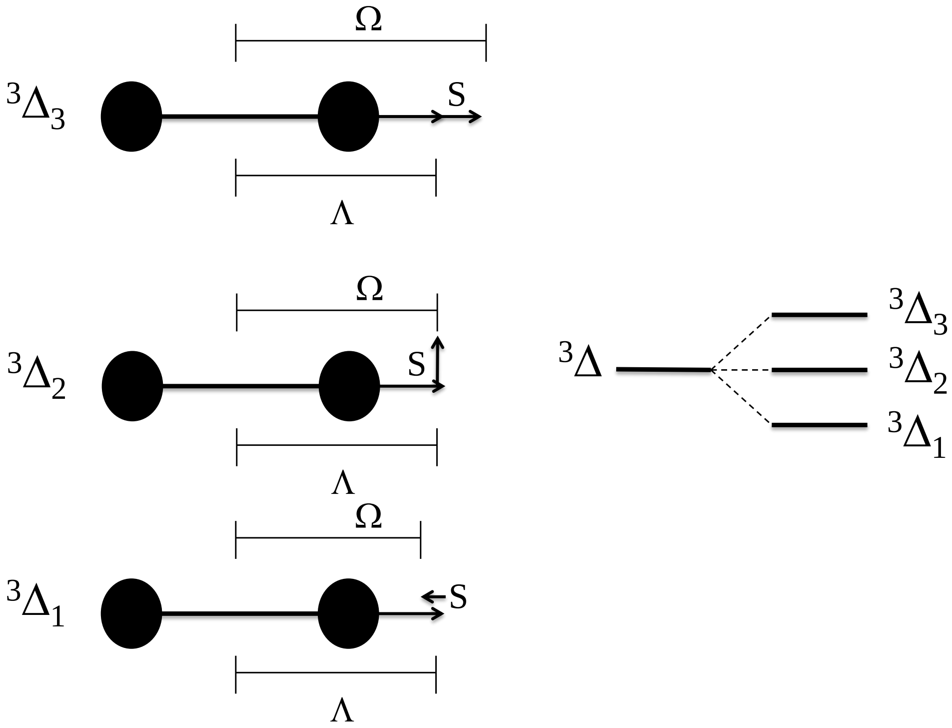

Figure 1.5. Spin-orbit splitting in a $^3\Delta$ state.

the state having the highest Ω value will lie highest in energy. Occasionally the lowest value of Ω will be highest in energy. These situations are known as inverted spin-orbit components and are denoted with an *i* subscript where the Ω usually is in the molecular state label, i.e. $^3\Delta_i$. When the system is not inverted, 'regular', the state is labelled $^3\Delta_r$.

1.2.4.5 Parity

The concept of parity in spectra of diatomic molecules makes more confusion than others. The concept of parity as it applies to molecular spectroscopy is well explained in Refs. [5,55]. The parity which we will discuss here is rotational (*e/f*) parity. If the symmetry operation is E^* and the total Hamiltonian including electronic, vibrational, and rotational parts (but not nuclear spin) is used, then one obtains total parity. The E^* operator inverts all of the coordinates of the nuclei and electrons in the laboratory frame with the origin at the center of mass that is,

$$\begin{aligned}\hat{E}^*\Psi(X_i,\ Y_i,\ Z_i) &= \Psi(-X_i, -Y_i, -Z_i) \\ &= \pm\Psi(X_i,\ Y_i,\ Z_i)\end{aligned} \tag{1.34}$$

The all (+) Ψ energy states have positive total parity, and all (–) Ψ energy states have negative total parity. Of course, the effects of $\hat{E}^*$ on the electronic, vibrational and electronic parts of the wave function need to be determined individually [5]. The total parity alternates with *J* and it is useful to factor out this alternation by introducing rotationless *e* and *f* parities.

For integral *J*,

$$\hat{E}^*\Psi = +(-1)^J\Psi \quad \text{for } e \tag{1.35}$$

$$\hat{E}^*\Psi = -(-1)^J\,\Psi \quad \text{for } f \tag{1.36}$$

For half integral *J*,

$$\hat{E}^{*}\Psi = +(-1)^{J-\frac{1}{2}}\Psi \quad \text{for } e \tag{1.37}$$

$$\hat{E}^{*}\Psi = -(-1)^{J-\frac{1}{2}}\Psi \quad \text{for } f \tag{1.38}$$

Rotationless parity is more convenient to use as, for example all rotational energy levels of a $^1\Sigma^+$ state have *e* parity, while the sign of their total parity alternates with *J*. The + ↔ − selection rule for total parity becomes *e* ↔ *e* and *f* ↔ *f* for *P* and *R* branches, while *e* ↔ *f* for Q branch.

1.3.4.6 Perturbations in the spectra of diatomic molecules

Perturbations refer to deviations from the expected results. In terms of spectroscopy, perturbations arise when spectra do not behave according to simple models. These models generally consider only the interaction between two states and the states that involved in the transition, in reality; there are finite interactions between all states of a system. Mostly these interactions are so weak as to be completely negligible and therefore can be safely ignored. In these cases, a simple model is sufficient to describe the energy levels. In other instances, the interactions become significant enough to cause deviation from the simple model. In those cases the perturbing interaction must be considered. This consideration can be simple in the case of a single interacting state or complex in the case of several interacting states. To account for interactions between states an adjustment must be made to the simple model. Once the new model has been arrived at, it must be able to describe the system equally well whether there is large perturbation (the interaction is strong) or a small perturbation (the interaction is weak) [1,55]. To fully and properly describe a molecular system one should include interaction terms describing interactions between all states, but this would make the analysis impossibly complex. Most of the time it is possible to describe the system with one or two forms of interaction. The goal is to describe the system with the minimum possible number of parameters within a pre-chosen level of accuracy as described by the root mean square deviation. In the case of a single interacting state it is often possible to account for the interaction by the inclusion of a single off-diagonal interaction term in the rotational Hamiltonian. The form of the interaction term arises from which quantum mechanical operators are required to connect the two states [1,55]. When the nature of the perturbing state is known it is an easy task to determine which operator, or operators, connect(s) the two states. If the nature of the perturbing state is unknown, the form of the interaction term is not so easy to determine. In these cases one can try to determine the effect of the perturbation on the rotational structure; for example does the perturbation has an effect which appears to depend on $J(J+1)$ or does the effect appear to be constant? If so, this may give hints as to which form the interaction term is to take. Perturbations, like spectroscopic transitions, are governed by selection rules based on the quantum numbers and symmetry properties of the states/levels involved in the interaction [1]. Interactions must take place between states that have the same total angular momentum J and the same parity (+ ↮ -). Both states must have $\Delta\Omega = 0$ or ±1. In cases where the two states have the same value of Ω, the perturbation is considered homogeneous. When the states have Ω values that differ by ±1, the perturbation is heterogeneous. The last restriction is only valid under Hund’s case (a) or (b) formalism. For Hund’s case (c), since $\mathbf{\Lambda}$ and $\mathbf{\Sigma}$ are not defined, the selection rules are based on the values of Ω ($\Delta\Omega = 0$ or ±1).

Chapter 2

Experimental set-up and Methodologies

2.1. Introduction

Over the years, a number of different strategies have been employed to produce atomic or molecular species of refractory nature in gas phase, such as thermally heated oven sources, decomposition of volatile organometallics, discharge sputtering sources and electro spray ionization to name a few. Conventionally, emission or absorption spectra recorded on photographic plate served as the main source of spectroscopic data. Metals were vaporized in high temperature ovens, and were allowed to react with various gases to form the desired molecular species [56]. Thus due to the high temperature conditions necessary for metal vapour production, the obtained molecular spectra were often complex and congested which many times led to misleading assignments [57-59]. For example, initially ScH and YH molecules [60,58] were produced in hallow cathode discharge source which is a hot source where the excited electronic states are populated. Based on transitions observed from the $^3\Delta$ state and that time erroneous *ab initio* calculations [57], authors assigned $^3\Delta$ state as the ground state for these molecules. Later by using laser vaporization technique in conjunction with supersonic expansion, Simard *et al.*[61] produced the YH molecule in free-jet at low temperature and observed transitions originating from $^1\Sigma^+$. Based on this observation they assigned the ground state as $^1\Sigma^+$ symmetry. This assignment was also supported by contemporary the high-level *ab initio* calculations [62,63] which took into consideration electron correlation effects prominent in transition metal atoms.

The spectroscopy of transition metal containing molecules has taken a big boost after the advent of Smalley laser vaporization source [64] and demonstration of generation of these molecules at low temperature [65] by combining Smalley source and chemical reaction of laser-produced metal plasma with seed gas for generating wide variety of transient molecular species of interest. Recently, a detailed review was given by M.A. Duncan [66] on laser vaporization cluster sources. This technique caught the limelight in 1985 when Smalley *et al.* [67] used laser ablation of graphite to create C_{60}, for which they got Nobel Prize in Chemistry in 1995. The capability of the pulsed laser to vaporize elements of refractory nature in conjunction with supersonic expansion in free-jet allows the formation of exotic species in the beam. Supersonic expansion is a well-known technique for cooling the internal degrees of freedom of molecules thereby simplifying the spectrum. This simplified spectra led to an unambiguous assignment of character of the ground and excited electronic states [36] which is very important for understanding the nature of the transition metal-main group element bond. We have developed this source in our laboratory [68] and used it to study variety of diatomic molecular species containing transition metal atoms.

This chapter present details of the experimental technique employed in the present work that combines the techniques of laser vaporization with supersonic free-jet and laser-induced fluorescence spectroscopy as a probe for studying electronic structure of diatomic molecules.

2.2. Experimental set-up

2.2.1. Supersonic free-jet source

A schematic block diagram of the supersonic free-jet set-up is shown in Fig. 2.1 and 2.2. The vacuum chamber is a six-port double cross built with 250 CF-F flanges. It has additional 35 CF ports to insert gauges for vacuum measurements and electrical ceramic vacuum feedthroughs and laser beams. A homemade gas pulse valve is mounted on one of the 250 CF port. The opposite port to the pulse valve is used to view the alignment of ablation laser beam on metal target. The side ports are used to insert the Nd-YAG laser for metal vaporization and the tunable dye laser beam for molecular excitation. The resulting laser-induced fluorescence is collected from the top port by collection optics and imaged on the monochromator slit. The 10 inch throat turbomolecular pump (Pfeiffer vacuum TPU 2301) backed by a rotary vane pump (Pfeiffer vacuum DUO 65) is attached to the bottom port of the chamber through a pneumatically operated gate valve. The background pressure <1 x 10^{-7} mbar is regularly obtained. A vaporization source similar

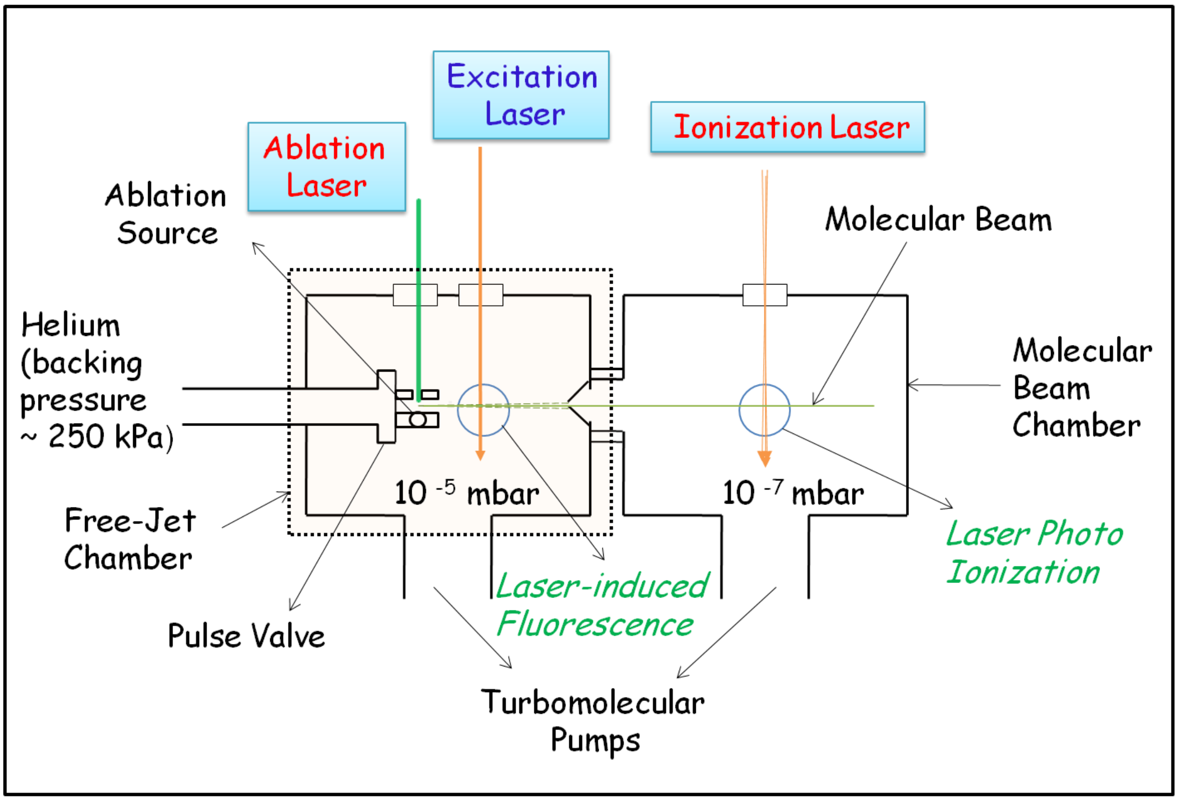

Figure 2.1. Schematic of the supersonic free-jet apparatus.

to the one used by Hopkins *et al*. [69] is fitted on the pulse valve (see Figure 2.3). The species being studied, for example La, in metal rod form having ¼ inch diameter and 50 mm length, positioned in front of a nozzle of about 400 micron diameter. The metal rod is rotated and translated back and forth by a motor driven micrometer screw. This provides

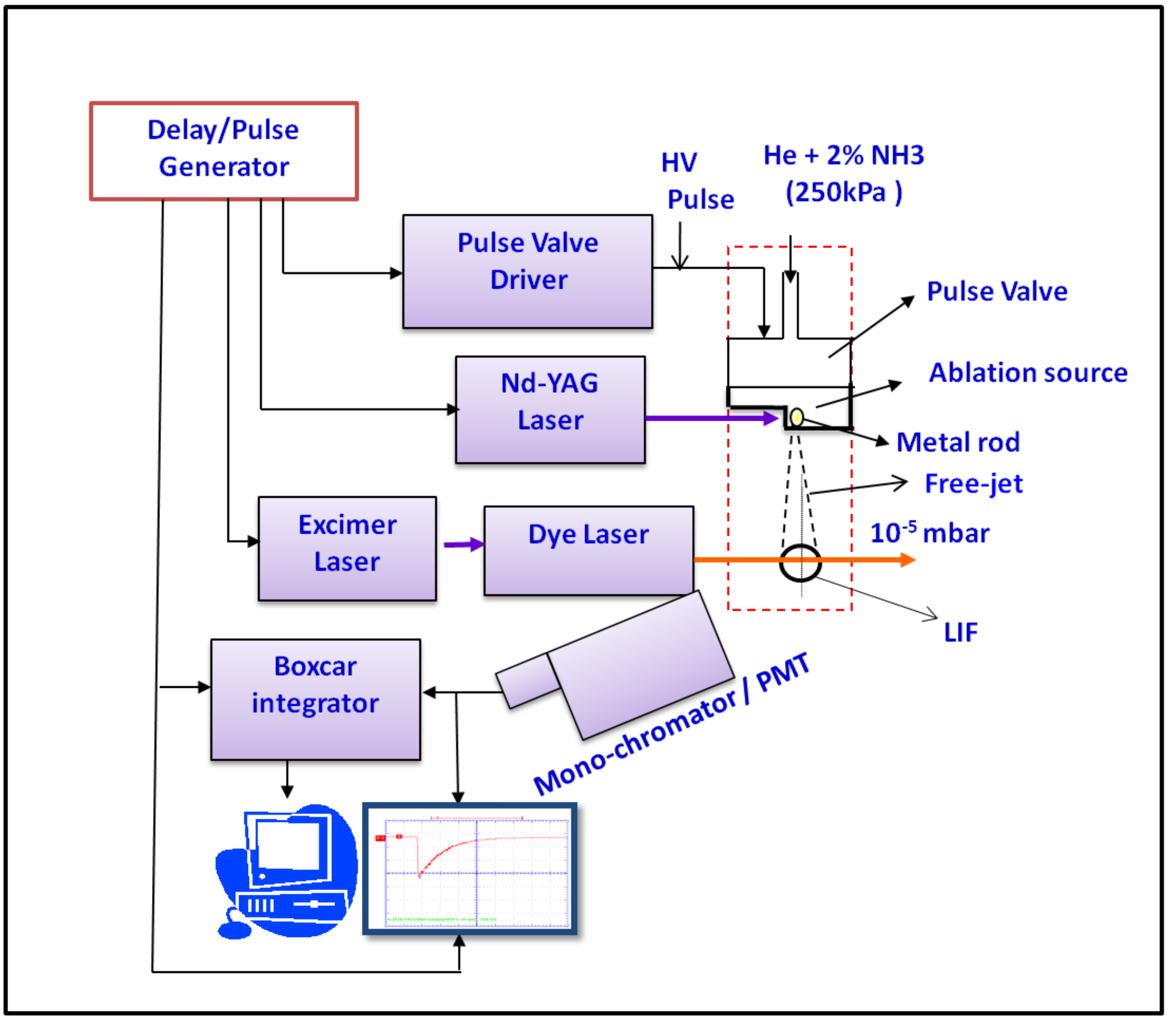

Figure 2.2. Block diagram of supersonic free-jet setup.

a fresh surface to every ablation laser pulse and a key factor in producing stable atomic or molecular species concentration in a beam. Free metal atoms and ions are generated in laser produced plasma by focusing the third harmonic of a Nd: YAG laser (Quanta System SYL 203) beam having pulse duration 8 ns and energy ~15 mJ on the metal rod.

The diameter of focal spot is ~ 1 mm. The Nd: YAG laser beam is passed through a 2 mm open channel in the vaporization source (Figure 2.3) from a side-port of the chamber. The generated hot metal plasma is reacted with 2% ammonia seeded in He emerging from the nozzle of the gas pulse valve into a channel of diameter 2 mm and length 7 mm and expanded freely into the vacuum chamber. A typical helium backing pressure of about 250 kPa (2.5 bar) is used. The base pressure in the expansion chamber is ~ 1 x 10^{-5} mbar with the pulse valve operated at 10 Hz repetition rate. The translationally cooled atoms/molecules are excited by a tunable pulsed dye laser (Coherent ScanMatePro) pumped by a XeCl excimer laser (Coherent CompexPro 201) at ~ 50 mm downstream of the nozzle. Typical pulse duration (FWHM) of the dye laser is 11 ns with spectral linewidth ~ 0.08 cm^{-1}. The laser-induced fluorescence detection is explained in detail in section 2.2.3.

The free-jet chamber is connected to another differentially pumped chamber (molecular beam chamber) as shown in Fig 2.1, where laser-photo ionization (LPI) studies are carried out using time-of-flight mass spectrometer (TOFMS). The free-jet expansion from the laser ablation source is skimmed through 2 mm diameter skimmer. The central portion of the free-jet passes through skimmer to the molecular chamber, resulting in a well collimated molecular beam. The source chamber is used for laser-induced fluorescence (LIF) and the molecular beam chamber is used for LPI studies. In the present thesis work, source chamber is only used for LIF experiments.

2.2.2. Gas pulse valve for supersonic free-jet expansion

A piezoelectric actuator driven gas pulse valve that delivered supersonic helium-jet is used in conjunction with laser vaporization source to generate cold atomic, molecular or cluster beam of refractory metals. Schematic of pulse valve/laser vaporization source is shown in Fig.2.3. We followed the design of Proch and Trickel [70] for gas pulse valve, which generated high intensity supersonic free-jet. The piezoelectric disc translator (Physics- Instrumente Model No.:P286.20) is used in this pulse valve. The adjustable plunger, which opens and closes the nozzle, is mounted on the orifice in the center of the piezoelectric disk with lock nuts. A Viton O-ring of inner diameter 1.5 mm and cross section 1.5 mm is mounted on the tip of plunger that seals the nozzle of diameter 400 μm.

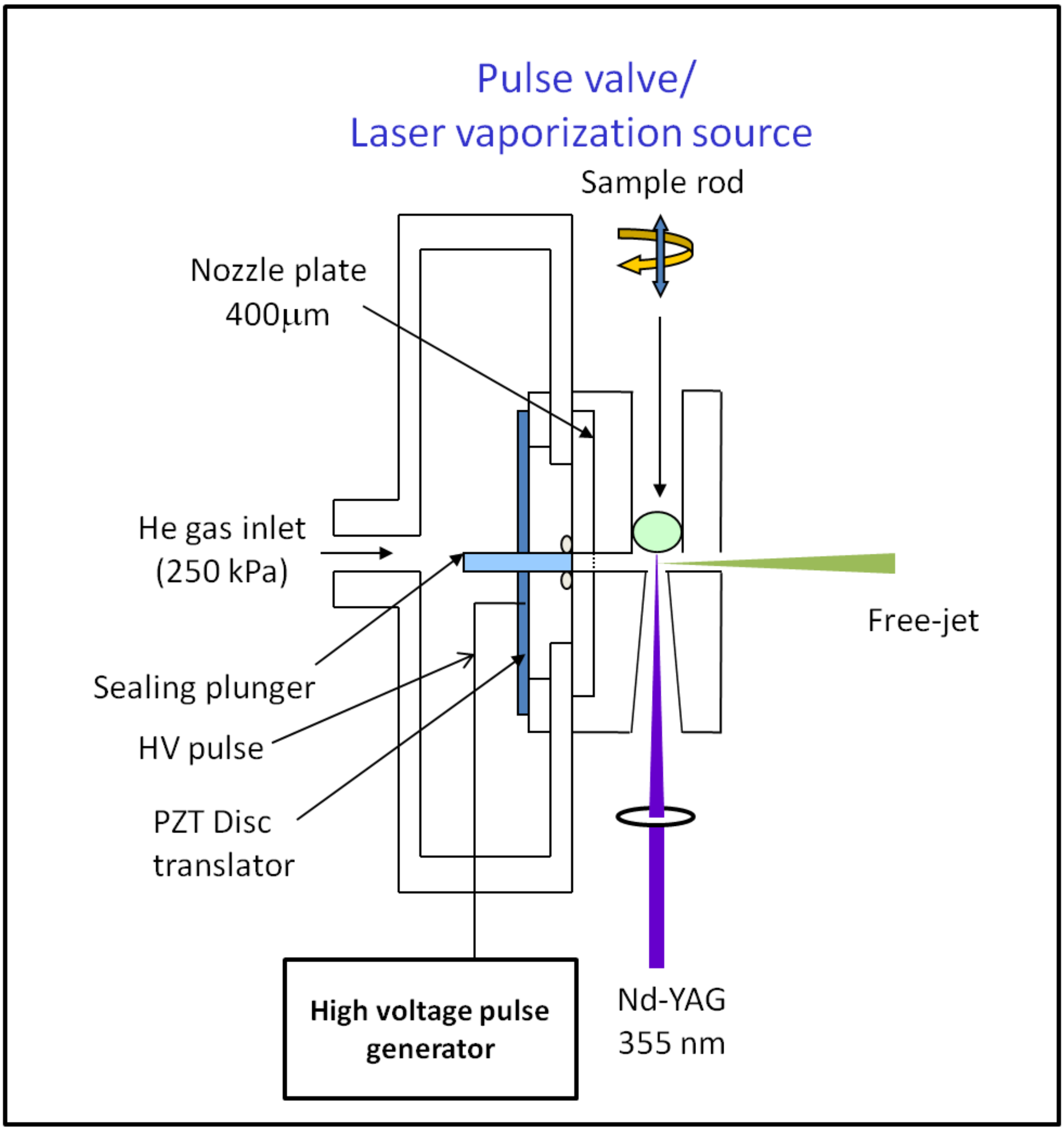

Figure 2.3. Schematic of the gas pulse valve/laser vaporization source.

The valve is driven by homemade high voltage pulse generator. The typical voltage pulse driving the valve is of ~300 μs duration and peak voltage of about 250-300 V. With this peak voltage the base pressure in source chamber is dropped from $\sim 1\times10^{-7}$ to $\sim 2\times10^{-5}$ mbar, when the valve is operated at 10 Hz repetition rate with helium stagnation pressure of 250 kPa (2.5 bar) behind the valve. The expected gas pulse width in our case is ~300 μs.

2.2.3. Fluorescence imaging and detection system

A schematic of fluorescence imaging and detection system is shown in Fig. 2.4. Various atomic/molecular species generated in the free-jet beam is excited with a tunable pulsed dye laser. The dye laser light intersects the free-jet beam orthogonally at a point about 50 mm downstream the nozzle. The delay of about ~ 25 μs is required between

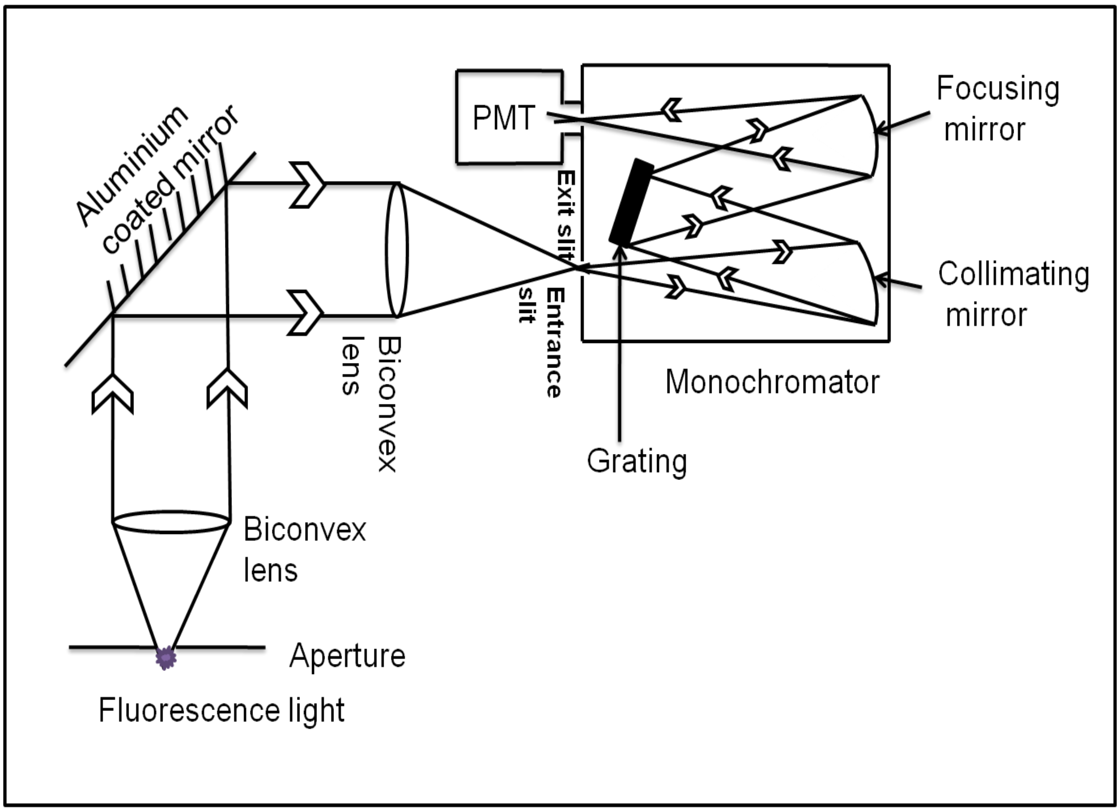

Figure 2.4. Schematic of fluorescence imaging and detection system.

ablation laser and dye laser pulse to achieve maximum fluorescence intensity. This fluorescence is collected at right angles to the plane formed by the expansion axis and the excitation axis by means of a biconvex 5 cm *f*/l quartz lens. The fluorescence spot lie at the focal point of the collecting lens. The fluorescence beam is folded by an aluminum coated mirror, and focused on an entrance slit of 0.5 meter Czerny–Turner design monochromator (Spex 270M) by another biconvex lens of focal length 30 cm. This focusing lens matches the *f/number* of monochromator. The fluorescence is detected by a Peltier cooled photomultiplier tube (Hamamatsu R943-02) having rise time of 3 ns. A black anodized cone of aperture 3 mm diameter is attached in front of the collection lens to minimize the scattered light from excitation laser falling on the photomultiplier tube (PMT). The PMT signal is then amplified with a broad-band amplifier (Femto Messtechnik, DUPVA-1-60). Gated detection technique (boxcar integrator) is used for signal processing. The boxcar integrator (Stanford Research System, SR250) is used to integrate 10-20 pulses and allows signal to be collected in a narrow adjustable gate. A data acquisition system of ScanMatePro laser is used for recording excitation spectrum and a controller system (Jobin Yvon Spex DataScan2) of the monochromator is used for recording dispersed fluorescence (DF) spectrum.

2.2.4 Time Synchronization and Optimization of LIF signal

Laser-induced fluorescence experiments are carried out using pulsed free-jet probed with pulsed lasers operated at 10 Hz repetition rate. So it is crucial that the gas pulse, ablation laser and excitation laser pulses are correctly synchronized in order to obtain an optimum laser-induced fluorescence signal. To achieve this, a delay generator (Stanford Research Systems Inc. Model DG535) is used to control the timings of various events such as firing of gas pulse valve, ablation laser and excitation laser (see Fig.2.2 and 2.5).

First the pulse valve is opened which delivers an intense gas pulse of He. After appropriate delay, laser pulse from Nd:YAG operated in 3rd harmonic wavelength ablates the metal rod to generate the metal plasma. The delay between the laser ablation pulse and He gas pulse is adjusted to generate an optimum laser driven plasma by looking at its emission intensity and also at intensity of LIF signal. The supersonic free-jet containing atoms and molecules are probed by a tunable pulsed dye laser, pumped by a XeCl excimer laser, at orthogonal to expansion axis at about 50 mm downstream from the nozzle. The delay of about 25 μs is required between ablation laser and excitation laser pulse to achieve maximum fluorescence intensity. Optimal signal strength depends on the alignment and timings of the ablation laser pulse and excitation laser pulse, concentration of seeded gas in He. When a LIF signal is observed on the oscilloscope, the timings of both ablation laser and excitation laser pulses are adjusted in order to maximize the observed signal strength. The reaction conditions are optimized by varying doping concentration of seeded gas. The ablation laser power is also varied in order to get the effective ablation which maximizes LIF signal strength. These optimizations result in the best possible signal to noise conditions.

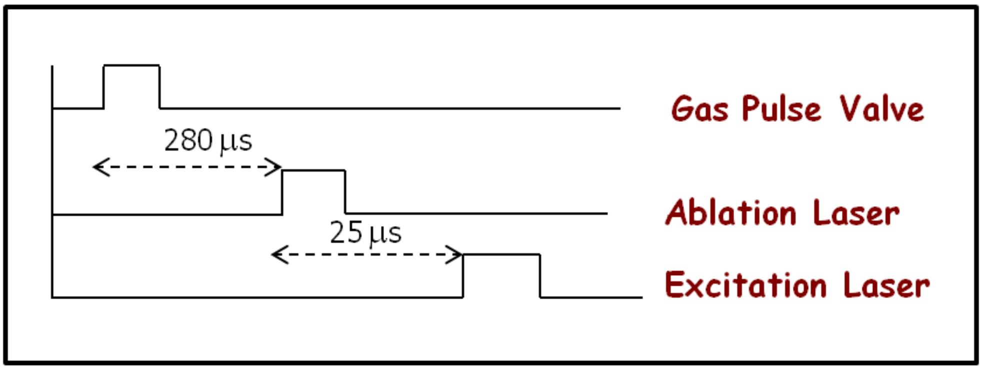

Figure 2.5. Time synchronization with Pulsed delay generator

2.3. Laser-induced Fluorescence (LIF) excitation spectrum

Laser-induced Fluorescence (LIF) is the optical emission from molecules that have been excited to higher energy levels by absorption of laser radiation. It is fundamentally an absorption measurement. The laser-induced fluorescence technique is widely used in the investigation of unstable molecular spectroscopy, from 1972, when R.N. Zare first reported this method [71]. Demtroder [72] and Andrews [73] have summarized some of the standard LIF techniques. Fig 2.6 shows a schematic diagram of the principle of laser-induced fluorescence. The laser wavelength is scanned across the spectral range of absorption lines and the total or dispersed fluorescence intensity is monitored as a

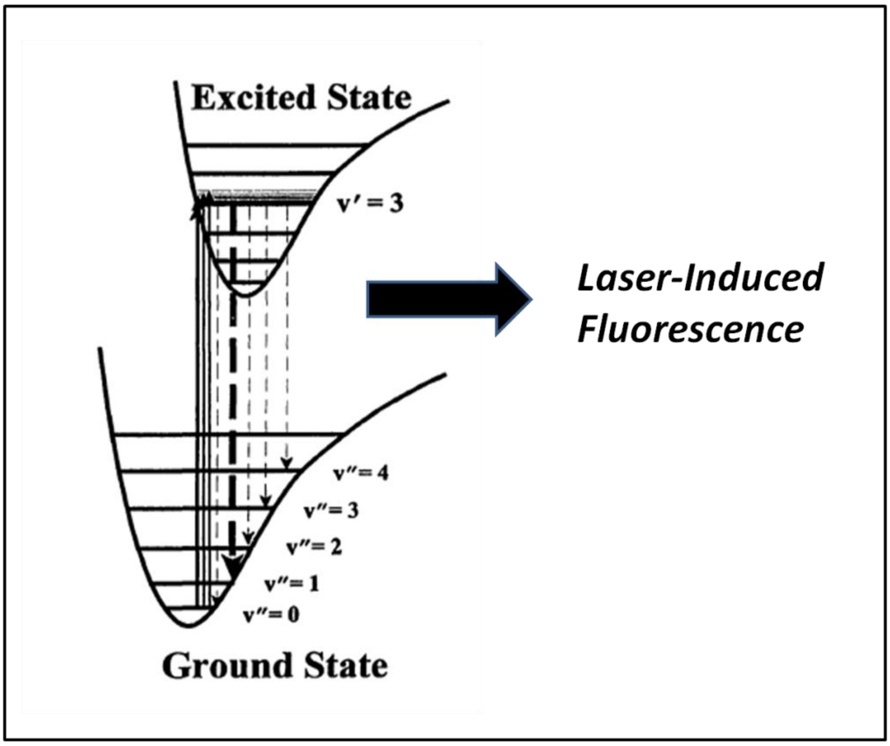

Figure 2.6. Laser-induced fluorescence technique. The monochromator is set at the fixed wavelength corresponding to the strongest fluorescence terminating either to a ground or an excited state.

function of laser wavelength. If the laser wavelength is not tuned to a specific ro-vibronic transition, then the spectral intensity is zero and no LIF signal is detected. For this reason, the LIF method is highly sensitive. In the LIF technique, a tunable dye laser is used to excite the molecules from a ground or a low-lying vibronic level to some excited state. When the laser is brought into resonance with a spectroscopic transition to an electronically excited vibronic level, molecules in the lower state will be excited to the higher state. The molecules in the excited state decay by spontaneous emission to various vibronic levels governed by the selection rules. The spontaneous fluorescence decay signal is monitored through the monochromator set at fixed wavelength corresponding to the strongest fluorescence terminating either to a ground or an excited state. Here monochromator is used as a broad band filter by setting width of the entrance and exit slits to 2.24 mm in our experiments. The excitation spectra are obtained with a typical resolution of 0.08 cm^{-1} limited by a laser line spectral width.

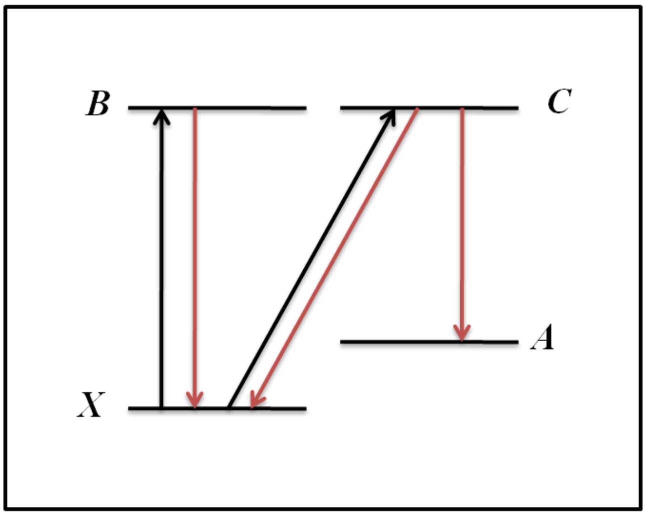

Figure 2.7. Wavelength filtering to separate overlapping excitation bands: Overlapping excitation bands can be separated by selectively monitoring the fluorescence from *C* state to *A* state. This way the excitation band due to state *C* can be filtered from *B* state.

In some cases two excitation bands overlap with on each other and it becomes difficult to assign the rotational levels to a particular electronic state with certainty. In such a case wavelength-filtering laser-induced fluorescence (WF-LIF) technique comes to rescue in certain favorable conditions. This situation is explained in Fig. 2.7. Using above technique we have separated two overlapping excitation bands of LaH to $0^+(^3\Sigma^-)$ and $^3\phi_2$ states in region 15540-15660 cm^{-1} and filtered the rotational excitation spectra belonging to $0^+(^3\Sigma^-)$-$X^1\Sigma^+$ transition from $^3\phi_2$-$a^3\Delta_1$ transition (see Chapter 3).

2.4 Wavelength Resolved Fluorescence (WRF) or Dispersed Fluorescence (DF) Spectroscopy

Wavelength Resolved Fluorescence (WRF) Spectroscopy is a very useful technique to get information on the vibrational levels of the ground state and also low-lying electronic states. The WRF spectra also provide insight into Franck-Condon overlap for the vibronic levels involved in the transition. In this technique the pulsed dye laser is tuned to a particular ro-vibronic transition and the resulting fluorescence is wavelength dispersed by a monochromator and spectrum is recorded by a scanning monochromator at reduced slit widths to improve the resolution of the fluorescence spectral lines. An illustration of the Dispersed Fluorescence (DF) technique is shown in Fig. 2.8. Many times it is essential to get rotationally resolved DF spectrum in order to get the identity on the lower electronic state. For this purpose one has to reduce the monochromator slit to improve the spectral resolution. However, many times it is not possible due to the low intensity associated with DF spectral line. In this thesis work, DF spectra of LaH and ZrN molecules were measured which gave abundant information on ground and low-lying electronic states and their identities.

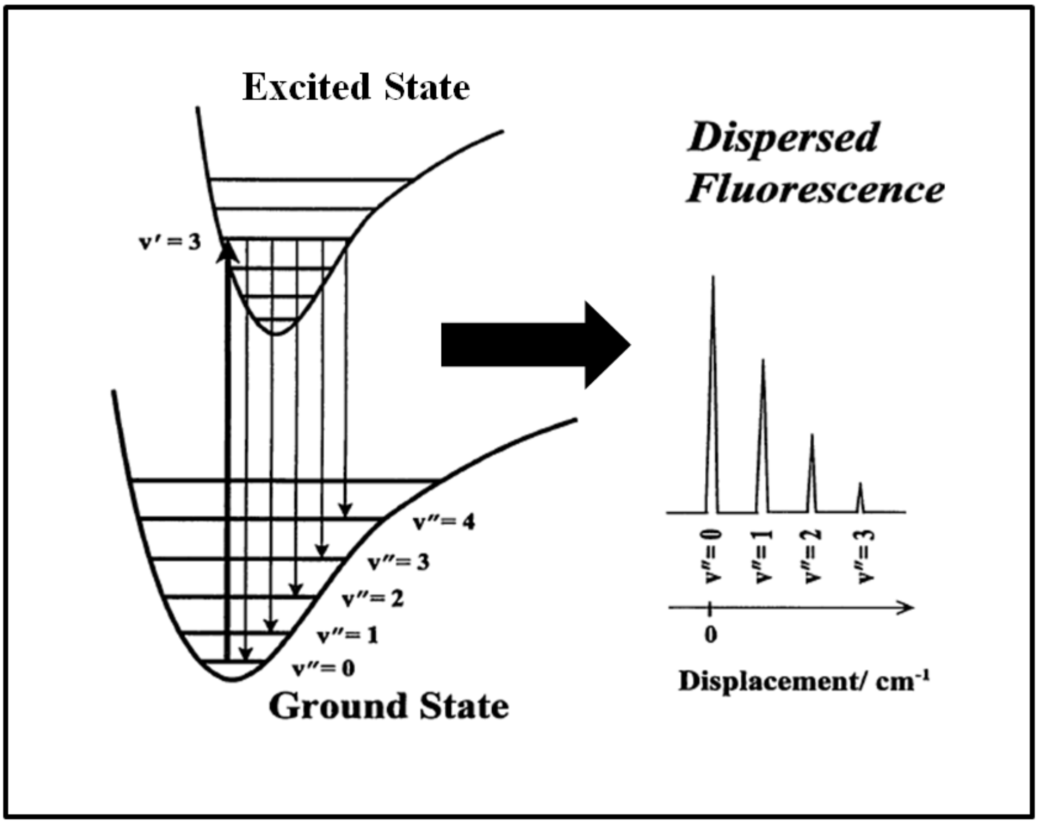

Figure 2.8. Dispersed fluorescence spectroscopy technique. The "0" on the displacement scale represents the fixed excitation wavelength of the pulsed dye laser.

2.5 Wavelength calibration of LIF excitation bands

A rotationally resolved excitation spectrum recorded with a narrow laser linewidth of 0.08 cm^{-1} requires accurate wavenumber calibration for accurate determination of the molecular constants of the electronic states involved in the transition. For this purpose reference Ne atomic lines generated from optogalvanic (OG) cell and fine frequency markers from Fabry-Perot étalon are recorded along with the uncalibrated LIF excitation spectrum as shown in the Fig.2.9. Laser light from pulsed dye laser is divided into two parts by a beam splitter. One part is sent to excite the molecular species in the free-jet chamber. Another part is again divided into two parts, out of which, one part is sent into a air spaced étalon and then onto a photodiode, and the second part is sent through an neon dc-discharge hollow cathode lamp. Laser light is transmitted through the étalon only when an integer number of half-wavelengths fit between the reflective surfaces. Therefore, as the dye laser is scanned a record of the light transmitted through the étalon displays a series of peaks (fringes). The free spectral range, which is the separation between adjacent maxima in the transmission spectrum, is used to provide a linear energy scale for the rotationally resolved spectrum. The transmission spectrum is recorded and stored along with the uncalibrated LIF signals. The monitor étalon used for this purpose

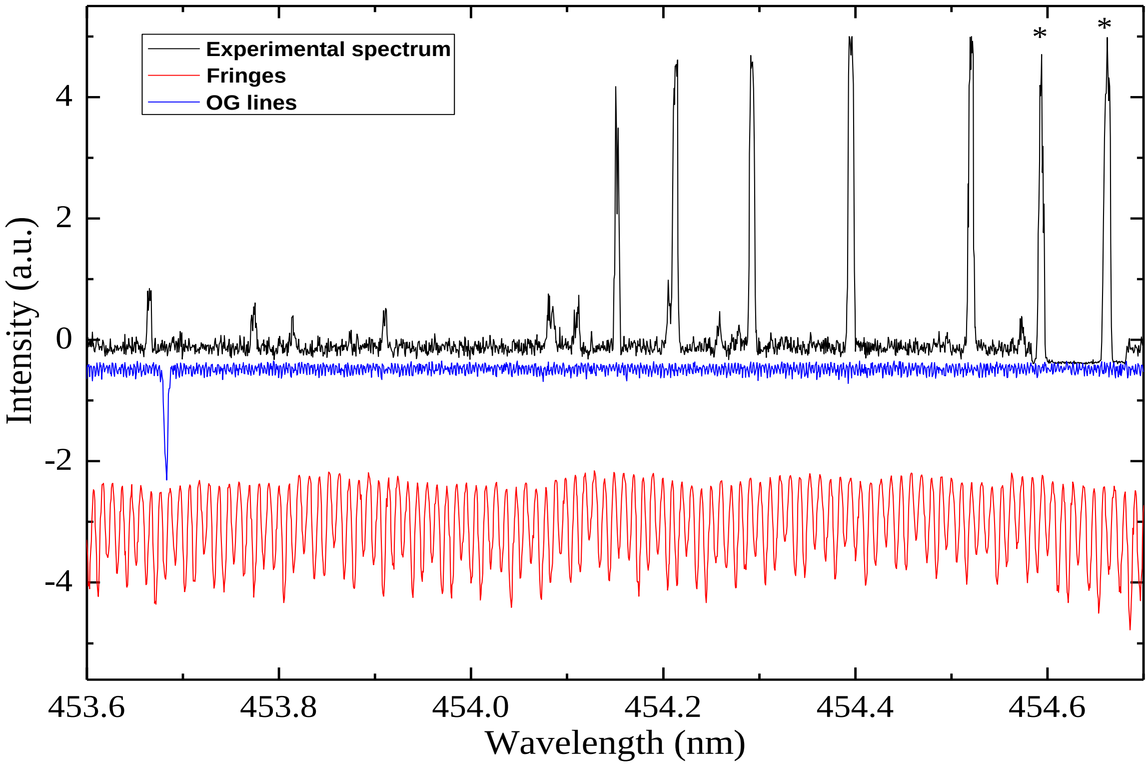

Figure 2.9. Calibration spectrum collected under rotational resolution conditions. Portion of the (0, 0) band of [21.9]$\Omega = 0^+$- $X^1\Sigma^+$ transition in LaH. The middle spectrum (blue) is an OG lines.The bottom spectrum (red) is an étalon transmission fringes with a free spectral range of 0.5 cm^{-1}. Lanthanum atomic lines are marked with *.

has a thickness of 10 mm and a free spectral range of 0.5 cm^{-1}. The second part of the dye laser beam, which is sent through Ne discharge lamp, excites the Ne spectral lines and the optogalvanic Ne spectrum is recorded. The Ne lines [74] are used for the absolute calibration. The observed spectra are also calibrated with metal target atomic lines which appeared in the LIF spectrum.

2.6 Characterization of free-jet

As we know the supersonic expansion is used to cool rotational, vibrational and electronic temperature of the molecular species. We characterize the free-jet by estimating the rotational and vibrational temperatures of the generated molecular species from their spectra. The rotational temperature of the LaH molecule was estimated from the relative intensity of the rotational lines of the band at 21970 cm^{-1} assigned as (0, 0) band of [21.9]Ω = 0^{+}–$X^{1}\Sigma^{+}$ system of LaH shown in Figure 3.13. The assignment and other details of the band will be discussed in the Chapter 3.

The relative intensities of the rotational lines in rotation-vibration band in absorption are given by [1],

$$I_{abs} = \mathrm{C}(J'+J''+1)\exp\left[-\frac{F_{v}^{''}(J'')hc}{kT}\right] \tag{2.1}$$

Here,

$$\mathrm{F}_{v}^{''}(J'') = B_{v}^{''}J''(J''+1) - D_{v}^{''}\left[J''(J''+1)\right]^{2} \tag{2.2}$$

C is constant, J', J'' are rotational quantum numbers, B'_{v}, B''_{v} are rotational constants and D'_{v}, D''_{v} are centrifugal distortion constants of upper and lower states respectively , h is plank constant, c is velocity of light, k is Boltzmann constant and T is rotational temperature.

Eq. (2.1) can be rewritten as

$$\ln\left(\frac{I_{abs}}{J'+J''+1}\right) = a - \frac{F_v^{''}(J'')hc}{kT} \tag{2.3}$$

where a is constant. Eq. (2.3) shows that, a plot of $\ln\left(\frac{I_{abs}}{J'+J''+1}\right)$ versus $F_v''(J'')$ is a straight line with slope hc/kT which determines the rotational temperature of the molecule. The plot is shown in Fig. 2.10 for *R*-branch of (0, 0) band of [21.9]$\Omega = 0^+ – X^1\Sigma^+$ system of LaH at He stagnation pressure 35 psi. The slope of 0.02077±0.00192 evaluated by least squares fitting yielded the rotational temperature 69.3±6.4 K at 35 psi He stagnation pressure. The rotational temperature was also evaluated from *P*-branch of (0, 0) band of [21.9]$\Omega = 0^+ – X^1\Sigma^+$ system and similar value is obtained as from the *R*-branch.

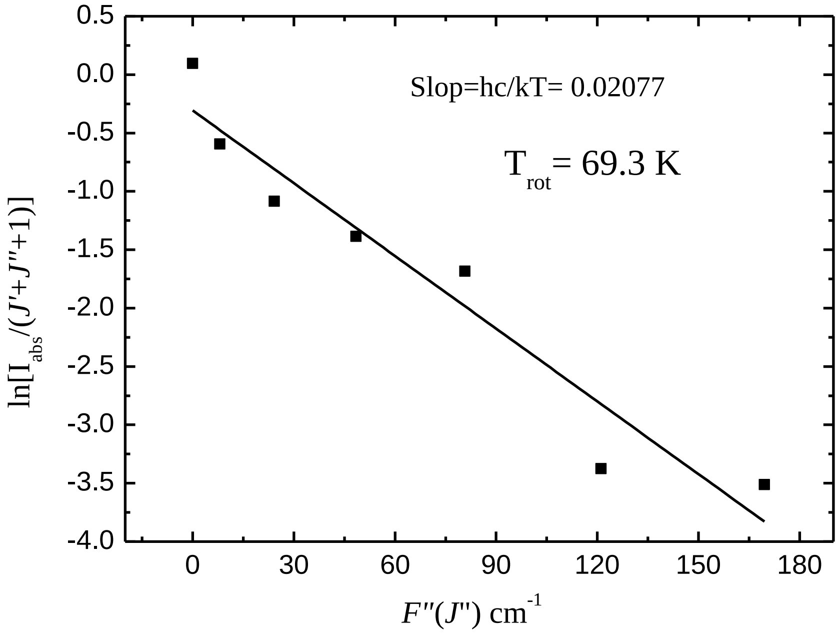

Figure 2.10. The plot of $ln[I_{abs}/(J + J + 1)]$ versus $F_v''(J'')$ for *R*-branch of (0,0) band of [21.9]$\Omega = 0^+ – X^1\Sigma^+$ system in LaH (square dots).

Similarly, the vibrational temperature was determined from the measurements of relative intensities of bands originating from $\nu = 0$ and $\nu = 1$ of ground state $X^1\Sigma^+$ of ScN molecule. The vibrational temperature measured in this case is 453 K. The low rotation, vibration and electronic temperatures associated with free-jet, simplify the spectrum to the great extent and since major population is in the ground ro-vibronic state the most intense band arise from this state and thus one can assign the ground state with most certainty.

Chapter 3

Laser-induced Fluorescence (LIF) excitation spectroscopy of jet-cooled lanthanum hydride (LaH) molecule

3.1 Introduction

The lanthanum hydrides (LaH_x) among other rare earth hydrides have recently attracted interest due to their use in semiconducting materials [75]. The basic understanding of electronic structure of diatomic transition-metal hydrides provide models for study of the metal hydrogen bond in compounds such as YH_x, LaH_x (x= 2,3), which are useful in modern technology due to their switchable optical properties [76]. Lanthanide metals are also being considered as materials for hydrogen storage [77]. It is therefore important to study electronic structure of lanthanum hydride molecule to extend our knowledge of hydrogen chemistry of these compounds. The interest in the study of these molecules stems from their importance in various area of science including astrophysics [78], catalysis [79], and organometallic chemistry [80].

Lanthanum atom has ground states electronic configuration [Xe] $5d^1 6s^2$ and is isovalent to Sc and Y, the first and simplest element among *d*-block transition metal atoms. Thus study of electronic structure of lanthanum and thus transition-metal containing diatomic molecules sheds light on the role played by *d* electrons in molecular bond. Transition metal hydrides (TMHs) are especially interesting since the bonding between the metal atom and H involves mixtures of $4d^n 5s^2$, $4d^{n+1} 5s^1$, $4d^n 5s^1 5p$ and other configurations. However, it also presents a serious challenge for both the theorist and the experimentalist because of the complex electronic structure arising from the partial occupation of open *d* orbitals [31]. From the point of view of *ab initio* studies, even a qualitatively correct results demand incorporation of large extent of electron correlation effect. Moreover, relativistic and spin-orbit effects are also known to be significant for second and third row TMHs compared to the first row. Among the transition-metals, relativistic effects are most prominent in the 5*d* series. This effect causes contraction of the *6s* and all the inner *s* orbitals. Relativistic effects also cause the 5*d* orbitals to expand due to the improved shielding by the contracted *s* orbitals. As a result, the *d* orbital contribution to chemical bonding is expected to be greater in the 5*d* transition-metal diatomics [81,82] than in those composed of 3*d* or 4*d* atoms. For above reason, experimental results on electronic states and spectroscopic properties of these molecules are of great importance as they provide a critical test of adequacy of selected methods and level of theoretical treatment. From the experimentalist point of view, the spectroscopic study of transition-metal containing diatomic molecules was hampered in the past due to their refractory nature which imposed requirement of high-temperature spectroscopic sources. The electronic structure of these molecules are much more complex due to presence of many unpaired electrons, which produces huge number of low-lying electronic states, many with very high spin multiplicity. The spectra of these types of molecules taken with high-temperature sources are very congested due to population distribution in high rotational, vibrational and low-energy excited states and also due to perturbations. This often lead to the misinterpretation of spectra and even incorrect assignment of the ground states symmetry [57,83] which is important for understanding the nature of the bond in the molecule. The systematic experimental study of these molecules however received a strong boost after the development of laser ablation source

[64] coupled with chemical reaction of laser produced metal plasma with reactant gas doped in carrier gas used for cooling in supersonic expansion [84]. This resulted in the generation of intense molecular beam of variety of exotic stable and transient species with rotational, vibrational and electronic cooling, thus simplifying the high temperature spectra which many times plagued the interpretation.

This chapter presents the experimental investigation of ground and high-energy excited electronic states of LaH molecules. The rotationally-resolved excitation spectra provided information on symmetry and molecular constants of the ground and the excited electronic states. Prior to this work there was no direct confirmation of ground state symmetry of LaH molecule. The visible electronic spectra of LaH molecule were known since 1975, when a number of bands were observed by Bacis *et al.* [83] in the 450 to 660 nm spectral region. These bands were classified [83] into several electronic transitions which were assigned as $^3\Phi$-$^3\Delta$, $^1\Delta$-$^1\Pi$, and $^1\Sigma$-$^1\Pi$. Based on primitive and erroneous *ab initio* calculations available at that time for isovalent ScH [57], Bernard and Bacis [83] suspected that LaH probably had a $^3\Delta$ ground state. Later, high level *ab initio* calculations by Das and Balasubramanian [85] included relativistic and electron correlation effects and predicted $^1\Sigma$ state as the ground state with a low-lying $^3\Delta$ as the first excited state. In addition, they predicted energies and spectroscopic properties of many low- and high-energy electronic states of LaH. Subsequently, Ram and Bernath [86] reported the observation of $A^1\Pi$-$X^1\Sigma^+$ and $d^3\Phi$-$a^3\Delta$ system of LaH and LaD in infrared region using Fourier transform emission spectroscopy. They reassigned two singlet transitions, $^1\Sigma$-$^1\Pi$ and $^1\Delta$-$^1\Pi$, observed by Bernard and Bacis [83] respectively to 0^+-$a^3\Delta_1$ and $^3\Phi_2$-$a^3\Delta_1$ and thus reported the assignment of $^3\Delta_1$ component which was observed but assigned incorrectly as $^1\Pi$ in ref. [83]. In the absence of observation of intercombination transition, Ram and Bernath [86] could not establish the singlet-triplet energy interval between the $X^1\Sigma^+$ and $a^3\Delta$ state. This restricted them from having direct experimental evidence that the $^1\Sigma^+$ state observed in the $^1\Pi$-$^1\Sigma^+$ system was the ground state of LaH. The assignment of $^1\Sigma^+$symmetry to the ground state by Ram and Bernath [86] was rather indirect and was based on the *ab initio* calculations by Das and Balasubramanian [85] and comparison with isovalent YH [87] and LaF [88,89]. Bernard and Chevillard [90] have observed a $C^1\Sigma^+$ state at 10150.9 cm^{-1}, which was predicted to lie at 13025 cm^{-1} [85]. Koseki *el al.* [91] have calculated potential energy curves and predicted dissociation energies, equilibrium distances, electronic transition energies with transition dipole moments, harmonic frequencies etc. for several low lying spin-mixed states of group 3 and 5 transition-metal hydrides using both effective core potential and all-electron approaches. More recently, Mahmoud and Korek have investigated 24 low-lying molecular states of the LaH molecule via the CASSCF/MRCI method [92]. Several other *ab initio* studies predicted $^1\Sigma^+$ symmetry for the ground state and reported the molecular constants [93-98].

The electronic spectrum of LaH is expected to be similar to that of isovalent ScH and YH molecules. The ground state symmetry for ScH and YH molecules was confirmed experimentally as well as theoretically as $X^1\Sigma^+$, arising from $1\sigma^2 2\sigma^2$ electronic configuration. Many low- and high-energy excited electronic states in ScH [40,99,100] and YH [87, 101-103] have been observed and are shown in Fig. 3.1 and Fig.3.2. The term energies of all observed electronic states of ScH, YH are listed in Table 3.1 along with few known observed electronic states in the LaH molecule prior to present work.

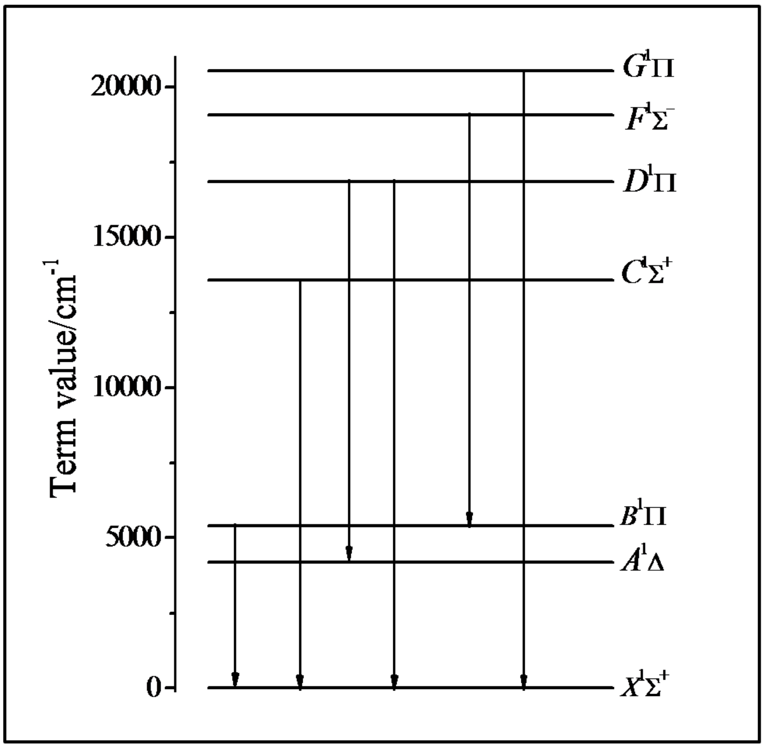

Figure 3.1. Observed singlet electronic states in ScH Molecule.

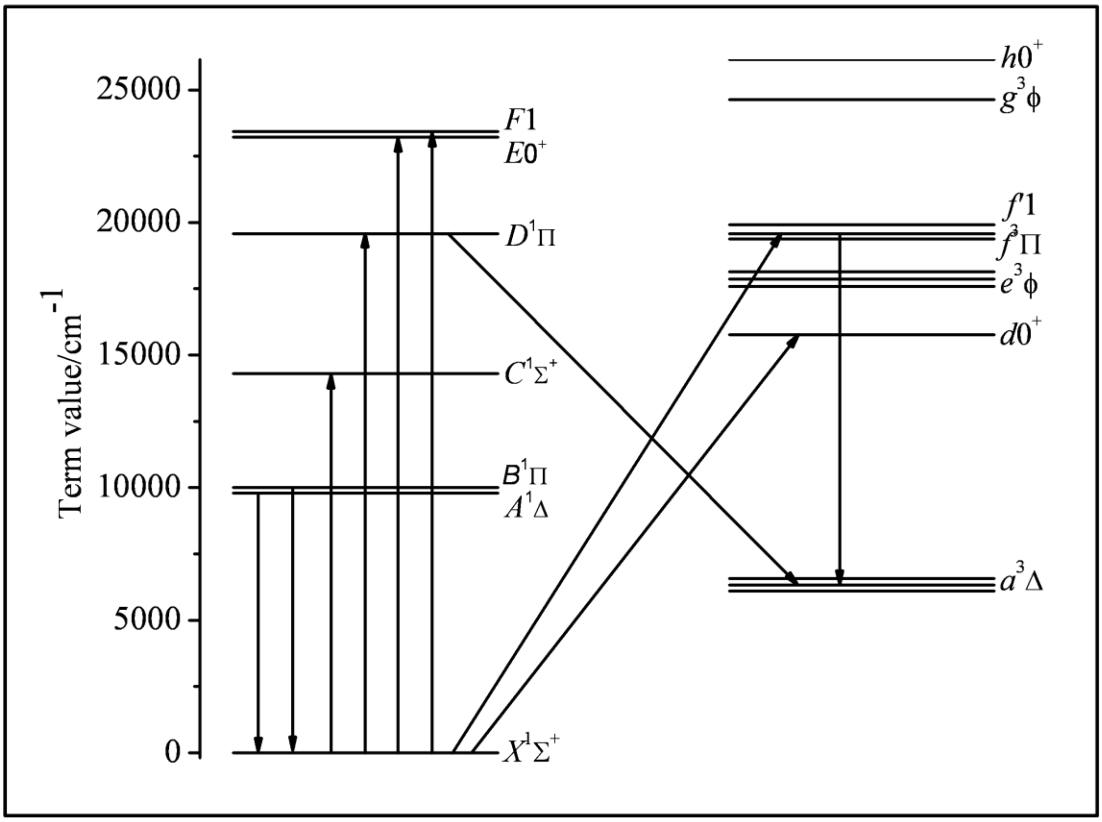

Figure 3.2. Observed singlet and triplet electronic states in YH Molecule.

Table 3.1.Term energies of all observed electronic states of ScH, YH along with few known observed electronic states prior to present work in LaH

Observed electronic states	ScH[a]	YH[b]	LaH[c]
	T_v (cm^{-1})	T_v (cm^{-1})	T_v (cm^{-1})
$X^1\Sigma^+$	0.0	0.0	0.0
$^3\Delta_1$	a[d]	6205(10)	x[e]
$^3\Delta_2$	-	6338(10)	y[e]
$^3\Delta_3$	-	6562(10)	z[e]
$A^1\Delta$[f]/$A^1\Pi$[g]	4185.3804(24)	9880.4094(316)	4533.55933(80)
$B^1\Pi$	5404.1857(12)	9880.9563(319)	-
$C^1\Sigma^+$	13574.2537(16)	14295.395(10)	10150.944(6)
$d0^+$	-	15756.4251(49)	-
$e^3\phi_2$	-	17583(10)	x+ 5955.8568(16)
$e^3\phi_3$	-	17867(10)	y+ 6238.3768(8)
$e^3\phi_4$	-	18146(10)	z+ 6306.6757(15)
$f^3\Pi_1$	-	19381.352(3)	-
$D^1\Pi$	16845.6112(23)	19573(1)	-
$f^3\Pi_2$	-	19574(1)	-
$f'\,1$	-	19742.734(2)	-
$E0^+$	-	23213.3(1)	-
$F^1\Sigma^-$[h]/$F1$[i]	19071.6409(24)	23426.5(2)	-
$g^3\phi_2$	a+17914.50(4)	-	x+15618.8
$g^3\phi_3$	-	-	y+16007
$g^3\phi_4$	-	24630(10)	-
$h0^+$	-	26136(10)	x+18595.1
$G^1\Pi$	20546.9162(38)	-	-

[a] Ref.[40,99,100]
[b] Ref. [87,101,103]
[c] Ref. [83,86,90]
[d] Ref. [40]
[e] Value undermined
[f] Electronic state of ScH and YH
[g] Electronic state of LaH
[h] Electronic state of ScH
[i] Electronic state of YH

Das and Balasubramanian [85] have predicted number of low- and high-lying exited electronic states in LaH molecules and are shown in Fig.3.3. Koseki *et al.* [91] has also calculated electronic transition energies in the infrared and visible regions. Prior to the present work, few of these predicted electronic excited states and transitions were observed in infrared and visible [83,86,90] and are shown by dashed arrow lines in Fig.

3.15. However, many of the electronic states observed in isovalent ScH and YH molecules and also predicted excited electronic states and transitions connecting them in the visible region with a large transition dipole moments in LaH [85,91] are still unobserved. Moreover, the vibrational frequencies in gas phase for LaH in both the ground and the excited electronic states are not known due lack of observation of off-

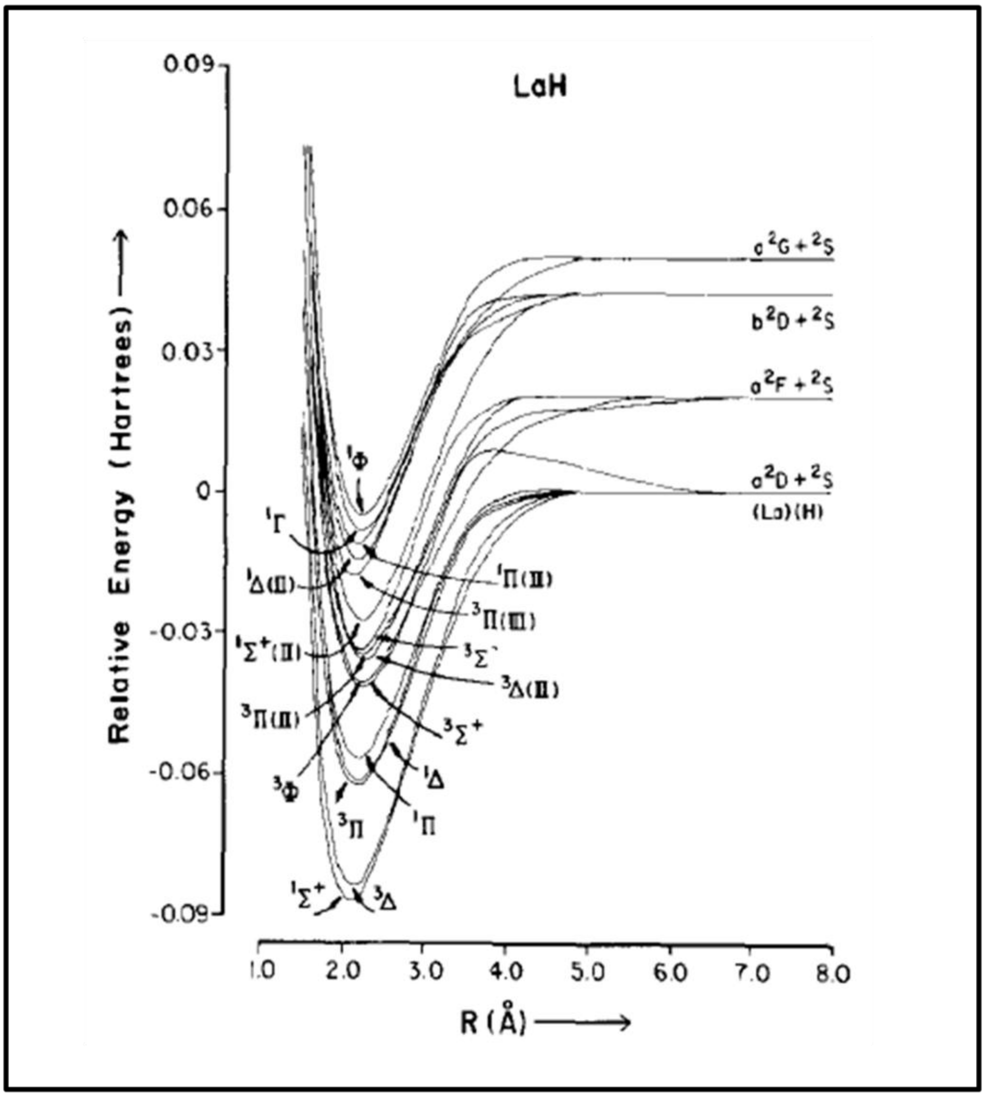

Figure 3.3. Predicted potential energy curves for low-lying electronic states in LaH molecule.[Chem. Phys. Lett. **172,** 372 (1990)]. [Energy conversion, 1 Hartree = 27.212 eV]

diagonal bands ($\Delta\nu \neq 0$). Even though a few states have been observed and assigned, important information of energy linkage between singlet-triplet manifold, is missing in LaH. Lack of this information left the energy of the whole stack of triplet states unknown with respect to the singlet states. Above mentioned shortfalls in the spectroscopic data of LaH motivated us to take up the laser-induced fluorescence (LIF) studies in supersonic free-jet in order to shed more light on the electronic structure of LaH in the low- and high-energy region which may also serve as a test of adequacy for present level *ab initio* results.

3.2 Experiment

The LaH molecules are produced in a supersonic free-jet apparatus, details of which are discussed in chapter 2. In brief, a rotating and translating lanthanum metal rod of 99.9% purity is ablated with the third harmonic beam (354.7 nm, ~10-15 mJ/pulse) of a Nd: YAG laser focused to an ~1 mm^2 spot. The laser produced lanthanum metal plasma reacted with the 2% ammonia seeded in He emerging from a pulse valve under a backing pressure of 275 kPa (2.75 bar). The products of the reaction are expanded into vacuum, cooling the internal degrees of freedom of the molecules and are probed at right angle to the supersonic expansion axis about 50 mm downstream of the nozzle by an excimer pumped tunable pulsed dye laser. The resulting laser-induced fluorescence is imaged on an entrance slit of a monochromator equipped with a Peltier cooled photomultiplier tube. An output signal from the photomultiplier is amplified by a 1 GHz bandwidth amplifier, integrated by a gated integrator, and stored on to a computer. Excitation spectra are obtained by scanning the pulsed dye laser frequency and recording the fluorescence intensity through the monochromator set at fixed wavelength corresponding to the strongest fluorescence terminating either to a ground or an excited state. Here monochromator is used as a broad band filter by setting width of the entrance and exit slits to maximum of 2.24 mm. The excitation spectra are obtained with a typical resolution of 0.08 cm^{-1}. Transition wavenumbers are calibrated by the Fabry-Perot interference fringes and the laser wavelength calibration facility of a dye laser which utilizes Ne optogalvanic spectral lines as well as by the known atomic lines of La I [104] appeared in the spectra with an absolute precision of ~0.1 cm^{-1}. Fabry-Perot interference fringes were used as fine frequency markers for interpolation of wavenumber. Radiative Lifetimes of the excited electronic states are also recorded by acquiring the fluorescence decay curve on a 200 MHz digital storage oscilloscope having sampling rate of 2 Giga-samples/s and rise time less than 2 ns. The decay curve is averaged for 128 shots in order to obtain a good signal to noise ratio.

3.3 Data analysis and results

3.3.1 Appearance of the spectra

Lanthanum has one major naturally occurring isotope, ^{139}La having abundance of 99.91% and naturally abundant ammonia were used in experiment. Thus excitation spectra of only the ^{139}LaH isotopomer were observed in our experiments. The spectra attributed to LaH were observed in the range 15500-22150 cm^{-1}, though search scans covering the range 13300-22500 cm^{-1}. Total ten excitation bands, clustered in five groups with origins at 15619, 15623, 17398, 17549, 18509, 18595, 19972, 20042, 21970 and 22100 cm^{-1} were observed. The bands with origin at 15619 and 18595 cm^{-1} were observed earlier by Bernard and Bacis [83] and reassigned by Ram and Bernath [86] respectively as (0,0) bands of $^3\Phi_2$-$a^3\Delta_1$ and 0^+-$a^3\Delta_1$ system. The other eight bands were observed for the first time. A group of dispersed fluorescence lines appeared for some of the excitation bands and not in others. We took advantage of these patterns to record the wavelength-filtered excitation spectra [105] explained in detail in chapter 2 in order to avoid the interference from overlapping bands by collecting fluorescence at two different suitable wavelengths.

Five newly observed bands at 17398, 17549, 18509, 19972 and 20042 cm^{-1} showed a single *P*, a single *R* and a single but intense *Q* branch ($\Delta\Lambda = \pm 1$ transition), however other three new bands at 15623, 21970 and 22100 cm^{-1} showed only *P* and *R* branches ($\Delta\Lambda = 0$ transition). The *R* branch was significantly more intense than the *P* branch for 17398, 17549, 19972 and 20042 cm^{-1} bands. This indicated that these are $\Delta\Lambda = +1$ type transitions. The intensities of bands with band origin at 17398, and 17549 cm^{-1} were several times stronger than that of the bands at 15623, 18509, and 18595 cm^{-1} among which 15623 cm^{-1} band was the weakest. The 17549 cm^{-1} band was stronger by approximately 2 times than the 17398 cm^{-1} band, however 18509 cm^{-1} band was about 1.5 times stronger than the 18595 cm^{-1} band. The band at 15623 cm^{-1} was 5 times weaker than the neighboring band at 15619 cm^{-1}. The band at 22100 cm^{-1} is 1.5 times stronger than the band at 21970 cm^{-1}.The rotational lines with maximum quantum number (J_{max}) observed in these bands is listed in Table 3.2. The wavenumbers of observed rotational lines with their assignments of all these band of LaH molecules are given in Appendix A.

Table 3.2. The rotational lines with maximum rotational quantum number (J_{max}) observed in new bands of LaH.

Band origins (cm^{-1})	***P*(*J*)**	***R*(*J*)**	***Q*(*J*)**	**Type of transition**
15623	8	5	-	$\Delta\Lambda = 0$
17398	10	13	13	$\Delta\Lambda = 1$
17549	13	11	12	$\Delta\Lambda = 1$
18509	9	5	4	$\Delta\Lambda = -1$
19972	9	5	9	$\Delta\Lambda = 1$
20042	16	14	14	$\Delta\Lambda = 1$
21970	7	6	-	$\Delta\Lambda = 0$
22100	12	10	-	$\Delta\Lambda = 0$

3.3.2 Assignments of bands

The band origins, their assignments and radiative lifetimes of the associated upper states of the newly observed bands of LaH are listed in Table 3.3. The assignment of bands, which is discussed below in detail, was based on the observation of number of branches, combination differences for the lower state, relative band intensity and radiative lifetimes. Rotational quantum number assignments of the P and R branches which are listed in Appendix A were carried out using combination differences (CD) method. The CD for lower state defined by following equations,

$$R(J-1) - P(J+1) = F_v''(J+1) - F_v''(J-1) = \Delta_2 F''(J) \tag{3.1}$$

$$\Delta_2 F''(J) = 4B_v''\left(J+\frac{1}{2}\right) - 8D_v''(J+\frac{1}{2})^3 \tag{3.2}$$

where B_v'' , D_v'' are the rotational constant and its higher-order correction. However, the assignments of the Q branches were based on the observation of the first line because no corresponding branches terminating on the levels with same symmetry of the upper states were present in the spectra. Combination differences for the lower state of the bands 15623, 17398, 17549, 20042, 21970 and 22100 cm^{-1} coincided within the experimental precisions with those of the $\nu = 0$ level of the $X^1\Sigma^+$ state observed by Ram and Bernath [86] and are shown in Fig. 3.4. For the weak band at 19972 cm^{-1}, lower state combination differences coincided with the $\nu = 1$ level of the $X^1\Sigma^+$ state.

Since our spectra were obtained in a jet-cooled molecular beam where the population is concentrated in $\nu = 0$ state of the ground state and considering the high intensity for the 17398, 17549, 20042, 21970 and 22100 cm^{-1} bands, we are entitled to conclude that the $X^1\Sigma^+$ state, first observed by Ram and Bernath [86] as the lower electronic state of the $A^1\Pi$-$X^1\Sigma^+$ band, is indeed the ground state of the LaH molecule. Due to the unavailability of isotopically enriched deuterated ammonia (ND_3) in our laboratory, isotope shift studies for vibrational quantum number assignments of the upper electronic states could not be carried out. However, our assignment of the ν' = 0 levels was based on the observation of bands on the lowest wavenumber side. Since no bands originating from ν = 0 of the $X^1\Sigma^+$ state could be observed to the red of the bands at 15623, 17398, 17549, 20042, 21970 and 22100 cm^{-1}, these bands were assigned the ν' = 0 vibrational quantum number in the upper electronic states.

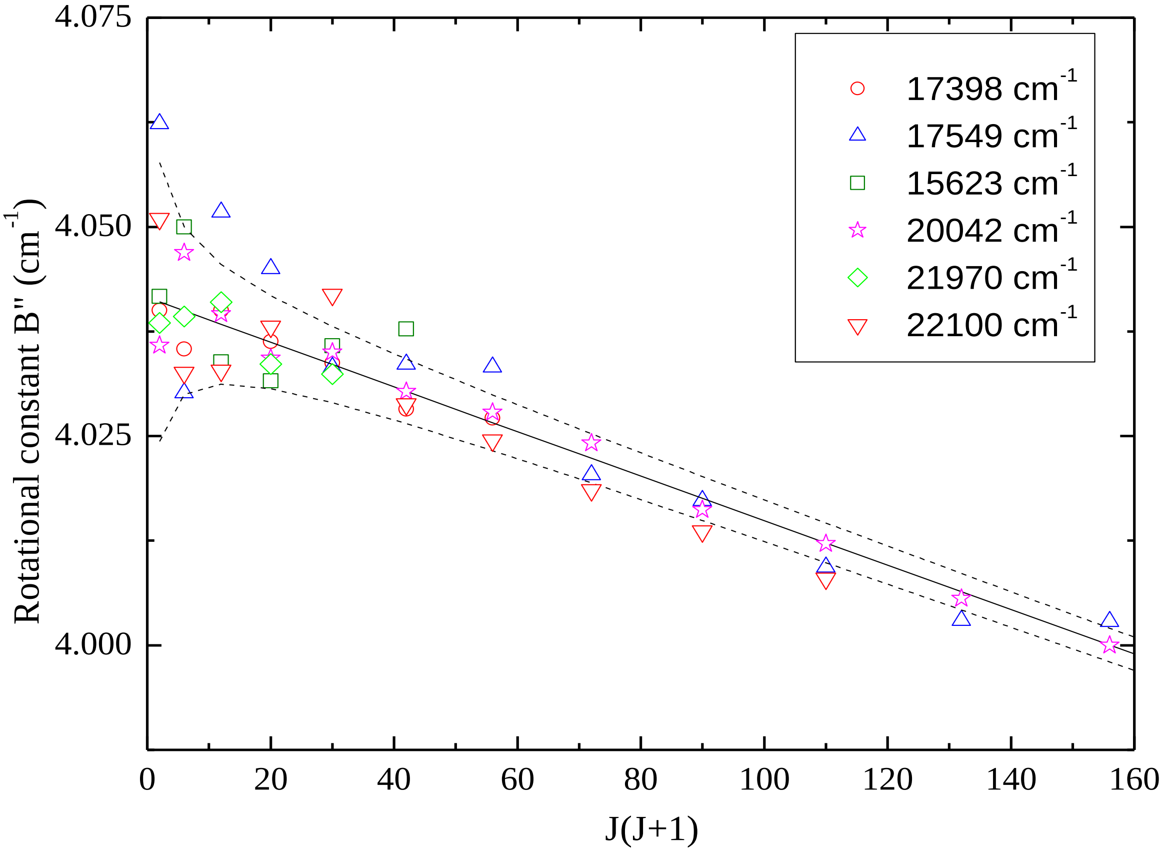

Figure 3.4. Graphical determination of the ground state rotational (B_0) and centrifugal distortion (D_0) constants from combination differences of different bands: square-15623 cm^{-1} ((0, 0) $0^+(^3\Sigma^-)$–$X^1\Sigma^+$), circle-17398 cm^{-1} ((0, 0) $D1$– $X^1\Sigma^+$), triangle-17549 cm^{-1} ((0, 0) $E1$– $X^1\Sigma^+$) band, star -20042 cm^{-1} ((0, 0) Ω = 1– $X^1\Sigma^+$) band, rhombus-21970cm^{-1}((0, 0) $\Omega = 0^+$– $X^1\Sigma^+$) band and inverted triangle-22100 cm^{-1} ((0, 0) $\Omega = 0^+$– $X^1\Sigma^+$) band. The solid straight line connects points calculated using the B_0, D_0, and H_0 values taken from

Ref. [86] and the dashed line represents the error around solid line corresponding to experimental precision of 0.1 cm^{-1}.

Table 3.3. Band origins, vibronic assignments and excited state lifetimes of the LaH molecule.

Band Origin (cm^{-1})	**Assignment**	ν'–ν''	**Lifetime (ns)**
15618.76(7)[a]	$^3\Phi_2 - {}^3\Delta_1$ [a]	0 - 0	39(2)
15622.86(3)	$0^+(^3\Sigma^-) - X^1\Sigma^+$	0 - 0	192(3)
17397.94(2)	$D1 - X^1\Sigma^+$	0 - 0	42(2)
17549.05(5)	$E1 - X^1\Sigma^+$	0 - 0	46(3)
18508.79(5)	$\Omega' = 0 - \Omega'' = 1$	–	13.6(5)
18595.10(1)[a,b]	$0^+ - {}^3\Delta_1$ [a]	0 - 0	5.7(12)
19972.00(2)	[20.0]$\Omega = 1 - X^1\Sigma^+$ [c]	1 - 1	23.0 (8)
20041.96(1)		0 - 0	19.7 (16)
21970.71(2)	[21.9]$\Omega = 0^+ - X^1\Sigma^+$ [c]	0 - 0	37.1(38)
22100.31(4)	[22.1]$\Omega = 0^+ - X^1\Sigma^+$ [c]	0 - 0	39.5(22)

[a] Observed by Bernard and Bacis [83], assigned by Ram and Bernath [86].
[b] Value taken from Bernard and Bacis [83].
[c] Adopted Linton *et al.*[54] notation.

3.3.2.1 The $0^+(^3\Sigma^-)$–$X^1\Sigma^+$ system: Observation of the first intercombination transition in LaH

The relatively feeble intensity band at 15623 cm^{-1} (lower pane spectrum of Fig.3.5) was filtered from the overlapping intense band at 15619cm^{-1} (upper pane spectrum of Fig. 3.5) by suitably parking the monochromator at a wavelength where the 15619 cm^{-1} band did not show DF. The DF spectrum from the band at 15619 cm^{-1} emits fluorescence back to the excitation wavelength only and is shown in Fig. 3.6. However, the DF spectrum from the band at 15623 cm^{-1} emits fluorescence at 1387 cm^{-1} red to the excitation wavelength, in addition to excitation wavelength. The separation of 1387 cm^{-1} matches with the first vibration quanta ($\Delta G_{1/2}$) of the ground state and is shown in Fig. 3.7. Thus by parking the monochromator at 1387 cm^{-1} red to the excitation laser, the weak band at 15623 cm^{-1} was filtered from an overlapped strong intense band at 15619 cm^{-1}. The energy level excitation and emission scheme for wavelength filtered-LIF technique is shown in Fig. 3.8.

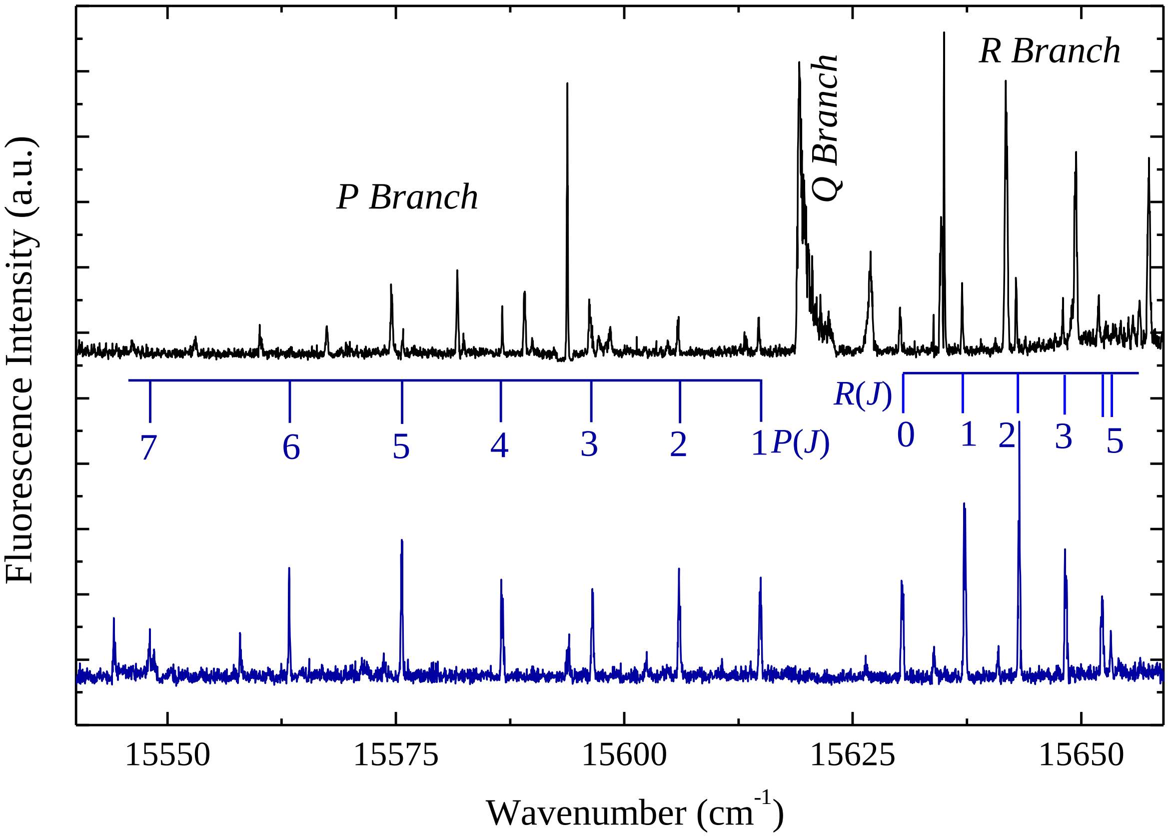

Figure 3.5. The upper spectrum is rotational structure of (0,0) band of $^3\Phi_2$-$^3\Delta_1$ system observed by Bernard and Bacis [83] at 15619 cm^{-1} mixed with (0, 0) band of $0^+(^3\Sigma^-)$–$X^1\Sigma^+$ system and the lower spectrum is the wavelength filtered spectrum of the (0, 0) band of $0^+(^3\Sigma^-)$–$X^1\Sigma^+$ system of jet-cooled LaH molecule at 15623 cm^{-1}.

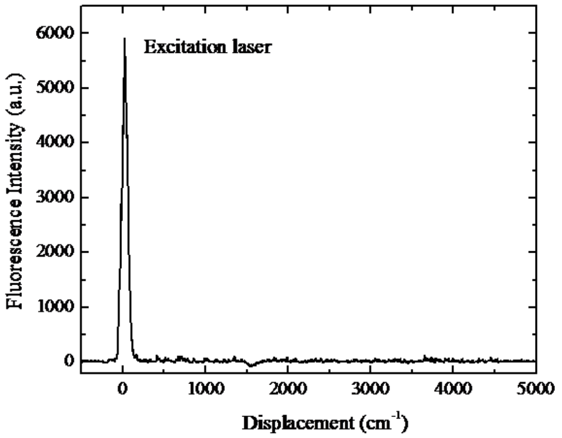

Figure 3.6. The DF spectrum from the band at 15619 cm^{-1}.

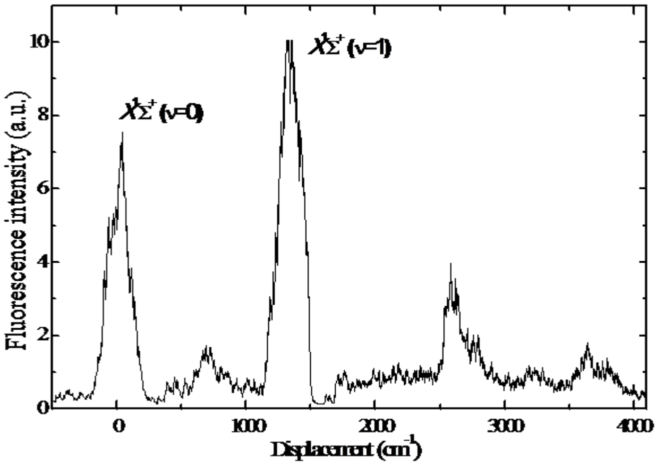

Figure 3.7. The DF spectrum from the band at 15623 cm^{-1}.

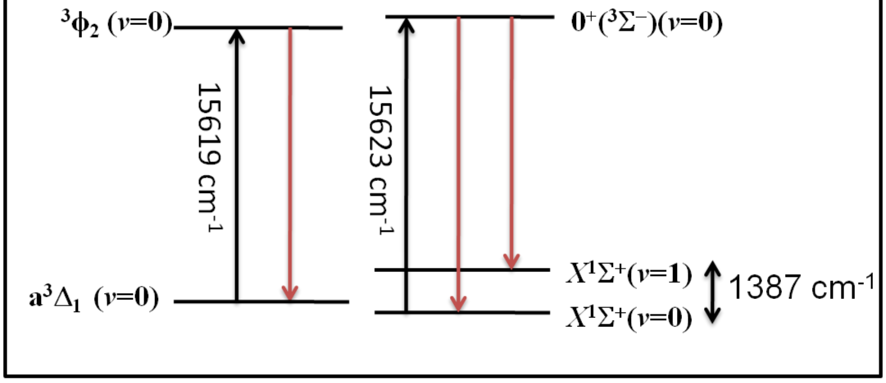

Figure 3.8. The experimental scheme for wavelength filtered-LIF technique.

The appearance of only single *P* and *R* branch structure in 15623 cm^{-1} band indicated that the transitions was of Δ*Ω* = 0 type. The first lines of *R*(0) and *P*(1) establish the *Ω* values as *Ω*″ = 0, *Ω*′ = 0. From the combination difference, the lower state confirmed as the ν = 0 of the ground state $X^1\Sigma^+$and thus the upper state involved in the transition was assigned *Ω* = 0^+. Also based on the observed weak intensity associated with the band and long radiative lifetime (see in Table 3.3), the upper state at 15623 cm^{-1} was assigned as the $0^+(^3\Sigma^-)$. The molecules with the Hund's case (c) tendencies, which could be more probable case for LaH molecules, the *Ω* assignment of 0^+ for this state is more likely than the $^3\Sigma^-$ parent term assignment. In addition to the appearance of few extra lines for 15623 cm^{-1} band, the upper state was found to be perturbed at *J* = 5 – 7 and are listed in Table A1 of Appendix A.

3.3.2.2 The $D^1\Pi$–$X^1\Sigma^+$ and $E^1\Pi$–$X^1\Sigma^+$ systems

The presence of *P*, *Q*, and *R* branch structure in 17398 and 17549 cm^{-1} bands shown in Fig.3.9 and 3.10 indicated that the observed transitions were of Δ*Ω* = ±1 type. As discussed earlier the combination difference indicated that the lower state involved in these transitions is ν = 0 of $X^1\Sigma^+$state. Also the observation of the first lines of *R*(0), *Q*(1) and *P*(2) establish the *Ω* values of upper state as *Ω*′ = 1. Thus the upper states of these transitions were assigned as *D*1, *E*1. Short radiative lifetime of 42 and 46 ns respectively for *D*1 and *E*1 bands and strong intensity associated with these bands indicated that the transitions occurred within same multiplicity and thus the most plausible parent term assignment of the *D*1 and *E*1 states was $^1\Pi$. The *Ω*-doubling splitting in the upper state particularly for *E*1 state was small. For the *D*1 state , it was found to be proportional to $J^{1.9}$ however for the *E*1 state it was very small up to $J \leq 6$ and was proportional to J^3 in the range *J* = 6–12 (see Fig.3.11a & b). The *Q*(10) to *Q*(12) lines were perturbed for the

17398 cm^{-1} band (see Table A2 of Appendix A), however the band at 17549 cm^{-1} showed visible perturbation at $Q(2)$, $Q(3)$, $Q(11)$ and $Q(12)$ (see Table A3). Also the 17549 cm^{-1} band showed a few extra lines which could not be grouped as members of the band and displayed longer radiative lifetime of 215 to 240 ns than that of 17549 cm^{-1} band (46 ns).

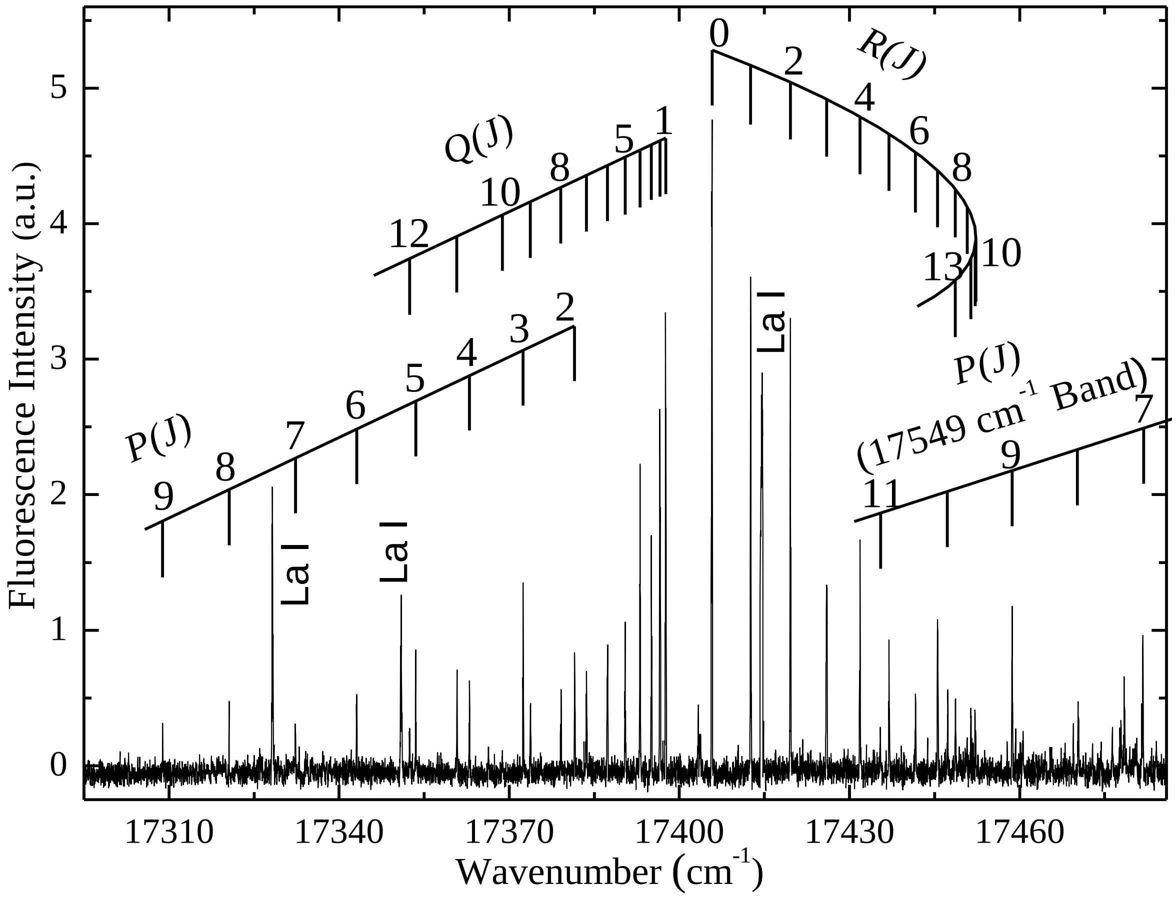

Figure 3.9. Rotational structure of (0, 0) $D^1\Pi$–$X^1\Sigma^+$ excitation band of jet-cooled LaH molecule at 17398 cm^{-1}.

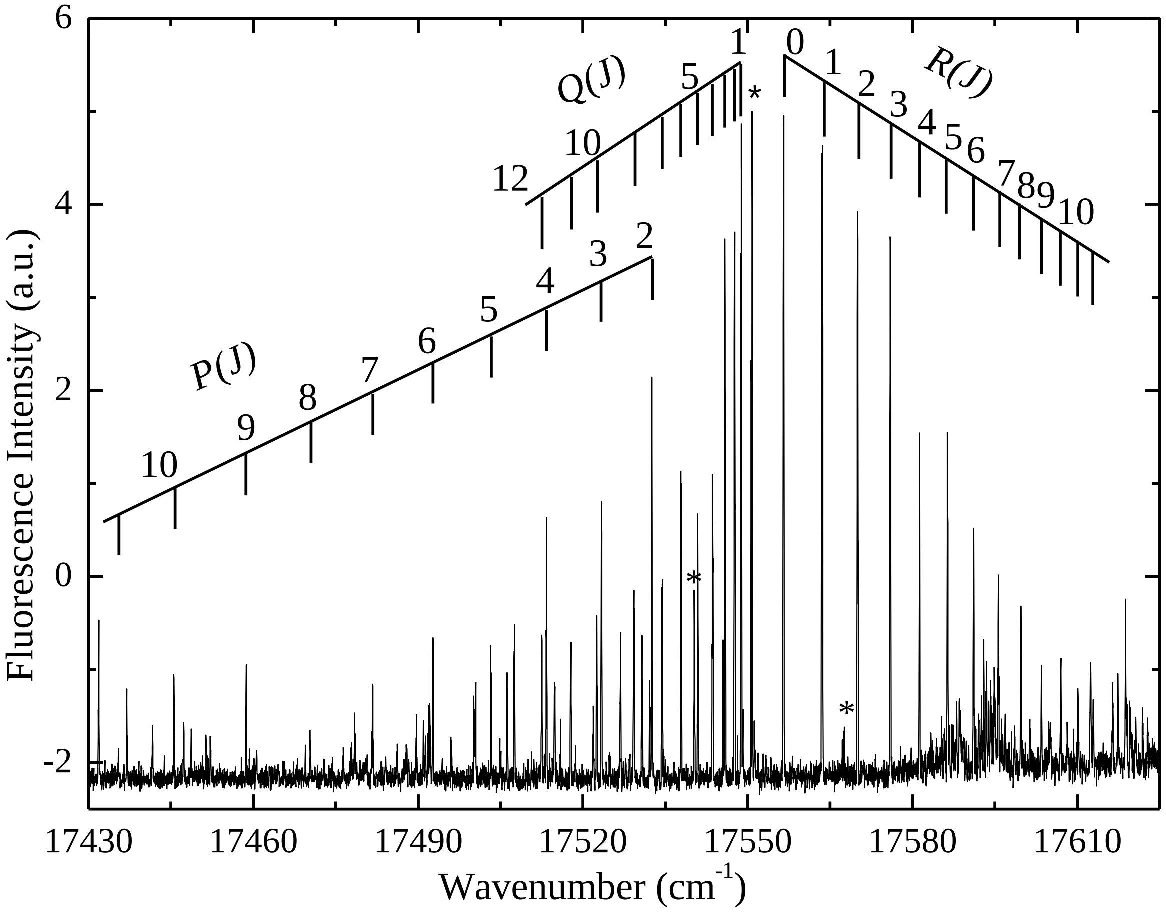

Figure 3.10. Rotational structure of the (0, 0) $E^1\Pi$–$X^1\Sigma^+$ excitation band of jet-cooled LaH molecule at 17549 cm^{-1}. Lanthanum atomic lines (La I) indicated by '*'.

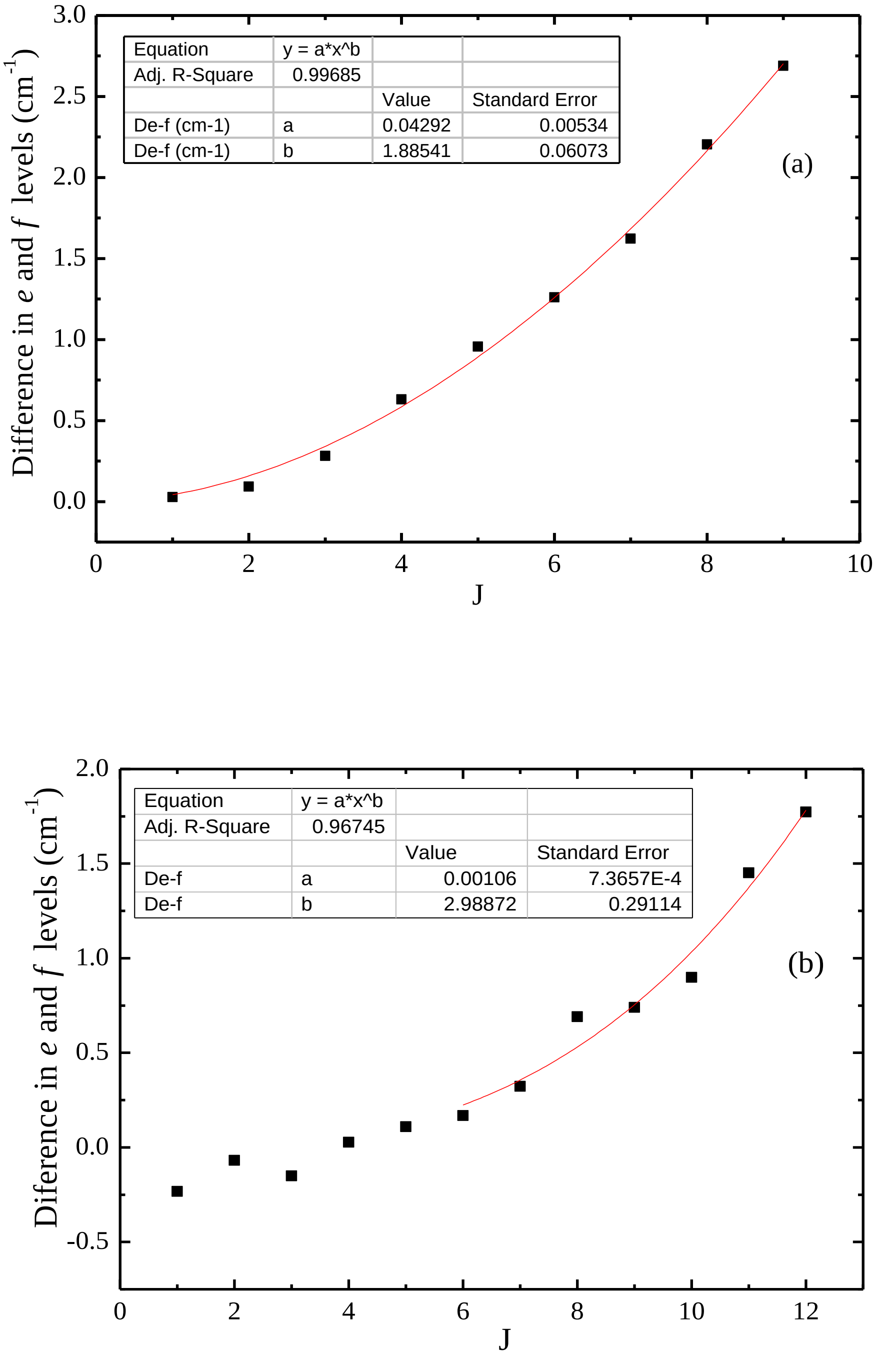

Equation	y = a*x^b		
Adj. R-Square	0.99685		
		Value	Standard Error
De-f (cm-1)	a	0.04292	0.00534
De-f (cm-1)	b	1.88541	0.06073

Equation	y = a*x^b		
Adj. R-Square	0.96745		
		Value	Standard Error
De-f	a	0.00106	7.3657E-4
De-f	b	2.98872	0.29114

Figure 3.11. The Ω-doubling splitting for the band (a) at 17398 cm^{-1} and (b) at 17549 cm^{-1}.

3.3.2.3 The $\Omega' = 0^{+}$–$\Omega'' = 1$ system

Similar to 18595 cm^{-1} band which was observed by Bernard and Bacis [83] and reassigned by Ram and Bernath [86] as (0,0) band of 0^{+}-$a\ {}^{3}\Delta_{1}$ system, the band at 18509 cm^{-1} showed single *P*, *Q* and *R* structure (see Fig. 3.12) indicating that it was $\Delta\Omega = \pm1$ transition. The *R*-branch of this band showed interference from (1,0) band of $B^{2}\Sigma^{+}$-$X^{2}\Sigma^{+}$ system of LaO and it could not be filtered because this band showed fluorescence only at the excitation laser wavelength. The appearance of LaO band was probably due to the presence of sufficient oxide layer on lanthanum metal rod or residual oxygen in gas line. The appearance of first lines, viz. *R*(1) and *P*(1) and confirmed that this was $\Omega' = 0$-$\Omega''=$ 1 transition, thus the obvious assignment of the band was thought to be (1,1) transition of 0^{+}-$a^{3}\Delta_{1}$ system. However, the combination differences for the lower state involved in this band did not concur with $\nu = 1$ state of $a^{3}\Delta_{1}$. Also the radiative lifetime of the upper state involved in this transition is distinctly different than that of the 0^{+} state (see Table 3.3). The lower state combination differences coincided within the experimental precision with those of the $\nu = 1$ of $a^{3}\Delta_{2,3}$ state, but the observed lower state showed large Ω-doubling splitting which was not present in the $a^{3}\Delta_{2,3}$ state [86]. In view of the above observations we could not assign the band observed at 18509 cm^{-1} to the transition connecting the earlier known low-energy excited electronic states.

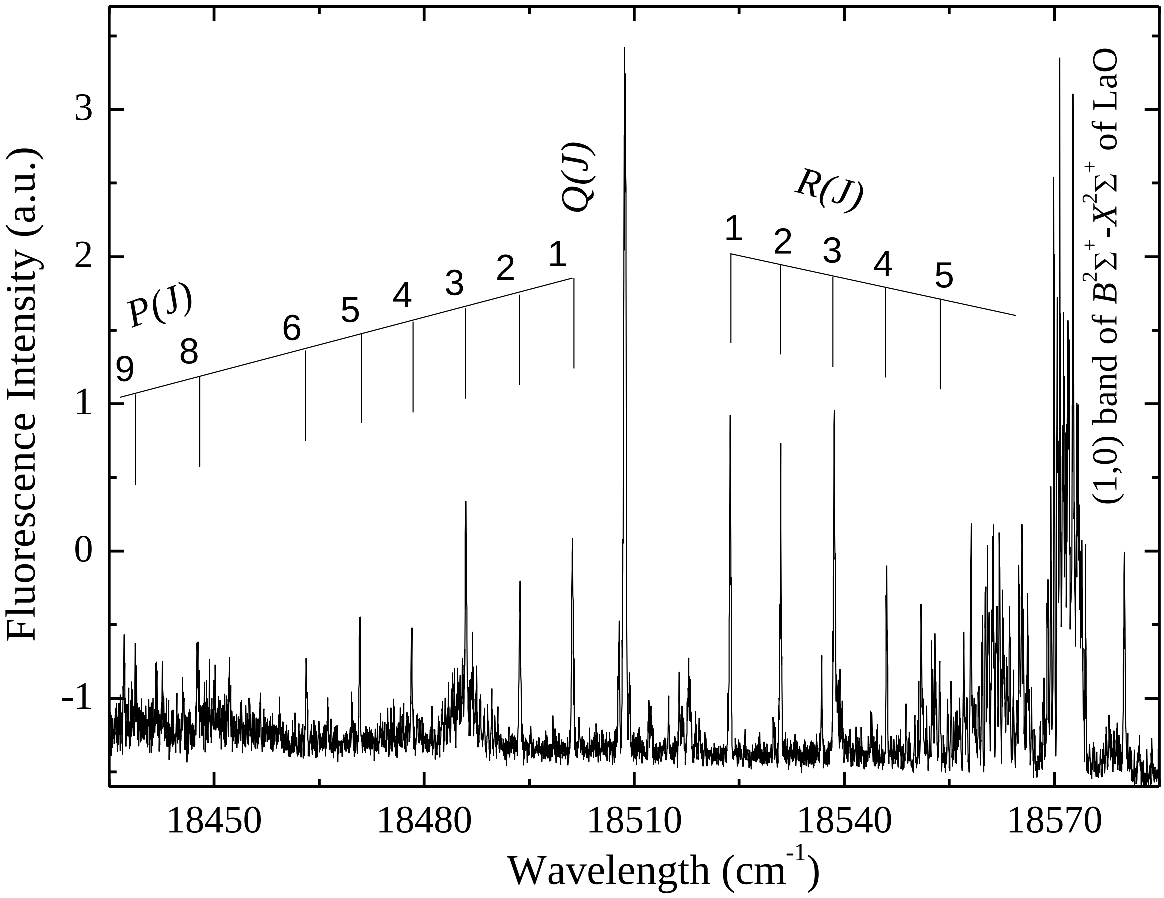

Figure 3.12. Rotational structure of the band of jet-cooled LaH molecule at 18509 cm^{-1}.

3.3.2.4 The [20.0]$\Omega = 1$–$X^1\Sigma^+$ system

The excitation bands at 20042 and 19972 cm^{-1} were observed to be very weak while the monochromator was parked at the excitation laser wavelength. However, the dispersed fluorescence spectra from these bands showed a strong fluorescence at 1660 cm^{-1} to the red from the excitation laser (see Fig. 4.2). This line was assigned as fluorescence to the $\nu = 0$ of $a^3\Delta_2$ state and is discussed in detail in the next chapter. By parking the monochromator at this position, we recorded both the rotational resolved excitation bands and are shown in Fig. 3.13. The presence of *P*, *Q*, and *R* branch structure in 20042 and 19972 cm^{-1} bands indicate that the transitions were of $\Delta\Omega = \pm1$ type. The first lines of *R*(0), *Q*(1) and *P*(2) establish the Ω values as $\Omega'' = 0$, $\Omega' = 1$. From the combination differences, the lower state of the bands at 20042 and 19972 cm^{-1} were respectively confirmed as $\nu = 0$ and $\nu = 1$ of the ground state, $X^1\Sigma^+$.Thus the upper states were assigned as $\nu = 0$ and $\nu = 1$ of $\Omega = 1$ state. The term energy of $\nu = 1$ of $\Omega = 1$ state was determined as 21359.1 cm^{-1} which was obtained by adding the rotationless term energy of $\nu = 1$ of $X^1\Sigma^+$ state to the band origin. The rotationless energy of 1387.1 cm^{-1} for $\nu = 1$ of $X^1\Sigma^+$ state was determined by DF studies discussed in chapter 4. Rotational perturbations were observed for the few lines in the 20042 cm^{-1} band. The Q (7) line showed irregular spacing and Q lines beyond $J = 14$ were untraceable due to interference from LaO band (see Fig. 3.13). These bands strongly interfered respectively due to (3,0) and (4,1) bands of $B^2\Sigma^+$-$X^2\Sigma^+$ system of LaO. The R lines beyond $J = 15$ could not be identified due to perturbations. The corresponding P lines viz. P(17) and P(18) were also perturbed and higher P lines were not traceable. This band also showed few extra lines belonging to LaH that could not be grouped as members of the band. As Ram and Bernath [86] did not report any perturbation in $\nu = 0$ and 1 vibrational levels of the ground state, it can be inferred that the upper state at 20042 cm^{-1} is perturbed. As the 19972 cm^{-1} band is a hot band, the rotational lines only up to R(5), P(9) and Q(9) were observed. No rotational perturbations were observed for this band. The DF spectrum from the 20042 cm^{-1} state showed transitions mainly to the triplet states (see in Chapter 4). This indicates that this state probably has triplet multiplicity. The appearance of strong Q-branch in the spectra as well strong fluorescence to $a^3\Delta_2$ state suggests the $^3\Pi$ rather than $^3\Sigma^-$ to be the parent term of this state. However, the short radiative lifetime of ~20 ns (Table 3.3) of this state contradicts with the triplet character. This probably indicates that $\Omega = 1$ assignment in Hund's case (c), usual for heavy molecules, is more appropriate for this state. Thus for this state the nomenclature introduced by Linton *et al.* [54] was followed and indicated as [20.0]$\Omega = 1$ for $\nu = 0$ and [21.3]$\Omega = 1$ for $\nu = 1$ states.

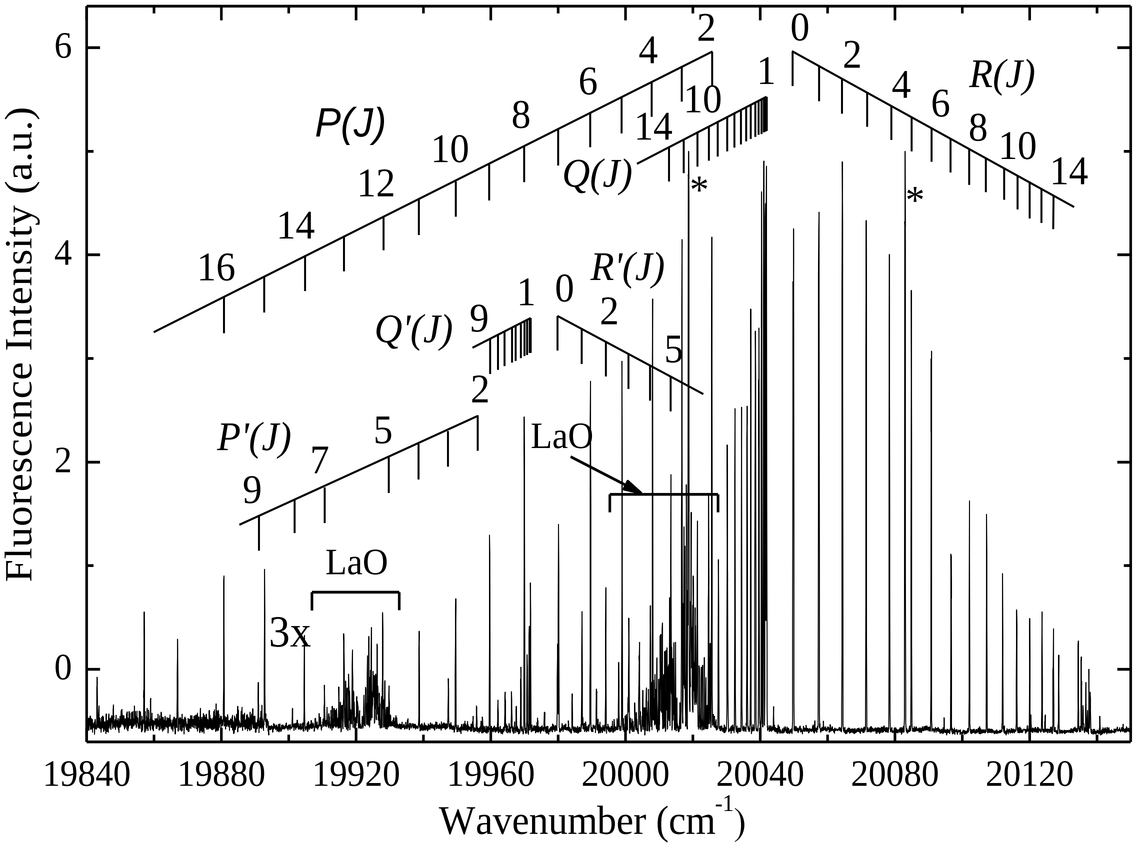

Figure 3.13. Rotational structure of the (0, 0) and (1, 1) [20.0]Ω = 1–$X^1\Sigma^+$ excitation bands of jet-cooled LaH molecule. Lanthanum atomic lines (La I) indicated by '*'.

3.3.2.5 The [21.9]Ω= 0^+- $X^1\Sigma^+$ and [22.1]Ω= 0^+- $X^1\Sigma^+$ systems

Two other simple band systems with origin at 21970 and 22100 cm^{-1} were observed to be weak in intensity while the monochromator was parked at the excitation laser wavelength. However, the dispersed fluorescence spectra from both the bands showed a strong fluorescence at 5066 displacement wavenumber. By parking the monochromator at this strong fluorescence position, rotationally resolved excitation bands were recorded. The rotational structure of the 21970 and 22100 cm^{-1} bands, displayed in Fig.3.14, showed a single *P*- and a single *R*-branch, indicating $\Delta\Omega = 0$ transitions. Fig. 3.14 also shows the simulated spectrum by Pgopher programme used for assignment and determination of molecular constants, discussed in next section. The rotational quantum number assignments for the *P*- and *R*-branches in both these bands were straight forward. The first lines of *R*(0) and *P*(1) established the *Ω* values as $\Omega'' = 0, \Omega' = 0$. From the combination differences, the lower state was confirmed as the ν = 0 of the ground state, $X^1\Sigma^+$ and thus the upper state involved in the transition was assigned as $\Omega = 0^+$. The DF spectrum recorded from isolated rotational lines of both the bands showed transitions to mainly the triplet states. The transitions to the low-lying triplet states indicate that both

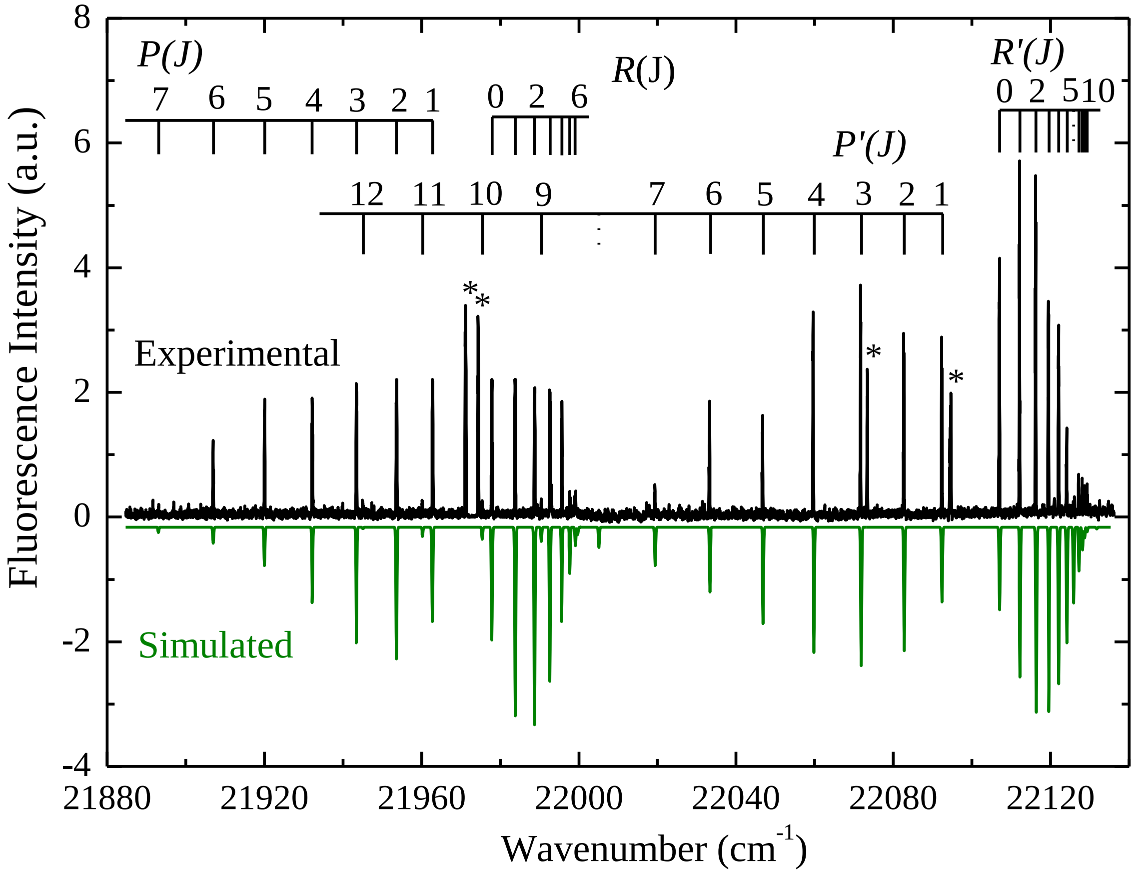

Figure 3.14. Rotational structure of the excitation bands of jet-cooled LaH molecule at 21970 and 22100 cm^{-1}. Inverted spectrum is simulated from Pgopher programme discussed in next section. Lanthanum atomic lines (La I) indicated by ‘*’.

the states have triplet multiplicity. However, the short radiative lifetime of ~40 ns of these states (Table 3.3) contradicts the triplet character. This again indicates that Ω = 0^+ assignments in Hund's case (c), usual for heavy molecules, are more appropriate for these states. Thus for these states the nomenclature introduced by Linton *et al.* [54] was followed and indicated as [21.9]$\Omega = 0^+$ and [22.1]$\Omega = 0^+$ states.

3.3.3 Molecular constants

The transition wavenumbers observed in the laser excitation spectra were reduced to the set on molecular constants using a nonlinear least squares fitting procedure. The spectra are also fitted and simulated using Pgopher program [106].

The $X^1\Sigma^+$ and 0^+ states were described by customary energy level expression of the form,

$$F_v(J) = T_v + B_v J(J+1) - D_v[J(J+1)]^2 + H_v[J(J+1)]^3 \tag{3.3}$$

and the states with $\Omega = 1$ were described by the expression,

$$F_v(J)\binom{e}{f} = T_v + B_v J(J+1) - D_v[J(J+1)]^2 \pm \tfrac{1}{2}\left\{q_v J(J+1) + q_{D_v}[J(J+1)]^2\right\} \tag{3.4}$$

where B_v ,D_v and H_v are the rotational constant and its higher-order corrections and q_v and q_{Dv} are the Ω-doubling constant and its higher order corrections. Each rotational line was given an appropriate weight depending on the signal-to-noise ratio and the extent of blending. The molecular constants for the $v = 0,1$ level of the $X^1\Sigma^+$ ground state were constrained in the fit at more precise values obtained by Ram and Bernath [86] from the analysis of the near-infrared data on $A^1\Pi$–$X^1\Sigma^+$ bands and the molecular constants for the $0^+(^3\Sigma^-)$, $D^1\Pi$, $E^1\Pi$, [20.0]$\Omega = 1$ ($v = 0$ and 1), [21.9]$\Omega = 0^+$ and [22.1]$\Omega = 0^+$ states were treated as adjustable parameters. The obviously perturbed lines were removed from the fit. The molecular constants obtained for the $0^+(^3\Sigma^-)$, $D1$, $E1$, [20.0]$\Omega = 1$, [21.9]$\Omega = 0^+$

and [22.1]$\Omega = 0^+$ states are given in Table 3.4. Table 3.5 list the molecular constants for the upper and the lower electronic excited states associated with the 18509 cm^{-1} band.

As seen from the Table 3.4, the perturbations in the 17549 cm^{-1} band were reflected in the relatively poor variance of the least squares fit, even after removing a few visibly perturbed lines (see in Table A3). The poor variance in the least squares fit for the 17549 cm^{-1} band was also reflected in the relatively large standard deviation for the determined molecular constants. However, the exact identity of the perturbing states could not be established due to the lack of sufficient data. The obviously perturbed lines in the 20042 cm^{-1} band were also not considered in the fit. The term energy of the excited state was determined as 21359.1 (5) cm^{-1} by adding the energy of $\nu = 1$ level of the $X^1\Sigma^+$ state to the band origin of the 19972 cm^{-1} band. The rotational constant for the 21359.1 cm^{-1} state is just smaller by ~2% to that of 20042 cm^{-1} state and both the excited states have similar radiative lifetimes (see Table 3.3).This further support that the 21359.1 cm^{-1} state is $\nu = 1$ of the 20042 cm^{-1} state. The $\Delta G_{1/2}$ value for this excited state is 1317.1 cm^{-1}.

Table 3.4. Molecular constants (in cm^{-1}) of the $X^1\Sigma^+$ ground state and 0^+ ($^3\Sigma^-$), $D^1\Pi$, $E^1\Pi$, [20.0]Ω = 1, [21.9]Ω = 0^+ and [22.1]Ω = 0^+ excited states.

Constants	**$X\ ^1\Sigma^{+\,a}$**		**$0^+(^3\Sigma^-)$**	**$D^1\Pi$**	**$E^1\Pi$**	**[20.0]Ω = 1**		**[21.9]Ω =0^+**	**[22.1]Ω =0^+**
	(ν = 0)	**(ν = 1)**	**(ν = 0)**	**(ν = 0)**	**(ν = 0)**	**(ν = 0)**	**(ν = 1)**	**(ν = 0)**	**(ν = 0)**
T_v	0.0	1387.1(5)^b	15622.86(3)	17397.94(2)	17549.05(5)	20041.96(1)	21359.1(5)	21970.71(2)	22100.31(4)
B_v	4.041837(62)^c	3.964443(78)	3.7369(79)	3.82270(64)	3.76697(227)	3.93916(28)	3.8468(15)	3.5070(20)	3.2902(49)
$D_v\times10^4$	1.3387(21)	1.3339(23)	19.4(37)	5.39(4)	–2.15(18)	2.154(15)	2.38(18)	–4.46(37)	–51.8(18)
$H_v\times10^5$	0.000312(21)	-	-	-	-	-	-	-	–3.75(21)
$L_v\times10^7$	-	-	-	-	-	-	-	-	1.11(8)
$q_v\times10^2$	-	-	-	2.86(5)	0.737(86)	–5.845(42)	–3.5(1)	-	-
$q_{Dv}\times10^5$	-	-	-	-	-	7.10(24)	-	-	-
Variance of fit in cm^{-1} (No. of lines)	-	-	0.2(9)	0.36(30)	1.64(30)	0.14(43)	0.21(22)	0.03(13)	0.06(21)

[a] Molecular constants (from Ref [86]) constrained in the fit.
[b] Determined from DF study discussed in Chapter 4.
[c] Number in parentheses denote one standard deviation in the last quoted digits.

Table 3.5. Molecular constants (in cm^{-1}) for the upper and the lower electronic excited states associated with the 18509 cm^{-1} band.

Constants	Lower state	Upper state
T_v	a	a +18508.79(5)
Bv	3.760(4)[b]	3.717(9)
$D_v \times 10^3$	-	2.0(3)
$H_v \times 10^5$	-	2.4(3)
$q_v \times 10^2$	1.5(6)	-

[a] Value undermined.
[b] Numbers in parentheses denote one standard deviation in the last quoted digits.

3.4 Discussion

Das and Balasubramanian [85] have predicted the ground state of LaH was arising from $1\sigma^2 2\sigma^2$ electron configuration, similar to YH molecule [63]. They inferred that in the $^1\Sigma^+$ ground state, the 1σ orbital is a strongly bonding orbital made of La(6s) and H(1s) and the participation of H(1s) orbital in the 2σ orbital is very small. The 2σ orbital is predominantly a non-bonding hybrid of La(6s), La($6p_z$), and La($5d_\sigma$) but slightly antibonding with respect to H(1s). Mulliken populations of ground and various excited electronic state of LaH show that the gross La population of all the states is smaller than 3.0 indicating considerable electron transfers from La to H and hence the LaH bond has La^+H^- polarity. Also the La(6p) population is considerable in ground as well as excited states. This indicates considerable *dsp* hybridization in the formation of bond. In this present work, we have observed six new excited electronic states, $0^+(^3\Sigma^-)$, $D^1\Pi$, $E^1\Pi$, $[20.0]\Omega = 1$, $[21.9]\Omega = 0^+$ and $[22.1]\Omega = 0^+$ respectively at 15622.9(1), 17397.9(1), 17549.0(1), 20041.96(1), 21970.71(2) and 22100.31(4) cm^{-1}. All these states were observed in $v = 0$ level, in addition $[20.0]\Omega = 1$ state was also observed in $v = 1$ level at

21359.1 cm^{-1}. A schematic energy level diagram of the electronic states of LaH with transitions observed in the present work, by solid lines and earlier work, by dashed lines is shown in Fig.3.15. The energy of $a^3\Delta$ state is not known and is placed at 2805 cm^{-1} in Fig 3.15 as predicted by Balasubramanian [85]. In order to better understand the nature of these newly observed excited states we attempted to compare our results with *ab initio* calculations of Das and Balasubramanian [85] and Koseki *et al.* [91]. The comparison of experimental term values and internuclear distances for electronic states reported in this and earlier work [86,90] with *ab initio* values is shown in Table 3.6. As seen from the Table 3.6, the *ab initio* results overestimated the internuclear distances a little and term energies by substantial amount. The *ab initio* equilibrium internuclear distances r_e for the

Table 3.6. Comparison of experimental values with available *ab initio* calculations in LaH.

Electronic state	**Experimental values**^{a}		***Ab initio* results**			
	T_0(cm^{-1})	**$r_0[r_e]$(Å)**	**T_0(cm^{-1})^b**	**r_e(Å)^b**	**T_0(cm^{-1})^c**	**r_e(Å)^c**
$X\ ^1\Sigma^+$	0.0	[2.031969(20)]^d	0.0	2.08	0.0	2.060
$A^1\Pi$	4533.55933(80)	[2.074276(21)]^d	6200	2.13	6354	-
$C^1\Sigma^+$	10150.944(6)	2.152983(71)^e	12923	2.20	11323	-
$0^+(^3\Sigma^-)$	15622.86(3)	2.1233(23)	16016	2.17	-	-
$D^1\Pi$	17397.94 (2)	2.09938(17)	-	-	18033	-
$E^1\Pi$	17549.05(5)	2.11485(64)	20124	2.19	-	-
[20.0]$\Omega = 1$	20041.96(1)	2.06811(7)	-	-	-	-
[21.9]$\Omega = 0^+$	21970.71(2)	2.19199(47)	-	-	-	-
[22.1]$\Omega = 0^+$	22100.31(4)	2.2630(15)	-	-	-	-

[a] Present work
[b] Ref.[85], $\omega_e x_e$ disregarded while calculating T_0 from T_e
[c] Ref.[91]
[d] Ref.[86]
[e] Ref.[90]

ground $X^1\Sigma^+$, $A^1\Sigma^+$ and $C^1\Sigma^+$ states reported in [85] are higher by about 2.4 to 2.7% than the experimental values, however r_e calculated for $X^1\Sigma^+$ state by Koseki *et al.*[91] is overestimated by 1.4%. The *ab initio* electronic transition energies for the $A^1\Pi$ and $C^1\Sigma^+$ states from ground state, $X^1\Sigma^+$ are higher respectively by about 36% and 27% than observed values in [85], however the transition energy for *A*-*X* transition is overestimated by 40% and only by 12% for *C*-*X* transition than experimental values by Koseki *et al.* [91]. The observed state at T_0 = 15622.9 cm^{-1} in the present work having $\Omega = 0^+$ correlate with $^3\Sigma^-$ parent term assignment in case (b). Das and Balasubarmanian [85] have predicted two $^3\Sigma^-$ states at energy 12035 and 16107 cm^{-1}. Considering the trend that the term energies are overestimated by *ab initio* calculations, the observed $0^+(^3\Sigma^-)$ state may correspond to a state at 16107 cm^{-1} which is heavily mixed. It shows major contribution of 60 % from $1\sigma^2 1\delta^2$, 4% from $1\sigma^2 1\pi 2\pi$ and $1\sigma^2 2\pi 3\pi$ and about 3% from $1\sigma^2 1\pi^2$, $1\sigma^2 1\delta 2\delta$ configurations [85]. The internuclear distance r_0 determined from this study for $0^+(^3\Sigma^-)$ state is 2.1233 (23) Å. The corresponding *ab initio* value [85] is overestimated by 2.2 % than the experimental value. The $d0^+(^3\Sigma^-)$ state was also observed in isovalent molecule YH by Ram and Bernath [87] and Jakubek *et al.* [101] in $\nu = 0$ with perturbation from $\nu = 1$ of $C^1\Sigma^+$. The $\nu = 0$ of $d0^+(^3\Sigma^-)$ state is at 15756 cm^{-1} and $\nu = 1$ of $C^1\Sigma^+$ is at 15502 cm^{-1} state are energetically closer and showed the perturbation in YH molecule. However, this is not the case in LaH molecule, the $\nu = 0$ of $0^+(^3\Sigma^-)$ state is at 15623 cm^{-1} and $\nu = 1$ of $C^1\Sigma^+$ is at 11381 cm^{-1} (determined using predicted ω_e value) which shows that no overlap between these two electronic states. But the indication of perturbation at J = 5-7 in the least squares term value fitting, appearance of few extra lines and large value of the centrifugal distortion constant D shows perturbations in the $0^+(^3\Sigma^-)$ state. However, the perturbing state could not be exclusively identified due to insufficient data. The $^3\Sigma^-$ state is predicted also for isovalent ScH by Anglada *et al.* [107] but has not been observed so far.

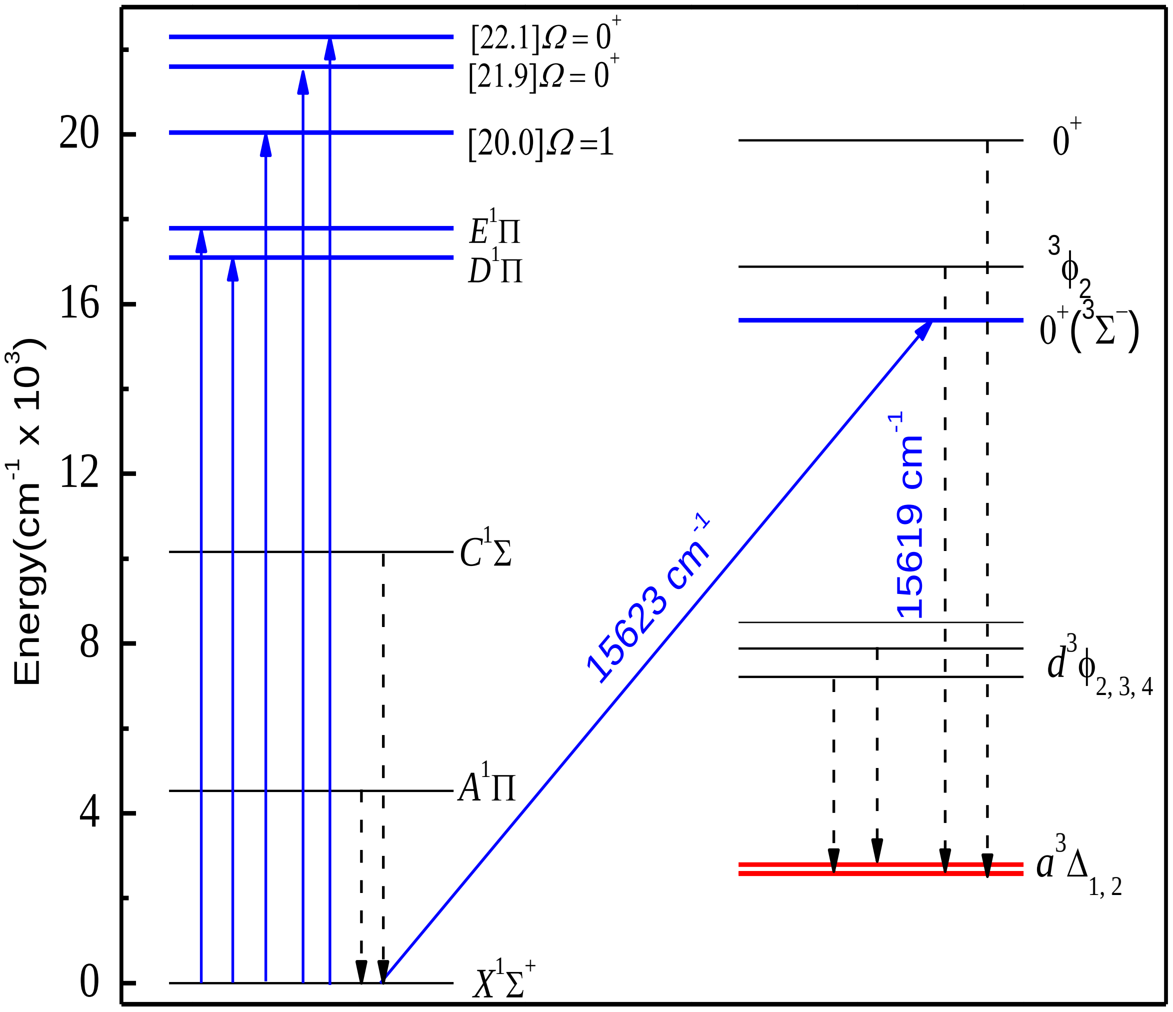

Figure 3.15. A schematic diagram of the electronic states of LaH. The solid (blue) and dashed arrows (black) indicate transitions observed respectively in the present and the earlier work. Prior to present work the experimental value energy of $^3\Delta$ states (indicated in red) with reference to ground states was not known.

The plausible assignment for the *D*1 and *E*1 electronic excited states observed respectively at T_0 = 17397.9 and 17549.0 cm^{-1} is $^1\Pi$. Das and Balasubramanian [85] have predicted $B^1\Pi$ and $C^1\Pi$ states respectively at T_e = 15729 and 20170 cm^{-1}. Koseki *et al.* [91] also predicted intense electronic transitions between the ground $X^1\Sigma^+$ and $D^1\Pi$ and $I^1\Pi$, with transition dipole moment larger than *A*-*X* and *C*-*X* transitions, respectively at 15396 and 18033 cm^{-1}. However, neither of these studies predicted two close lying $^1\Pi$ states separated by just 150 cm^{-1} as observed in the present work. Thus as shown in Table 3.6, either of the observed *D*1 or *E*1 states may correspond to $^1\Pi$ state predicted by Koseki [91] and Balasubramanian [85] respectively at 18033 and 20170 cm^{-1}. The overestimation of the excited electronic states term values by *ab initio* calculations [85,91] compared to the values observed in the present as well as in the earlier work [83,86,90] may be caused by the underestimation of the electron correlation effects taken into account at the level of theory. The visible perturbations at several places in the *E*1 state and appearance few extra lines with distinct long radiative lifetimes compared to the members of 17549 cm^{-1} band, indicate the presence of electronic state, probably with triplet multiplicity interacting with *E*1 state. As mentioned previously the perturbations in the *E*1 state are also reflected in poor variance in the least squares fit of the band and also the negative sign of centrifugal distortion constant *D*. We speculate that the perturbing state could be $^3\Pi$ state. Das and Balasubramanian [85] predicted a $^3\Pi$ state at 15880 cm^{-1}. Jakubek *et al.*[101,102] also reported the case of interacting $D^1\Pi$ (19573 cm^{-1}) and $f^3\Pi_2$ (19574 cm^{-1}) state in YH and YD which exhibit *J*-dependent variation in lifetime and effective Ω quantum number, determined from the Stark spectroscopy. However, we did not observe *J*-dependent variation in radiative lifetime for *E*1 state. The internuclear distance r_0 determined from this study respectively for *D*1 and *E*1 state are 2.09938(17) and 2.11485(64) Å. The corresponding *ab initio* values [85] for $D^1\Pi$ and $E^1\Pi$ are higher by 2 to 4% than the experimental values. In addition, we observed three new excited electronic states [20.0]Ω = 1, [21.9]$\Omega = 0^+$ and [22.1]$\Omega = 0^+$ respectively at 20041.96(1), 21970.71(2) and 22100.31(4) cm^{-1}. These are probably described well by case(c) notations. Present available *ab initio* calculations did not calculate electronic states with $\Omega = 1$, and $\Omega = 0^+$ in this energy range.

In summary, the *ab initio* values [85,91] for term energies are largely and internuclear distances are slightly overestimated as compared to the experimental values determined in previous [86,90] and present work. There is a need to extend the *ab initio* calculations to higher energy excited states for comparing the observation of additionally observed electronic states.

3.5 Conclusions

Laser-induced fluorescence excitation spectra of jet-cooled LaH molecules confirmed $^1\Sigma^+$ symmetry for the ground state, as previously suggested by Ram and Bernath [86]. Six new electronic states, viz. $0^+(^3\Sigma^-)$, $D^1\Pi$, $E^1\Pi$, $[20.0]\Omega = 1$, $[21.9]\Omega = 0^+$ and $[22.1]\Omega = 0^+$ have been observed at 15622.9(1), 17397.9(1), 17549.0(1), 20041.96(1), 21970.71(2) and 22100.31(4) cm^{-1} respectively. The internuclear distances r_0 were found to be 2.1233(23), 2.09938(17), 2.11485(64), 2.06811(7), 2.19199(47) and 2.2630(15) Å respectively for the $0^+(^3\Sigma^-)$, $D^1\Pi$, $E^1\Pi$, $[20.0]\Omega = 1$, $[21.9]\Omega = 0^+$ and $[22.1]\Omega = 0^+$states. The 0^+ state may correspond to parent term $^3\Sigma^-$ in case (b) and $D1$, and $E1$ states to $^1\Pi$. The $[20.0]\Omega = 1$, $[21.9]\Omega = 0^+$ and $[22.1]\Omega = 0^+$ could not assign the parent terms and follows the assignment in Hund’s case(c), usual for heavy molecules, is more appropriate for these states. The 15623 cm^{-1} band is the intercombination transition observed for the first time in LaH. The present data on the new excited states is compared with the available *ab initio* results [85,91] and in general the overestimation of calculated internuclear distances and term energies have been observed.

Chapter 4

Wavelength resolved laser-induced fluorescence spectroscopy of jet-cooled LaH molecule

4.1 Introduction

This chapter presents the wavelength-resolved fluorescence (WRF) or dispersed fluorescence (DF) study of LaH molecule. The principal motivation behind this study is to establish the missing energy linkage between singlet and triplet manifold, obtain information about low-energy excited states predicted by *ab initio* studies and also to determine the vibrational frequencies of the ground state of LaH molecule. In the absence of observation of inter-combination transition, the singlet and triplet stack of electronic states observed by earlier workers [83,86] were not placed energetically with respect to each other. This chapter provides the Dispersed Fluorescence (DF) study of LaH molecules by exciting single isolated rotational levels of excited electronic states reported in chapter 3.

In chapter 3, we confirmed the $^1\Sigma^+$ symmetry of the LaH ground state arising from $1\sigma^2 2\sigma^2$ electronic configuration as previously suggested by *ab initio* studies [85]. A number of low-lying electronic states were predicted from *ab initio* studies [85]. The low-energy excited states $^{1,3}\Delta$ and $^{1,3}\Pi$ arise respectively from the excitation of 2σ electron from the ground state configuration to 1δ and 1π orbital to get $1\sigma^2 2\sigma 1\delta$, $1\sigma^2 2\sigma 1\pi$ electron configurations. All these states are also expected in isovalent ScH and YH molecules. Ram and Bernath [99,100] have observed low-energy excited states for ScH at 4185, 5404 cm^{-1} and assigned them as the $A^1\Delta$, $B^1\Pi$ respectively. Similarly in case of YH

[101,103], the low-energy excited states were observed at 6205, 6338, 6562, 9848, 9859 cm^{-1} and were respectively assigned as the $a^3\Delta_{1,2,3}$, $A^1\Delta$, $B^1\Pi$ states. However in LaH, out of the predicted low-energy excited states [85] Ram and Bernath [86] experimentally observed $A^1\Pi$-$X^1\Sigma^+$ transition at 4533 cm^{-1} and also observed transitions from $a^3\Delta$ states to $^3\Phi$ states. The other low-energy excited states $^1\Delta$ and $^3\Pi$ remained unobserved. In addition, important singlet-triplet manifold energy linkage is still not established. The vibrational frequencies for the ground and the earlier observed low-lying electronic states are also not experimentally known. Of late, we also got curious on whether LaH could be a potential candidate for electron electric dipole moment (eEDM) measurement. One of the criteria for LaH to be used for eEDM measurement is that it should have a low-lying $^3\Delta$ metastable state [108].

As discussed in chapter 3, Bacis *et al.* [83] first recorded the electronic spectra in the 450-660 nm range. These bands were classified [83] as $^3\Phi$–$^3\Delta$, $^1\Delta$–$^1\Pi$ and $^1\Sigma$–$^1\Pi$. Based on the available *ab initio* calculations for isovalent ScH [57,83], Bernard and Bacis [83] suggested $^3\Delta$ as the ground state. Later, high-level *ab initio* studies of Das and Balasubramanian [85] predicted a $^1\Sigma$ as the ground state with a low-lying $^3\Delta$ as the first excited state. Ram and Bernath [86] studied $A^1\Pi$–$X^1\Sigma^+$ and $d^3\Phi$–$a^3\Delta$ systems in the infrared and reassigned the $^1\Delta$–$^1\Pi$ and $^1\Sigma$–$^1\Pi$ transitions observed by Bernard and Bacis [83] as $^3\Phi_2$–$a^3\Delta_1$, and 0^+–$a^3\Delta_1$ respectively. Since no inter-combination line was observed, Ram and Bernath could not establish the singlet-triplet interval between the $X^1\Sigma^+$ and $a^3\Delta$ states.

This chapter describes determination of the term energies of Ω = 1 and 2 components of $a^3\Delta$ state, which established singlet-triplet energy linkage for this molecule. This observation allowed us to energetically place all states of triplet multiplicity, observed in this and earlier work [83,86] with respect to the ground state. In addition, all the spin-orbit components viz. $\Omega = 0^+, 0^-$, 1 and 2 of the $b^3\Pi$ state and also $B^1\Delta_2$ state, predicted by *ab initio* studies [85], are also observed for the first time. The vibrational frequency is an important spectroscopic quantity and is a finger print of the molecules. The vibrational frequency of LaH molecules in gas phase was not known prior to this work because of the lack of observation of off-diagonal transitions in *A*-*X* band [86]. The harmonic and anharmonic vibrational constant for the $X^1\Sigma^+$ and $a^3\Delta_2$ states and $\Delta G_{1/2}$ for the $a^3\Delta_1$ and $b^3\Pi_1$ states are also determined in this work. The vibrational constants determined in this work enabled us to determine $\Delta G_{1/2}$ for the $A^1\Pi$ and $d^3\phi_2$ states previously reported by Ram and Bernath [86].

4.2 Experiment

The LaH molecules are produced in a pulsed supersonic free-jet apparatus. The experimental procedure is essentially the same as described in Chapter 3. In this Chapter, dispersed fluorescence (DF) technique is used to map the vibrational frequencies of the ground state and search for low-lying electronic states. The DF spectra are obtained by exciting single isolated rotational levels of excited electronic states reported in chapter 3. For this purpose the pulsed dye laser is tuned to a particular ro-vibronic transition and the laser-induced dispersed fluorescence signal is recorded through a scanning monochromator in the blue and red side of the excitation wavelength. The spectral resolution of the DF measurement depends on the width of the spectral features in the scan. This is determined by the monochromator slit width. The reduction in slit width increases the spectral resolution; however it decreases the intensity of fluorescence line. One has to optimize these parameters to rotationally resolve the DF line with measurable fluorescence intensity. Typical spectral line widths, FWHM were of the order of 15 cm^{-1} in the DF spectra.

4.3 Observations and Analysis

The DF spectra of only one isotopomer^{139}La^{1}H were studied since lanthanum atom has a single naturally occurring major isotope La-139 (99.91%) and naturally abundant ammonia was used in the present experiment. The spectra were recorded in the 450-900 nm wavelength range. The DF spectra were first recorded with a moderate resolution (FWHM~50 cm^{-1}) to get coarse information about low-energy electronic states and their likely vibrations. The coarse spectra were then examined under relatively higher spectral resolution (FWHM~15 cm^{-1}) to resolve the rotational structure, wherever possible, so as to confirm the identity of the observed states.

4.3.1 Vibrational constants of the $X\,^1\Sigma^+$ ground state

The DF spectrum at moderate resolution originating from $0^+(^3\Sigma^-)$ state is shown in Fig.4.1(a). The same DF spectrum was recorded at relatively higher resolution, and is shown in Fig. 4.1(b).

The DF lines at displacement wavenumber 0, 1387.1 and 2742 cm^{-1} from excitation laser line consisted of *PR*-doublets when either *P*- or *R*-lines of the excitation band were excited. Since the upper state has $\Omega = 0$ and the transitions are typical to $\Delta\Omega = 0$, the lower levels were confirmed as the vibrations of the ground electronic state ν = 0-2. To determine the rotationless energy, T_v and rotational constants of ν = 0-2 levels, the DF spectra were recorded by exciting different $P(J)$ or $R(J)$-lines with J = 0-5. Rovibrational term values of the lower states were determined by subtracting the wavenumbers of the DF lines from the term energy of the rotational levels of the upper electronic states. The ro-vibrational term values, E_{Jv}, were fitted to the following expression (4.1) for determining the rotationless term value T_v, the rotational constant B_v and centrifugal distortion constants D_v of the vibrational level ν.

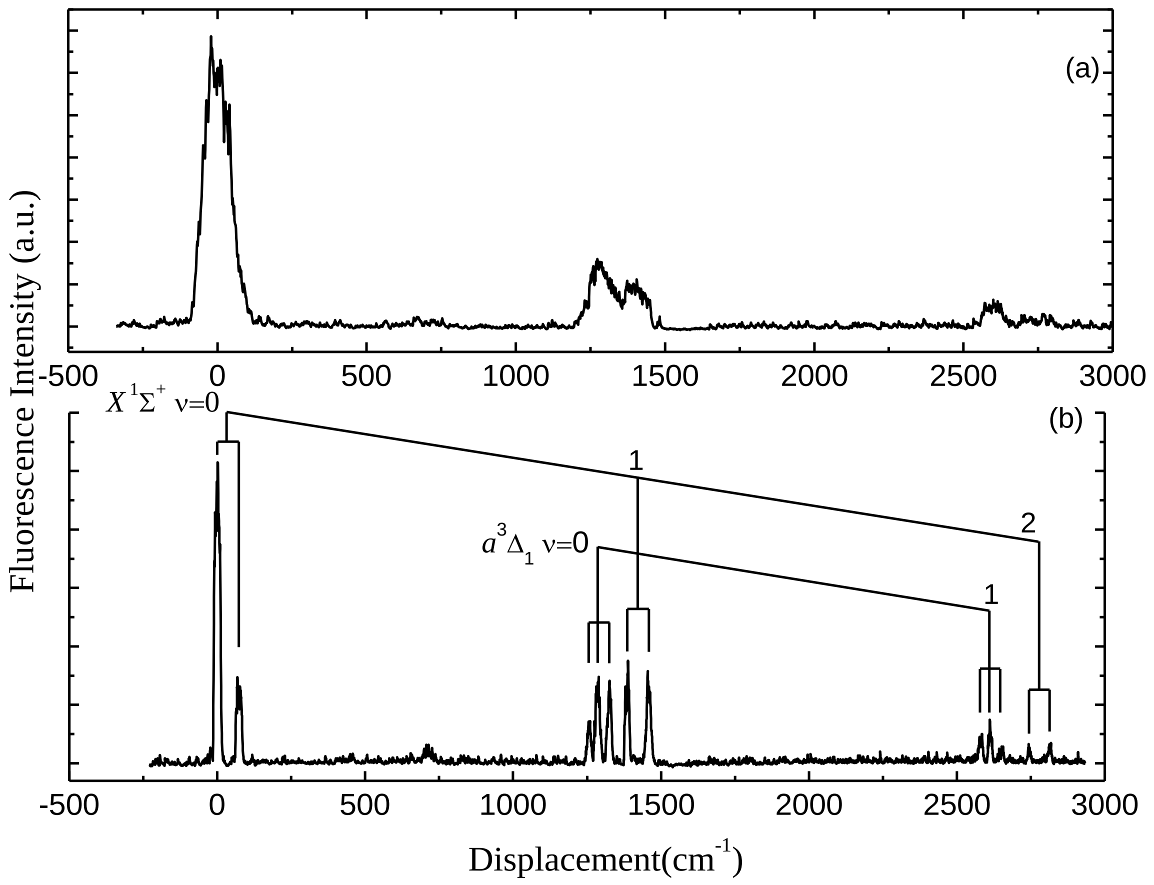

Figure 4.1. Laser-induced dispersed fluorescence spectra of LaH observed by exciting *R*(3)-line of the (0, 0) band of $0^+(^3\Sigma^-)$-$X^1\Sigma^+$ in (a) moderate resolution (b) high-resolution. The x-axis shows the displacement from the excitation line in cm^{-1}.

$$E_{Jv} = T_v + B_v J(J+1) - D_v[J(J+1)]^2 \tag{4.1}$$

The B_v determined from the DF data was compared with more accurate values reported in Ref.[86] and it was found that our B_v values were accurate only to first decimal place and no meaningful values for D_v could be determined. This is because the dispersed fluorescence data is less precise due to limited resolution of the monochromator. So in the present work, rotational constants for the newly observed vibronic levels are not reported. The rotationless energy T_1 was determined from expression (4.1) using the rotation

Table 4.1. Vibrational term values T_ν, ω_e and $\omega_e x_e$ in cm^{-1} for the ground and excited electronic states of LaH. The numbers in parentheses are one standard error in the last digit.

State	ν	T_ν	ω_e	$\omega_e x_e$
$X^1\Sigma^+$	0	0.0	1418.2(2)	15.6(7)
	1	1387.1(5)		
	2	2742(2)		
$a^3\Delta_1$	0	1259.5(5)	1326.1[a]	
	1	2585.6(5)		
$a^3\Delta_2$	0	1646(1)	1357.7	15
	1	2973(5)		
	2	4269.3(5)		
$b^3\Pi_{0-}$	0	3542(1)		
$b^3\Pi_{0+}$	0	3586(1)		
$b^3\Pi_1$	0	3754(1)	1312[a]	
	1	5066(1)		
$b^3\Pi_2$	0	4048(2)		
$A^1\Pi$	0	4533.55933(80)[b]	1283.6[a]	
	1	5817.2(5)		
$B^1\Delta_2$	0	6057(2)		
$d^3\Phi_2$	0	7215.4(5)	1203.6[a]	
	1	8419.0(5)		
$d^3\Phi_3$	0	7884(1)		
	2	10281.1(5)		
$^3\Phi_2$	0	16878.3(5)		
$^3\Phi_3$	0	17653(1)		
0^+	0	19854.6(5)		

[a] $\Delta G_{1/2}$ values

[b] Ref [86]

constants given in Ref. [86]. Same approach was used for the states where more precise rotational constants were known from the previous work. However, for those vibronic levels where the rotational constants were not known, for example ν = 2 of the ground state, the reported term values were determined by fitting the rotational constant B_v and disregarding the D constant. In such cases, the vibronic term values are accurate to maximum 5 cm^{-1}. Further ω_e = 1418.2(2) cm^{-1}, $\omega_e x_e$ = 15.6(7) cm^{-1} were obtained by using the following relation,

$$\Delta G = G(v) - G(0) = \omega_e v - \omega_e x_e v(v+1) \tag{4.2}$$

The T_v, ω_e and $\omega_e x_e$ values for the ground state are listed in Table 4.1.

4.3.2 Assignment of $a\,^3\Delta$ state

The rotational structure at ~1259.5 cm^{-1}as shown in Fig. 4.1(b) consisted of *PQR* triplets with a strong *Q*-line and $I_P > I_R$, when either a *P*- or *R*-line of $0^+(^3\Sigma^-)$-$X^1\Sigma^+$ transition was excited. This is in accordance with $\Delta\Omega$ = -1 transition, confirming Ω = 1 of the lower state. Additionally, we observed only one line, *P*(1) and two lines, *Q*(1) and *P*(2) in the DF spectra while populating respectively J = 0 and 1 level of the $0^+(^3\Sigma^-)$ state, which further confirms that the lower state has Ω = 1. This is the lowest excited state observed in the present work. Das and Balasubramanian [85] also predicted $^3\Delta$ as the first excited state with Ω = 1 at 2580 cm^{-1}. This confirmed that the state observed at 1259.5 cm^{-1} is Ω = 1 component of $a^3\Delta$ state i.e. $a^3\Delta_1$ sub-state. This observation is important for establishing the missing energy link between the singlet ground and $a^3\Delta$ state. We also observed first vibration of $a^3\Delta_1$ at T_1 = 2585.6 cm^{-1} as evident from the *PQR* structure and is marked in Fig.4.1 (b).The term values of ν = 0,1 of $a^3\Delta_1$ state are listed in Table 4.1. Similarly, Ω = 2 component of $a^3\Delta$ state was identified at T_0 = 1646 cm^{-1} (see in Fig. 4.2). This observation was confirmed by observing a resolved *PQR* triplet structure in DF spectra, with strong *Q*-line and $I_P > I_R$, irrespective of excitation to $J \geq 3$,*e*- or *f*-parity levels of *D*1 and *E*1 state, which were assigned as $^1\Pi$ states in the chapter 3. Further confirmation of this state comes from the observation of two lines, *Q*(2) and *P*(3) in the

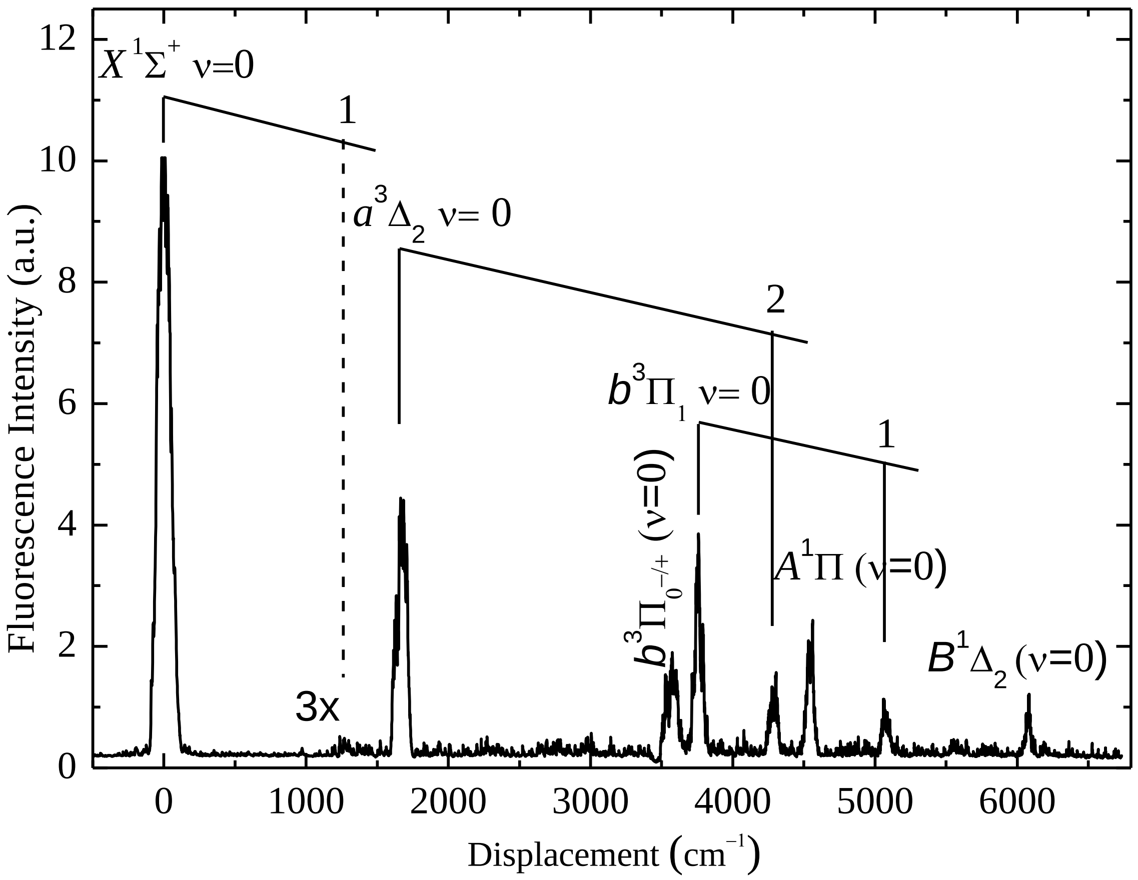

Figure 4.2. Laser-induced dispersed fluorescence spectra of LaH observed by exciting *R*(0)-line of the (0,0) band of *E*1-$X^1\Sigma^+$ transitions. Thus J = 1 (e-parity) level of *E*1 state is populated. The x-axis shows the displacement in cm^{-1} from the excitation line.

DF spectra while populating J = 2 and one line, *P*(2) while populating J = 1 level of the *D*1 and *E*1 states. We also observed ν = 2 of this state at T_2 = 4269.3 cm^{-1}, whereas ν = 1 remained undetected in this excitation. However, it was detected in the DF spectrum of [20.0]Ω = 1 excited state and is shown in Fig. 4.3. From this figure we noticed that the peak at 2973 cm^{-1} was corresponding to ν = 1 of $a^3\Delta_2$ state. Thus we determined $\Delta G_{1/2}$ = 1326.1 cm^{-1} for $a^3\Delta_1$ state and ω_e = 1357.7 cm^{-1}, $\omega_e x_e$ = 15 cm^{-1} for $a^3\Delta_2$ state from T_v values of ν = 0, 1, 2 and are in good agreement with each other. As expected, the vibrational frequencies did not change within spin-orbit components. The values are listed in Table 4.1. As seen from the Table 4.1 the experimental ω_e value for $a^3\Delta$ state compares well with the *ab initio* value [85] of 1352 cm^{-1}.

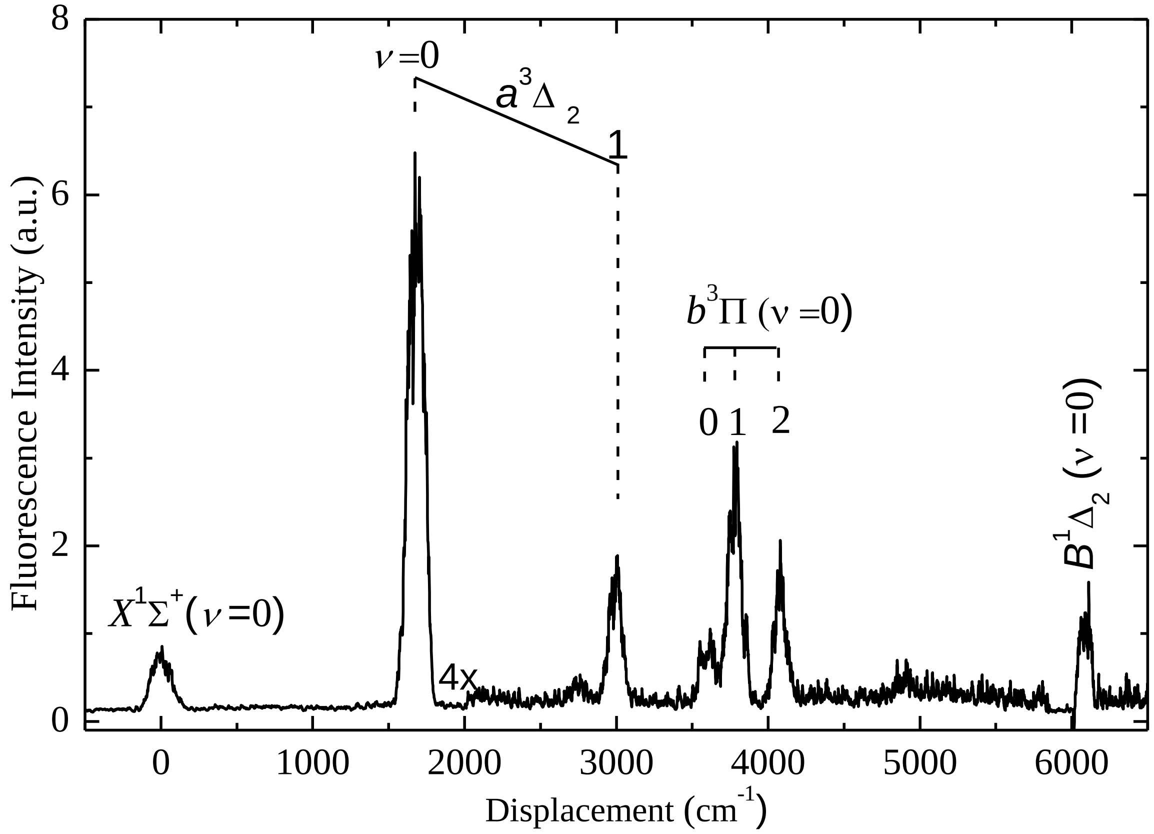

Figure 4.3. Dispersed fluorescence spectrum of LaH observed by exciting the *R*(2) line of the (0,0) band $[20.0]\Omega = 1\text{-}X^1\Sigma^+$system.

4.3.3 Assignment of $^3\Pi$ and $^1\Delta$ states

The DF spectrum at moderate resolution originating from the *E*1 state is shown in Fig. 4.2. The DF spectra obtained from *D*1 state also shows identical features.

The spectra in the 3000-6500 cm^{-1} range shows 6 peaks at ~3564, 3754, 4269.3, 4533.6, 5066 and 6057 cm^{-1}. Das and Balasubramanian [85] predicted an inverted $^3\Pi$ state with its spin-orbit component $^3\Pi_2$ at 4815, $^3\Pi_1$ at 5166, $^3\Pi_0^+$ ($^3\Pi_0^-$) at 5474 (5520) and $^1\Delta_2$ state at 6567 cm^{-1}. Considering the theoretical overestimation trend of ≥1000 cm^{-1}

for the observed term values of the $a^3\Delta$ state in the present work and $A^1\Pi$ and $C^1\Sigma^+$ in the earlier work [86,90] , these $^3\Pi$ and $^1\Delta$ states are expected in this energy range. In order to establish symmetries of these states, we recorded DF spectra at higher resolution. A single DF line at 3564 cm^{-1} split into three-line pattern under higher resolution irrespective of excitation to *e*- or *f*-parity level of the *E*1 state. Among these three lines one was stronger than the other two. The DF line pattern was different while exciting the same *J* with different *e*- and *f*- parity of the upper state (Fig. 4.4(a)). The separation between the weak lines monotonically increased with *J* of the upper state and if this is considered as *PR*-doublets, provides a reasonable value of the rotational constant of LaH. However, the spacing between the stronger line with respective to any of the weaker lines was inconsistent with the rotational constant of LaH. This indicated that the two weak lines (*PR*-doublets) belong to one state and the strong line (*Q*) belongs to the other state. This observation is consistent with $^3\Pi_{0^\pm}$ assignment for the lower state. As shown in Fig. 4.4, with the *e*- (*f*-) parity excitation of the upper state, the *PR*-doublets emit to $^3\Pi_{0^+}$ ($^3\Pi_{0^-}$) state and Q-line connect to $^3\Pi_{0^-}$ ($^3\Pi_{0^+}$) state. Considering this state as $\nu = 0$, the term energy for the $^3\Pi_{0^+}$ and $^3\Pi_{0^-}$ was estimated to be 3586 and 3542 cm^{-1} respectively. Being the second excited state as observed in the present experiment, which was also predicted so from theory, we designated this state as $b\,^3\Pi_{0^\pm}$. The single lines at 3754 and 5066 cm^{-1} (see in Fig 4.2) were resolved into *PR* doublets, irrespective of excitation to *e*- or *f*- levels of the *D*1 and *E*1 upper states is shown in Fig. 4.5. Since the upper states were assigned as $^1\Pi$ ($\Omega = 1$) in the chapter 3 and the transitions are typical to $\Delta\Omega = 0$, both the lower states have $\Omega = 1$.This indicates that the 3754 cm^{-1} state is $\Omega = 1$ spin-orbit component of the $b^3\Pi$ and its first vibration is located at 5066 cm^{-1}. Thus the $\Delta G_{1/2}$ value

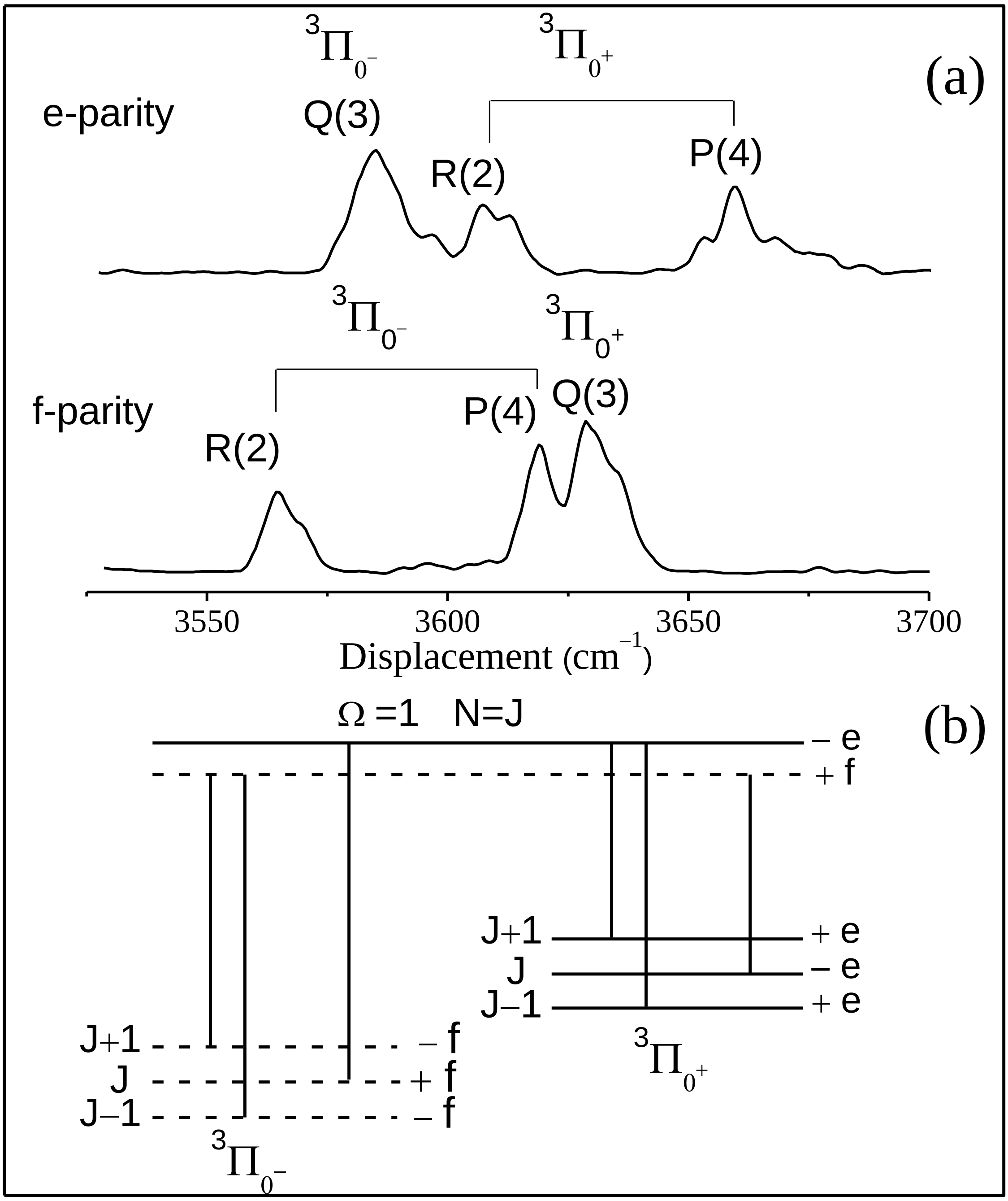

Figure 4.4. (a) High-resolution dispersed fluorescence patterns from *e*- and *f*- symmetry levels of *E*1 (J = 3) to $^3\Pi_0{}^+$ and $^3\Pi_0{}^-$ states. (b) The relevant energy levels of the upper and the lower states involved in the *E*1-$b^3\Pi_{0^\pm}$ transition is also shown.

of 1312 cm^{-1} obtained for $b^3\Pi_1$ is consistent with ω_e = 1341 cm^{-1} predicted from the *ab initio* studies [85]. The DF spectrum from the *R* (2) line of the [20.0]Ω = 1 state in Fig.4.3

shows the third spin-orbit component (Ω = 2) of $b^3\Pi$ state at T_0 = 4048 (2) cm^{-1}.Thus contrary to the prediction of *ab initio* studies [85] the spin-orbit splitting of the $b^3\Pi$ state is observed as regular and the spin-orbit separation respectively of 190 cm^{-1} between Ω = 0 to 1 and 294 cm^{-1} between Ω = 1 to 2 components of $b^3\Pi$ state are in poor agreement with the *ab initio* values respectively of –331 and –351 cm^{-1}.

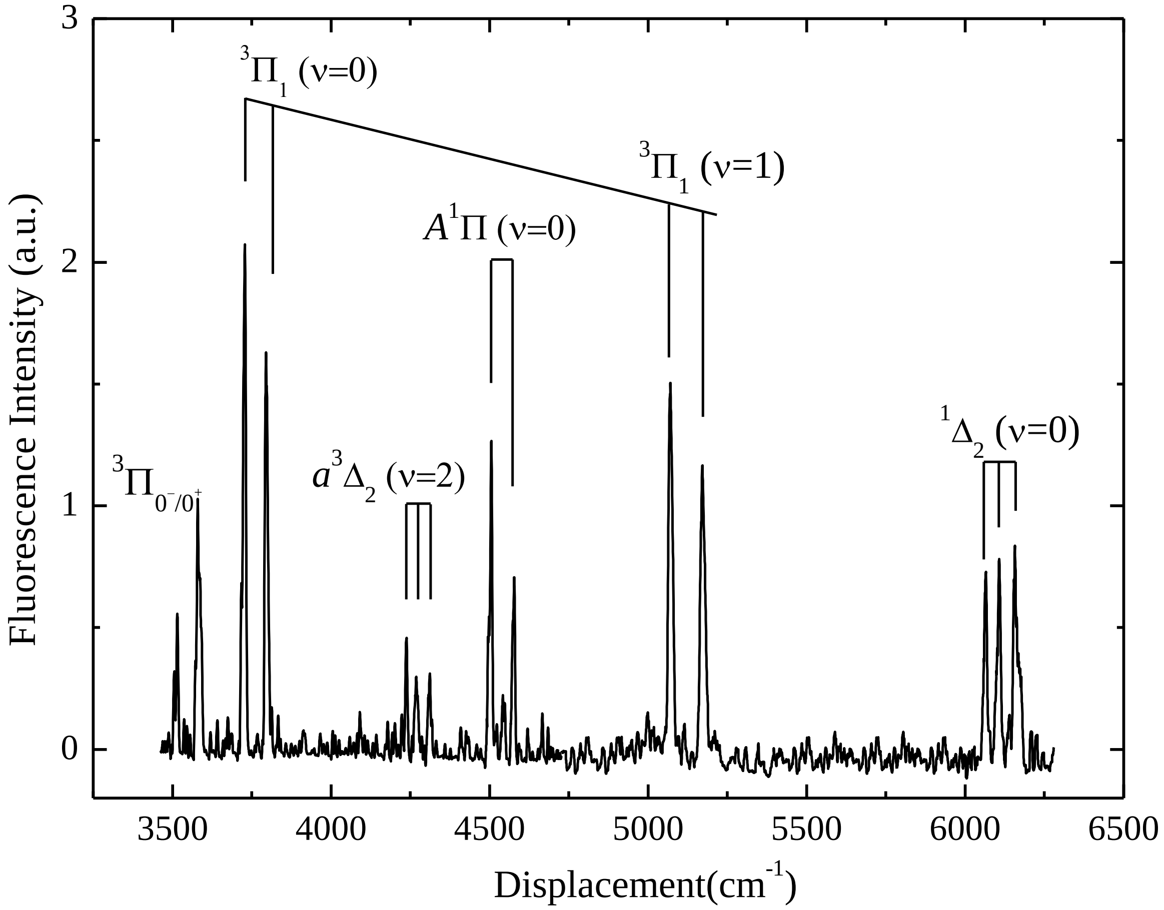

Figure 4.5. High-resolution dispersed fluorescence patterns from *e*-parity level (J = 3) of *D*1 to various low lying electronic states. The x-axis shows the displacement in cm^{-1} from the excitation line.

The state at 4533.6 cm^{-1} was identified earlier by Ram and Bernath [86] as $A^1\Pi$. The DF spectrum for this state consisted of *PR* doublets as expected irrespective of excitation to the *e*- or *f*-parity levels of upper *D*1 and *E*1 states and is shown in Fig.4.5. A new $B^1\Delta_2$ state was observed at T_0 = 6057 cm^{-1}, which was predicted at T_e = 6567 cm^{-1} from *ab initio* studies [85]. The single line at 6057 cm^{-1} as shown in Fig. 4.2 was resolved into *P*,*Q* and *R* triplets, with strong *Q*-line and $I_P > I_R$ indicating a $\Delta\Omega = -1$ transition as shown in Fig. 4.5. Ram and Bernath [86] investigated (0,0) and (1,1) bands of $A^1\Pi$–$X^1\Sigma^+$ and $d^3\Phi_2$-$a^3\Delta_1$ and (0,0), (1,1) and (2,2) bands of $d^3\Phi_3$–$a^3\Delta_2$ systems in the infrared. However, they did not observe any off- diagonal vibrational transitions ($\nu' \neq \nu''$) in any of those systems and therefore could not determine the vibrational constants for these states. The observation of ground state vibrations has enabled us to determine the $\Delta G_{1/2}$for the $A^1\Pi$ state. Similarly, the term energies of the earlier observed $d^3\Phi_{2,3}$ and $^3\Phi_{2,3}$ and 0^+ states [83,86] were determined from the derived term energies of $a^3\Delta_{1,2}$ states in the present work and are listed in Table 4.1.

4.4 Discussion

Theoretical calculations of Das and Balasubramanian [85] have predicted that the low-energy electronic states $^1\Pi$, $^1\Delta$, $^3\Sigma^+$, $^3\Pi$ and $^3\Delta$ including the $^1\Sigma^+$ ground state arise from La ground state configuration $5d6s^2$ (^{2}D) and H $1s^1$ (^{2}S) configuration (see Fig. 3.3). According to this calculation, the ground state of LaH has an electron configuration $1\sigma^2 2\sigma^2$ and the $^{1,\,3}\Delta$ and $^{1,3}\Pi$ states arise respectively from $2\sigma \rightarrow 1\delta$ the $2\sigma \rightarrow 1\pi$ electron promotions. These calculations show the contribution of various leading configurations in the low-energy electronic states. The $^{1,3}\Delta$, $^{1,3}\Pi$ and $^3\Sigma^+$ states respectively have $1\sigma^2 2\sigma 1\delta$ (97%) ,$1\sigma^2 2\sigma 1\pi$ (95%) and $1\sigma^2 2\sigma 3\sigma$ (52%) leading electron configurations. The *ab initio* calculations [85] also noted that the La (6*p*) orbital contribution is quite significant for most of states. The $^1\Sigma^+$ ground state of LaH has a La population of $5s^{1.524}6p^{0.216}5d^{0.972}$. Therefore, there is considerable participation of the 6p orbital of the lanthanum atom during bond formation and is *dsp* hybridized. Among the predicted low-energy states [85], $A^1\Pi$ state was observed earlier [86] and transitions from $a^3\Delta$ states to $^3\Phi$ states were reported [86,83]. However, the term energy of $a^3\Delta$ state was not known and also $^1\Delta$, $^3\Sigma^+$, and $^3\Pi$ states remained unobserved. In previous chapter $^1\Sigma^+$ symmetry for the ground state of LaH has been confirmed. In the present chapter observation of $b^3\Pi_{0,1,2}$ and $B^1\Delta_2$ states are reported along with the determination of term energy for $a^3\Delta_{1,2}$ state. Among the other low-energy states, the $d^3\Phi$ reported by Ram and Bernath [86] and $C^1\Sigma^+$ observed by Bernard and Chevillard [90] have an electronic configuration $1\sigma^2 2\pi^1 2\delta^1$ and $1\sigma^2 2\sigma^1 3\sigma^1$ respectively. These states correlate respectively to the excited atomic asymptotes d^2s^1 (^{2}F) and d^2s^1 (^{2}D) of La and s^1 (^{2}S) configuration of H [85]. Thus the low-energy states predicted by Das and Balasubramanian [85] up to 11000 cm^{-1} have now been observed. However, the $^3\Sigma^+$ state predicted at T_e = 11794 cm^{-1} [85] originating from La $5d6s^2$ (^{2}D) and H $1s^1$ (^{2}S) atomic asymptotes could not be observed. The term energy diagram including the energy levels of singlet and triplet multiplicity observed in the present and earlier work is shown in Fig.4.6. Prior to this work energy levels in the triplet stack was hanging with respect to the singlet one. Table 4.2 shows the comparison of spectroscopic constants of the low-energy electronic states (T_e, ω_e or $\Delta G_{1/2}$, spin-orbit splitting) obtained in the present work with the theoretical values [85]. As seen from the Table 4.2, while the *ab initio* values of the vibrational constants are found to be in good agreement with our experimental values, the term energies and spin-orbit separation of $^3\Delta_2$-$^3\Delta_1$, $^3\Pi_1$-$^3\Pi_0$, and $^3\Pi_2$-$^3\Pi_1$ are found to be in poor agreement. Prior to this work, the gas phase experimental values of vibrational constants for any of the electronic states of LaH were not known. The *ab initio* values of ω_e = 1433 cm^{-1} estimated by Das and Balasubramanian [85] and later ω_e = 1429 cm^{-1}, $\omega_e x_e$ = 20.93 cm^{-1} by Koseki *et al.* [91] for the ground state compare well with the experimental value of ω_e = 1418 and $\omega_e x_e$ = 15.6 cm^{-1}. Wang *et al.* [109]

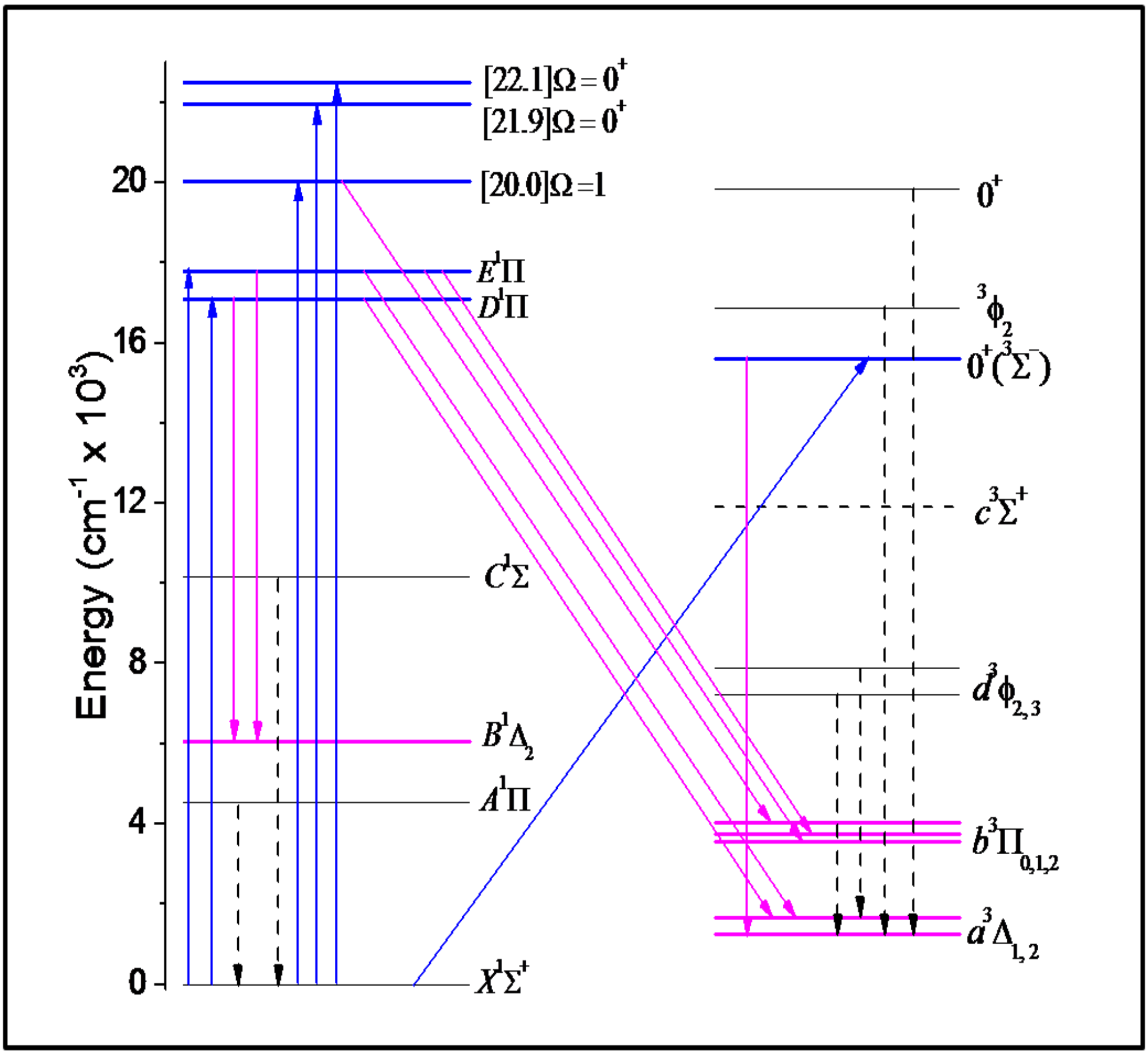

Figure 4.6. A schematic energy level of the electronic states of LaH molecule. Dashed line transitions are observed by previous authors, solid line transitions are observed in present work (blue and pink). The levels indicated by blue and pink lines are observed respectively in the excitation and dispersed fluorescence spectra reported in the present work.

have attributed a band at 1344.1 cm^{-1} to fundamental vibration of LaH in argon matrix. The red shift of 74 cm^{-1}in Ar matrix from the present gas phase value is too large to be accounted by matrix effects. However, this large red shift can be understood in terms of the ionic nature of the LaH molecule. The large positive dipole moment associated with the ground electronic states and the gross Mulliken population analysis [85] indicate the polar nature of La^{+}H^{-} bond with considerable electron transfer from La to H. As a result, H^{-}····Ar interaction is significant, weakening the La-H vibrational frequency and causing the red shift. For $a^3\Delta_2$ state, the *ab initio* ω_e value of 1352 cm^{-1} [85] is also in good

Table 4.2. Comparison of spectroscopic constants determined in the present work with theory.

State	T_0		ω_e		Spin-orbit splitting	
	Experiment[a]	Theory[b,c]	Experiment[a]	Theory[b]	Experiment[a]	Theory[b]
$X^1\Sigma^+$	0	0	1418	1433	-	-
$a^3\Delta_1$	1259	2540	1326.1[d]	1352	386.5	209
$a^3\Delta_2$	1646	2749	1357.7			
$b^3\Pi_{0-}$	3542	5474	-	1341	190	–331
$b^3\Pi_{0+}$	3586	5428	-			
$b^3\Pi_1$	3754	5120	1312[d]		294	–351
$b^3\Pi_2$	4048	4769	-	-		
$A^1\Pi_1$	4533.6[e]	6200	1283.6[d]	1309	-	-
$B^1\Delta_2$	6057	6500	-	-	-	-

[a] Present work
[b] Ref. [85].
[c] $\omega_e x_e$ disregarded while calculating T_0 from T_e.
[d] $\Delta G_{1/2}$ value.
[e] Ref. [86].

agreement with the experimental value of 1357.7 cm^{-1}. Also the presently determined $\Delta G_{1/2}$ = 1312 cm^{-1} for $b^3\Pi_1$ and 1283.6 cm^{-1} for $A^1\Pi$ state are in agreement with theory. Although *ab initio* studies predicted vibrations quite accurately it can be seen from Table 4.2 that the term energies were largely overestimated by more than 100% in some cases. Contrary to the prediction of *ab initio* studies [85], the spin-orbit splitting of the $b^3\Pi$ state is observed as normal. Also the spin-orbit separation of 386.5 cm^{-1} for $a^3\Delta_2$-$a^3\Delta_1$,190 cm^{-1} for $b^3\Pi_1$-$b^3\Pi_0$ and 294 cm^{-1} for $b^3\Pi_2$-$b^3\Pi_1$ are in poor agreement with *ab initio* values of 209,–331 and –351 cm^{-1} respectively. As shown experimentally in the previous chapter, the observed two high-energy $^1\Pi$ ($D1$ and $E1$) states separated by just 150 cm^{-1} were also not predicted by existing *ab initio* theory [85,91].

4.5 Comparison with Isovalent molecules

The current information on the electronic structure of LaH is compared with that of isovalent ScH and YH molecules. Based on erroneous *ab initio* calculations [57], $^3\Delta$ state was assigned as the ground state for all the three molecules, ScH [110], YH [58] and LaH [83]. Later *ab initio* calculations which included electron correlation and relativistic effects have predicted a $^1\Sigma^+$ ground state for ScH [111,112,113,107], YH [62,63] and LaH [85,91]. Table 4.3 shows the comparison of experimental values with *ab initio* values for energy ordering for ground and low-energy states with their assignment and their internuclear distances for ScH, YH and LaH. The observed electronic states in ScH, YH and LaH are shown in Fig. 3.1, 3.2 and 4.6 respectively. As seen from the Table 4.3 and Figures 3.1, 3.2, 4.6, there are strong similarities between the low-lying electronic states of LaH, YH, and ScH. The ground state for these molecules is a $X^1\Sigma^+$ state which arises from the $1\sigma^2 2\sigma^2$ electron configuration. For YH, the ground state is well separated from the rest of the excited states while in LaH, the ground state is closer to the $^3\Delta$ excited

Table 4.3. Comparison of experimental term energies and internuclear distances for ground and low-energy states of LaH, YH and ScH with *ab initio* values.

Electronic states	LaH				YH				ScH			
	T_0 (cm^{-1})		r_e(Å)		T_0 (cm^{-1})		$r_e[r_0]$ (Å)		$T_0[T_e]$ (cm^{-1})		$r_e[r_0]$ (Å)	
	Expt.[a]	Theory[b]	Expt.[c]	Theory[b]	Expt.[d]	Theory[e]	Expt.[d]	Theory[e]	Expt.[f]	Theory[g]	Expt.[f]	Theory[g]
$X^1\Sigma^+$	0.0	0.0	2.031969	2.08	0.0	0.0	1.922765	1.865, 1.961[h]	0.0	0.0	1.775427	1.804
$^3\Delta_1$	1259.5	2540	2.099924	2.13	6205	9009	[2.04709]	1.944	-	-	-	-
$^3\Delta_2$	1646	2749	2.083181		6338	8961	[2.00546]		-	-	-	-
$^3\Delta_3$	-	2588	2.081242		6562	9023	[1.98319]		-	-	-	-
$^3\Pi_0^-$	3542	5474	-	2.12	-	7873	-	1.907	-	-	-	-
$^3\Pi_0^+$	3586	5428	-		-	7894			-	-	-	-
$^3\Pi_1$	3754	5120	-		-	8177	-		-	-	-	-
$^3\Pi_2$	4048	4769	-		-	8448	-		-	-	-	-
$A^1\Pi^i/A^1\Delta^j$	4533.6[c]	6200	2.074276	2.13	9848	10920	2.03153	1.950	4185	[4450]	[1.895011]	1.947
$B^1\Delta^i/B^1\Pi^j$	6057	6500	-	2.16	9859	12620	1.96308	1.944	5404	[7420]	1.851706	1.926

[a] Present work,; [b] Ref.[85] $\omega_e x_e$ disregarded while calculating T_0 from T_e,; [c] Ref.[86],; [d] Ref.[87,101, 103],; [e] Ref.[63] $\omega_e x_e$ disregarded while calculating T_0 from T_e,; [f] Ref.[99,100],; [g] Ref.[112],; [h] Ref.[62],; [i] Electronic state of LaH,; [j] Electronic state of YH and ScH.

state. For ScH the predicted first excited state is $^3\Delta$ and is observed experimental by our group [40], however its term energy is not yet known. Ram and Bernath have observed low-energy singlet states at 4185, 5404 cm^{-1} for ScH and assigned them as the $A^1\Delta$, $B^1\Pi$ states respectively [99,100]. Similarly in the case of YH, low-energy singlet states were observed at 9848, 9859 cm^{-1} and were assigned as $A^1\Delta$, $B^1\Pi$ states respectively [103]. However in case of LaH, the first low-energy singlet state was observed at 4533 cm^{-1} and this state was assigned as $A^1\Pi$ [86], arising from $1\sigma^2 2\sigma^1 1\pi^1$(95%) electron configuration, and the other singlet state which was observed in the present work at 6057 cm^{-1} was assigned as the $B^1\Delta$ state and it comes from $1\sigma^2 2\sigma^1 1\delta^1$(97%)electron configuration. In general we expect the elongation of the bond length as we move from Sc to La. The experimental equilibrium bond lengths r_e for the ground states of ScH, YH and LaH are 1.775427(8), 1.922765(8) and 2.031969(20) Å respectively and are comparable with their *ab initio* values as given in Table 4.3. From Table 4.3 we can infer that the ground state experimental r_e value increase by 14.4 % as we move from ScH to LaH through YH and it closely matches with the predicted *ab initio* value of 15.3 %. The experimental internuclear distances for the other low-energy states are compared with *ab initio* values and are given in Table 4.3. Table 4.4 shows the comparison of experimental vibrational frequencies for ground and low-energy states of LaH, YH and ScH molecules with the *ab initio* values. The observed ground state vibrational frequency decreases from LaH to ScH through YH. The predicted dissociation energy D_e for LaH [85] and YH [63] were 2.60 and 3.05 eV respectively and there is no experimental value for comparison. Langhoff *et al.* [62] also calculated De value 2.95 eV for YH which is compares well with the Balasubramanian value [63]. However for ScH, the dissociation energy D_0 was 2.06(9) eV determined from mass spectrometric monitoring of high temperature equilibria [114].

Table 4.4. Comparison of experimental vibrational frequencies (ω_e in cm^{-1}) for ground and low-energy states of LaH , YH and ScH molecules with *ab initio* values.

Electronic state	LaH		YH		ScH	
	Expt.[a]	**Theory**[b]	**Expt.**[c]	**Theory**[d]	**Expt.**[e]	**Theory**[f]
$X^1\Sigma^+$	1418	1433	1530	1510,1558[h]	1547[g]	1621
$^3\Delta$	1358	1352	1565[g]	1433	-	1460
$^3\Pi$	1312[g]	1341	-	1489	-	1438
$A^1\Pi$[i]/$A^1\Delta$[j]	1284[g]	1309	1339[g]	1366	-	1479
$B^1\Delta$[i]/$B^1\Pi$[j]	-	1299	1342[g]	1380	1410	1418
$C^1\Sigma^+$	-	1230	1207[g]	-	1368[g]	1396

[a] present work,; [b] Ref. [85],; [c] Ref.[87,101, 103],; [d] Ref.[63],; [e] Ref.[99,100],; [f] Ref.[112],; [g] $\Delta G_{1/2}$ value,; [h] Ref.[62],; [i] Electronic state of LaH,; [j] Electronic state of YH and ScH.

Table 4.5 shows the experimental term values and internuclear distances for high-energy exited electronic states of LaH, YH and ScH molecules with the *ab initio* values. The high-energy singlet states $C^1\Sigma^+$, $D^1\Pi$ were respectively observed at 10151, 17398 cm^{-1} in LaH, and at 14295, 19573 cm^{-1} in YH, and at 13574, 16845 cm^{-1} in ScH molecule. *Ab initio* calculations predicted first low-lying triplet was $^3\Delta$ state for LaH [85] and ScH [107], while $^3\Pi$ state for YH [63]. However, experimentally observed the first low-lying triplet state in LaH and YH was $a^3\Delta$. This observation of the $a^3\Delta$ state as the lowest excited state in YH is not in concurrence with the *ab initio* results of Balasubramanian and Wang [63] who predicted $^3\Pi$ state to be the lowest excited state, but the observation is in agreement with the work of Langhoff *et al.* [62], who placed a $^3\Delta$ state below the lowest $^3\Pi$ state. Based on the energy separation of ground and $a^3\Delta$ states all the singlet and triplet stack of electronic states were placed energetically with respect

Table 4.5. Comparison of experimental term energies and internuclear distances for high-energy states of LaH, YH and ScH with *ab initio* values.

Electronic states	**LaH**				**YH**				**ScH**			
	$T_0[T_e]$ (cm^{-1})		**$r_0[r_e]$ (Å)**		**$T_0[T_e]$ (cm^{-1})**		**$r_0[r_e]$ (Å)**		**$T_0[T_e]$ (cm^{-1})**		**$r_0[r_e]$ (Å)**	
	Expt.[a]	Theory[b]	Expt.[a]	Theory[b]	Expt.[c]	Theory[d]	Expt.[c]	Theory[d]	Expt.[e]	Theory[f]	Expt.[e]	Theory[f]
$C^1\Sigma^+$	10151	12923	2.152983	2.20	14295	[15050]	2.007960	[2.034]	13574	15048	[1.869043]	1.889
$d0^+$	15623[g]	16016	2.1233[g]	2.17	15756	-	2.0197		-	-	-	-
$e^3\phi_2$	7215	10516	[2.148351]	2.19	17583	-	2.06764	-	-	-	-	-
$e^3\phi_3$	7884		[2.141420]		17867	-	2.05090	-	-	-	-	-
$e^3\phi_4$	z+6306		[2.124420]		18146	-	2.02906	-	-	-	-	-
$D^1\Pi$	17398[g]	18033[h]	2.09938[g]	-	19573	-	-	-	16850	[18160]	1.93349	-
$E^1\Pi$[i]/ $E0^+$ [j]	17549 [g]	20124	2.11485[g]	2.19	23213	-	2.307	-	-	-	-	-
[20.0]$\Omega = 1$[i]/ $F\ 1$[j]/ $F^1\Sigma^-$ [k]	20042 [g]	-	2.06811[g]	-	23427	-	1.891	-	19072	[19920]	1.86876	-
$g^3\phi_2$	16878	-	2.09924	-	-	-	-	-	-	-	-	-
$g^3\phi_3$	17653	-	2.0845	-	-	-	-	-	-	-	-	-
$h0^+$	19855	-	2.1011	-	26136	-	-	-	-	-	-	-
[21.9]$\Omega = 0^+$	21971 [g]	-	2.19199[g]	-	-	-	-	-	-	-	-	-
[22.1]$\Omega = 0^+$	22100 [g]	-	2.2630[g]	-	-	-	-	-	-	-	-	-

[a] Ref.[83,86,90],; [b] Ref.[85] $\omega_e x_e$ disregarded while calculating T_0 from T_e,; [c] Ref.[87,101],; [d] Ref.[63],; [e] Ref.[99,100,115],; [f] Ref.[112],; [g] Present work,; [h] Ref.[91],; [i] Electronic state of LaH,; [j] Electronic state of YH,; [k] Electronic state of ScH.

to one another in LaH and YH molecules. However in case of ScH, the first triplet-triplet ($g^3\phi_2$–$a^3\Delta_1$) transition was observed recently in our laboratory [40] but due to the lack of inter-combination transition, we could not place the singlet and triplet stack of electronic states with respect to one another. The $b^3\Pi$ state was predicted in all the three molecules but observed only in LaH. Similarly, $c^3\Sigma^+$ state was predicted but not observed in all the three molecules. The $d0^+(^3\Sigma^-)$ state was observed in YH and LaH molecules at 15756 and 15623 cm^{-1} respectively. However this $^3\Sigma^-$ state was predicted also for isovalent ScH by Anglada *et al.* [107] but has not been observed. The $^3\phi$–$a^3\Delta$ transitions were observed in both YH [58] and LaH [83] molecules and very recently in ScH [40] also. Still there is deficiency in *ab initio* calculations for high-energy electronic states of LaH, YH and ScH molecules and more refined calculations are required for the better understanding of the electronic structure of these three isovalent molecules.

4.6 Conclusions

The principal new results emerging from this dispersed fluorescence study in LaH are the observation of three low-energy states namely $a^3\Delta$, $b^3\Pi$ and $B^1\Delta$. Observation of the low-lying $a^3\Delta$ state with its spin-orbit component Ω = 1 and 2 lying respectively at 1259.5 and 1646 cm^{-1} enabled us to establish an energy linkage between the triplet states observed in the earlier work [86,83] with respect to the singlet ground state $X^1\Sigma^+$. Equilibrium vibrational constants for the ground and $a^3\Delta$ states were also determined. The present study completes the observation of all the states up to 11000 cm^{-1} predicted by *ab initio* studies [85]. However, there are still few discrepancies between experiment and theory. Although *ab initio* studies predicted vibrations quite accurately, the term energies and spin-orbit separations were largely overestimated. Contrary to the *ab initio* prediction, the spin-orbit splitting of the $b^3\Pi$ state was observed as normal. We hope that these discrepancies between the present observations and earlier theoretical results may stimulate more refined *ab initio* electronic structure of LaH. The current information on the electronic structure of LaH was compared with that of isovalent ScH and YH molecules.

Chapter 5

Laser-induced Fluorescence (LIF) excitation Spectroscopy of jet-cooled zirconium nitride (ZrN) molecule

5.1 Introduction

Transition-metal elements (TMs) are found in the atmospheres of cool S- and M-type stars in their metal monoxide and monohydride forms [10,15,22,78,116-119] due to high cosmic abundance of Oxygen and Hydrogen. High dissociation energy of 3*d* metal diatomic oxides makes them stable in low-temperature stars and many of them have been detected in the spectra of cooler stars (M-type) [10]. Since transition metal nitrides and oxides often have similar bond energies, the nitrides are also expected to be present in the stars. Although metal nitride molecules have not been observed yet in stellar atmospheres, they would provide valuable information on the abundance of nitrogen. Precise spectroscopic data is necessary for a meaningful search for these molecules in complex stellar spectra. The transition-metal containing diatomics are highly refractory materials and this makes it difficult to get them into the gas phase under non-equilibrium low temperature conditions. High temperature often complicates the spectra because of the complex electronic structure associated with them. The electronic spectra of transition metal nitrides, particularly in the visible region, are expected to be very complex because of a presence of high density of states, complicated by high spin multiplicities and large spin-orbit intervals. These problems are the result of a large number of unpaired *d* electrons. Many of the electronic states and spin components interact with each other causing extensive perturbations. Although the electronic structure of many gaseous transition-metal oxides, carbides, and hydrides are relatively well-characterized, following transition metal nitrides are known. For 3*d* transition metal series, ScN [37,38,120], TiN [121-127], VN [128-131], CrN [131-133], FeN [134] and 4*d* transition metal series, YN [101,135], ZrN [136-142], NbN [143,144], MoN [145-149], RuN [150,151], RhN[105] and 5*d* transition metal series, HfN [152], TaN [153], WN [154], ReN [155,156], OsN [157,158] IrN [159-161], PtN [162,163] have been studied in the gas phase.

The importance of transition metal nitrides is well-known [164,165]. The group IV metals are finding increased importance in the semiconductor industry. TiN, HfN, and ZrN are excellent diffusion barrier layers in silicon semiconductors because of their slow diffusion rates and high conductivity [166]. The electronic structures, dynamics of formation, and bonding in bulk and gas phase cluster materials have become of significant interest to materials scientists and chemists alike [166-169]. In industrial processes, ZrN is one of the materials that has the best mechanical properties and is deposited by physical vapour deposition to coat medical devices, industrial parts, automotive and aerospace components, and other parts subject to high wear and corrosive environments [170-173]. Transition metals like titanium, zirconium, or hafnium metal boride, carbide, oxide, nitride, and silicide materials have some of the highest melting points in nature. These materials also have a high degree of spectral selectivity, high hardness, and improved wear, corrosion, and oxidation resistance and thus they have potential applications in high temperature solar-selective coatings [174]. Transition-metal play a vital role in nitrogen fixation in biological systems [175], production of ammonia [80], and pollution control [29] and thus understanding of transition metal nitrogen bond is important. In this context, in our laboratory recently we have undertaken the electronic structure investigation of ScN molecule [37,38] where the ground state symmetry $^1\Sigma^+$ was confirmed and characterized new low- and high-lying electronic states. In the present work, we have studied the ZrN molecule in order to improve their molecular constants of ground and excited states at equilibrium.

Bates and Dunn [176] first studied the spectra of ZrN molecule, (0,0) band of $B^2\Sigma^+$ - $X^2\Sigma^+$ system in violet and (0,0), (1,1), and (2,2) bands of $A^2\Pi$-$X^2\Sigma^+$ system in yellow spectral range using conventional emission spectroscopy. They determined the molecular constants for $\nu = 0$ of $X^2\Sigma^+$ and $B^2\Sigma^+$ and $\nu = 0$-2 of $A^2\Pi$ states. In the yellow system, they reported severe perturbations in $A^2\Pi_{3/2}$-$X^2\Sigma^+$ sub-band and their spectral analysis in the violet system was hampered by the limited observations especially, the absence of low-*J* rotational lines. Bates and Gruen [177] confirmed the $X^2\Sigma^+$ as the ground state of ZrN by matrix isolation spectroscopy. Later, Cheung and co-workers revisited the yellow and violet band systems of ZrN [136-142] using laser-induced fluorescence (LIF) spectroscopy. They studied the previously observed (0,0), (1,1), and (2,2) bands [137,138,140] of $A^2\Pi$-$X^2\Sigma^+$ system for the various isotopomer of ZrN and determined the magnetic hyperfine structure of the $X^2\Sigma^+$ state of ^{91}ZrN [136,142]. Moskvitina and Kuzyako [178] also investigated the electronic vibrational–rotational spectrum of *A*-*X* system of ZrN molecule by using intracavity laser spectroscopy method and they revised the molecular constants for ground state $X^2\Sigma^+$ and excited state $A^2\Pi$. More recently, Farhat *et al.* [179] computed the potential energy curves for 21 low-lying electronic states of the ZrN molecule using Complete active space self-consistent field (CASSCF) and Multi reference single & double excitation configuration interaction (MSRDCI) methods, out of the 21 states 15 are new low-lying excited electronic states in the doublet and quartet manifolds.

The ZrN molecule is isoelectronic with YO [180] and ScO [39,181-184] and isovalent with TiN [121-127] and HfN [152]; In view of the perturbations observed in the spectra of these isovalent and isoelectronic molecules, it is not surprising that the spectrum of ZrN is also perturbed. The present study deals with the study of excited electronic states of zirconium nitride (ZrN) molecules. The motivation for this work is to extend the observation and analysis of the $B^2\Sigma^+$-$X^2\Sigma^+$ and $A^2\Pi$-$X^2\Sigma^+$ systems to the higher vibrational levels. Since this molecule is of astrophysical interest, it is important to gather as much spectroscopic information as possible for a meaningful search of its existence in the stellar atmosphere.

5.2 Experiment

The ZrN molecules are produced in a pulsed supersonic free-jet apparatus, which is discussed in detail in the Chapter 2. In brief, a rotating and translating zirconium metal rod is ablated with the third harmonic beam (354.7 nm, ~10-15 mJ/pulse) of a Nd: YAG laser focused to an ~1 mm^2 spot. The laser produced Zr metal plasma reacted with 2% ammonia seeded in He gas emerging from a pulse valve under a backing pressure of 275 kPa (2.75 bar) to produce cooled ZrN molecules. The ZrN molecules are probed tunable pulse dye laser. The resulting laser-induced fluorescence is imaged on an entrance slit of a monochromator equipped with a Peltier cooled photomultiplier tube. The excitation spectra are obtained by scanning the pulsed dye laser and recording the laser-induced fluorescence through the monochromator set at fixed wavelength corresponding to the strongest fluorescence terminating either to a ground or an excited state. Here monochromator is used as a broad band filter. The excitation spectra are obtained with a typical resolution of 0.08 cm^{-1}. Transition wavenumbers are calibrated by using a laser wavelength calibration facility of the dye laser utilizing neon optogalvanic spectral lines as well as by known atomic lines of Zr I [185] appeared in the spectra with an absolute precision of ~0.1 cm^{-1}. The dispersed fluorescence (DF) spectra are recorded by scanning the monochromator. Lifetimes of the excited electronic states are recorded by acquiring the fluorescence decay curve on a 200 MHz digital storage oscilloscope having sampling rate of 2 Giga-samples/s and a rise time <2 ns. The decay curve is averaged for 128 shots in order to obtain a good signal to noise ratio.

5.3 Data analysis and results

5.3.1 $B^2\Sigma^+$-$X^2\Sigma^+$ system

Naturally abundant ammonia and zirconium are used in this study. Naturally abundant Zr has five isotopes, ^{90}Zr (51.45%), ^{91}Zr (11.23%), ^{92}Zr (17.11%), ^{94}Zr (17.40%) and ^{96}Zr (2.80%). The spectral resolution employed in the present study does not permit to observe isolated rotational branches for each ZrN isotopic molecule. However, by simulating *B*-*X* (0,0) band with the data from ref. [141] with a resolution ~0.1 cm^{-1}, we could infer that the peaks corresponding to P_1 and P_2 branches of the main isotope ^{90}ZrN gets only slightly blended by P_2 of other two ^{92}ZrN and ^{94}ZrN isotopes. The rotational branches of ^{91}ZrN and ^{96}ZrN are expected to be weak because of their lower natural abundance. This simulated spectra of ZrN isotopic molecule for a given rotation N is in agreement with our experimental observations and in this work we report the spectral analysis of ^{90}Zr^{14}N molecule. First, Bates and Dunn [176] and later Chen *et al.* [141] observed and analyzed *B*-*X* (0,0) band. Bates and Dunn reported that their analysis was hampered by the absence of low-*J* rotational lines and perturbations maximized at $N = 44$ caused by an interacting excited vibrational level of $A^2\Pi$ sub-state. Chen *et.al* [141] determined the rotational constants for three isotopic molecules ^{90}ZrN, ^{92}ZrN and ^{94}ZrN. They found that all the rotational branches were perturbed and made efforts to identify the perturbing state and concluded that further high-resolution studies were necessary for establishing the identity of the perturbing state unambiguously. They searched for the (1,0) band of this transition but did not observe it and concluded a very unfavorable Franck-Condon factor as the reason. However in the present work, we observed (1,0), (1,1), (2,0), (2,1), (2,3) bands with considerable intensity and a weak (3,4) band. All the bands other than (3,4) were rotationally analyzed by simulating the spectra with the Pgopher program [106] to determine the molecular constants. The portion of the (1, 0) and (2, 0) bands are shown in Fig.5.1 and 5.2 respectively. The rotational constants for ν = 1, 2 of B state were determined by fitting the rotational line positions to energy level expression for $^2\Sigma^+$ state given in the Pgopher program [106]. The $X^2\Sigma^+$ and $B^2\Sigma^+$ states follow the case (b) where the electron spin **S** is strongly coupled to rotation **N**. The vector coupling is then **J** = **N** + **S** and the F_1 and F_2 rotational sublevels correspond to $N = J - 1/2$ and $N = J + 1/2$, respectively. The term value for the two sublevels of both states can be expressed as,

$$T_{1v}(N) = T_v + B_v[N(N+1)] - D_v[N(N+1)]^2 + \frac{\gamma_v}{2}N \tag{5.1}$$

and

$$T_{2v}(N) = T_v + B_v[N(N+1)] - D_v[N(N+1)]^2 - \frac{\gamma_v}{2}(N+1) \tag{5.2}$$

where B_v , and D_v are the rotational constant and its higher-order correction and γ_v is spin-rotation constant. The wavenumbers of observed rotational lines with their assignments of all bands of ^{90}ZrN molecules are given in Appendix B.

In the (1,0) band, clear rotational lines N up to 16 in the P and N up to 14 in the R branch were observed, where it forms band head in R. Similarly, in the (2,0) band, P

branch lines could be followed up to $N = 25$ and R branch forms band head at $N = 12$. After turning, R branch rotational lines merged with lower J members and could not be clearly identified because of limited resolution. Even though, P branch lines could be observed for a few more N in the (1,0) band, they could not be identified for certainty with lower state combination differences because of band head formations in R. In the (1,0) band, a small local rotational perturbation was observed at $J' = 13.5$ of F_1 component as seen in the Table B1 of Appendix B. The (2,0) band was found to be perturbed at $15.5 \leq J \leq 21.5$ in P_1- and at $12.5 \leq J \leq 17.5$ in P_2-branch.The rotational constants were determined for both bands by fitting the above mentioned lines of P and R branches and are listed in Table 5.1. The constants in Table 5.1 were derived by fitting 60 lines ($J = 1.5$ to 16.5 in P_1, $J = 1.5$ to 15.5 in P_2, $J = 0.5$ to 14.5 in $R_1$and $J = 0.5$ to 13.5 R_2) in (1,0) (see Table B1 of Appendix B) and 59 lines ($J = 1.5$ to 14.5; 22.5-24.5 in P_1, $J = 1.5$ to 11.5; 18.5-25.5 in P_2, $J = 0.5$ to 11.5 in R_1 and $J = 0.5$ to 9.5 in R_2) in the (2,0) band (see Table B2 of Appendix B). The molecular constants for the $v'' = 0$ level of $X^2\Sigma^+$ state were fixed in the fit to the more accurate values from Cheung *et al.* [140]. The centrifugal distortion constant D_v could not determined in the present work because of its small magnitude and observations limited to low rotational levels populated in the jet-cooled source. The spin-splitting in the P branches were not found to increase linearly with N because of rotational perturbations and thus γ_v for the $B^2\Sigma^+$ state could only be estimated and not accurately determined.

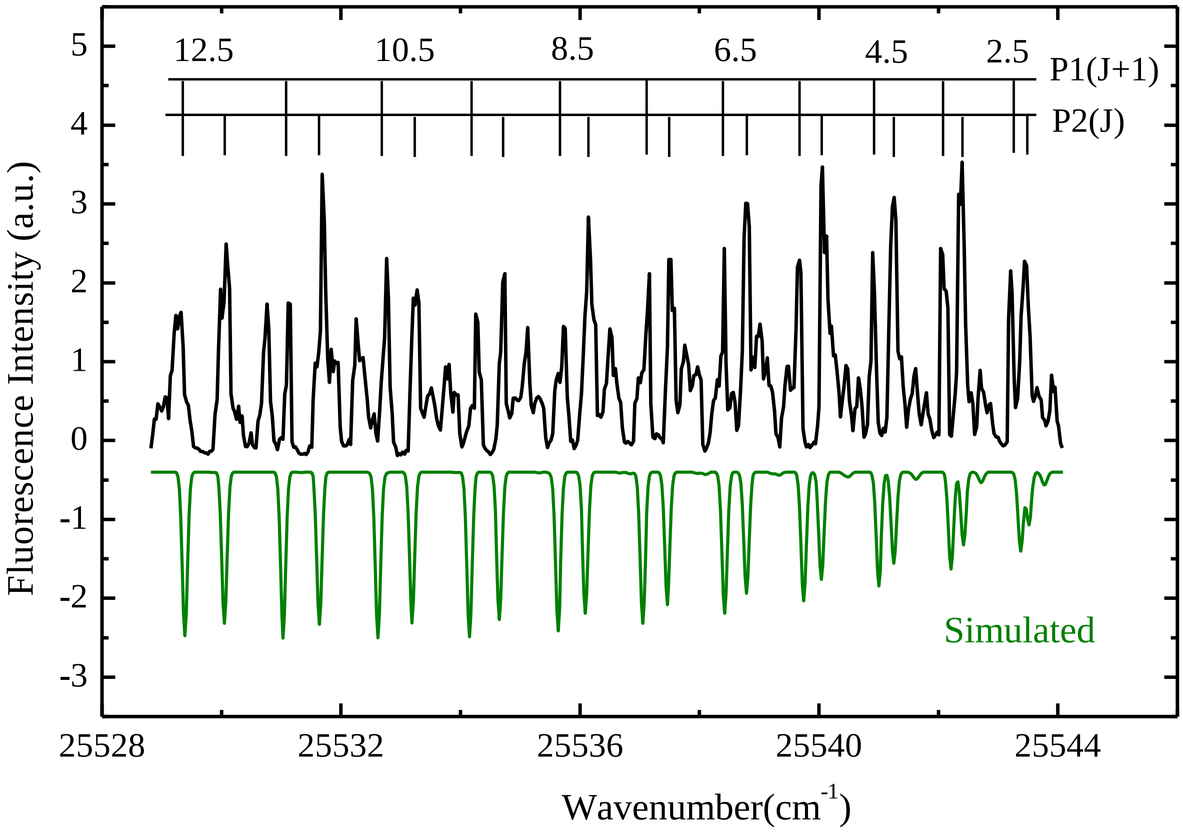

Figure 5.1. The portion of rotational structure of the (1, 0) band of $B^2\Sigma^+$–$X^2\Sigma^+$ system of jet-cooled ^{90}ZrN molecule. Inverted spectrum simulated from Pgopher program.

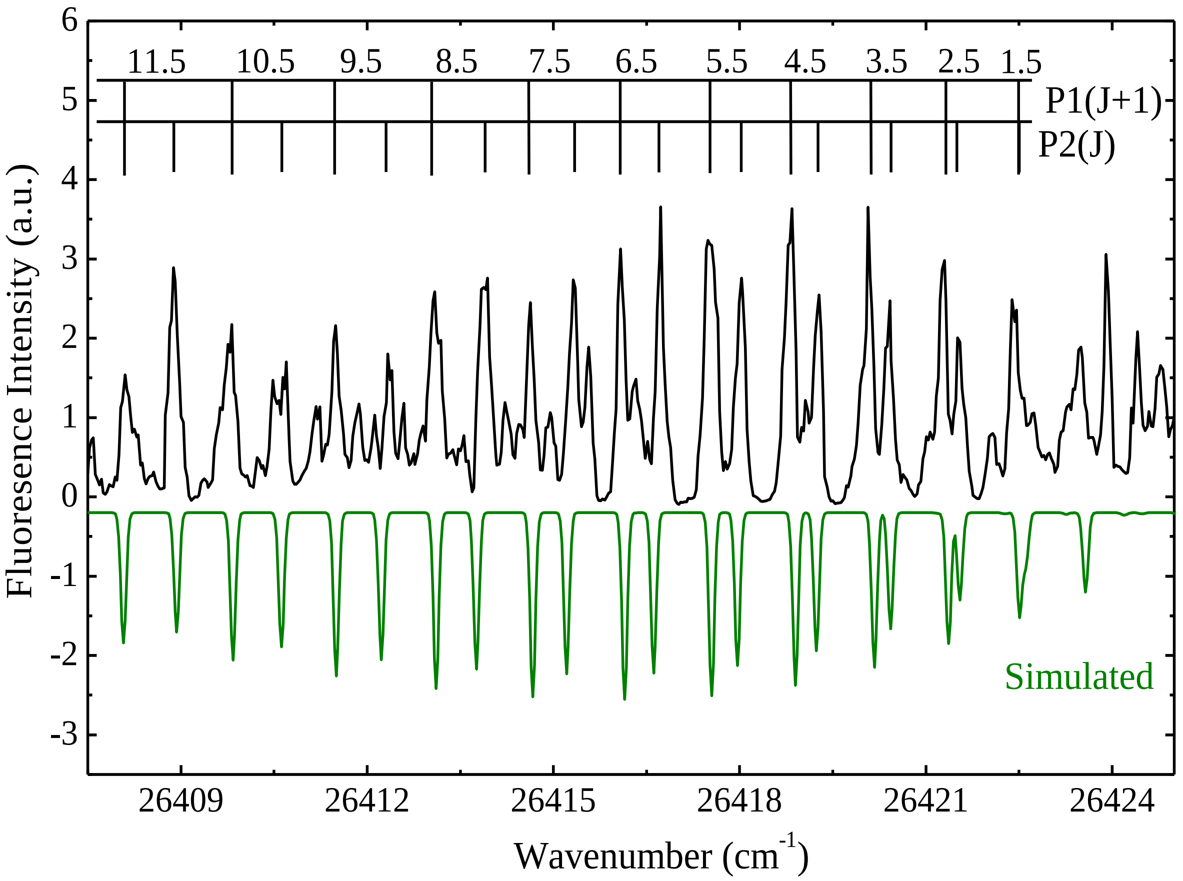

Figure 5.2. The portion of rotational structure of the (2, 0) band of $B^2\Sigma^+$–$X^2\Sigma^+$ system of jet-cooled ^{90}ZrN molecule. Inverted spectrum simulated from Pgopher program.

Table 5.1. Molecular constants (cm^{-1}) and radiative lifetimes (ns) of the $B^2\Sigma^+$ state of ^{90}ZrN.

Constants	**ν = 0**[a]	**ν = 1**	**ν = 2**
T_v	24670.60(3)[b]	25546.72(2)[c]	26424.54(1)
B_v	0.45870(8)	0.4507(2)	0.4490(1)
10^7D_v	1.7(5)	–	–
γ_v	-0.098(10)	-0.060(3)	-0.077(2)
τ	22.9(12)	23.5(10)	22.8(13)

[a] Parameters from ref [141] tabulated for completeness

[b] Typographical error in ref. [141] corrected by the corresponding author (private communication).

[c] Numbers in parentheses are one standard deviation in the last digits.

The presence of severe perturbation in the rotational spectra of (0,0) band was reported by earlier workers [176,141]. Bates and Dunn [176] reported perturbations only at the excited levels of F_2 component at high N, maximum at $N = 44$. They suggested an excited vibrational state of $A^2\Pi$ as the perturbing state. Later Chen *et al.* [141] reported perturbations at both the F_1 and F_2 component at different J values. From the shift of perturbations occurring at different J values for different isotopes in F_1, while at the same J for F_2, they concluded that at least two perturbing states were involved and suggested $A^2\Pi$ or $^4\Sigma^-$ as possible perturbing state. In a recent *ab initio* calculation, Farhat *et al.* [179] showed that the potential energy curves of a number of electronic states $(2)^2\Delta$, $(1)^2\Phi$, $(3)^2\Pi$, $(2)^2\Phi$, $(4)^2\Pi$, $(1)^4\Sigma^+$, $(2)^4\Delta$, $(1)^4\Pi$ and $(1)^4\Phi$ could cross the potential energy curve of the $B^2\Sigma^+$ (in notation of ref. 179, $(3)^2\Sigma^+$) state and listed their crossing positions. The T_e and ω_e values of their calculation shows that $\nu = 4$ of $(3)^2\Pi$, $\nu = 3$ of $(4)^2\Pi$, $\nu = 2$ of $(1)^4\Sigma^+$ and $\nu = 11$ of $(1)^4\Pi$ states are close in energy of $\nu = 0$ of $B^2\Sigma^+$ state. Two energetically close lying vibrational states belonging to two different electronic states can perturb each other if the levels lie close to the intersection of their potential energy curves [1]. To locate the intersection of potential energy curves of the above mentioned states with the $B^2\Sigma^+$ state, we reconstructed the potential energy curves of the relevant states shown in different figures in ref. [179] in a single potential energy plot and is shown in Fig.5.3. We also placed the vibrational levels of those states from the predicted ω_e values. From the Fig. 5.3, we infer that $\nu = 4$ of $(3)^2\Pi$, $\nu = 3$ of $(4)^2\Pi$ and $\nu = 2$ of $(1)^4\Sigma^+$ levels lie close to the crossing point of their respective potential energy curves and could be the potential perturbing states. The potential energy curves of $A^2\Pi$ and $B^2\Sigma^+$ states do not cross at all and thus the higher vibrational levels of $A^2\Pi$ state cannot cause any rotational perturbation in the (0,0) band as suggested in earlier reference [176]. Farhat *et al.* [179]

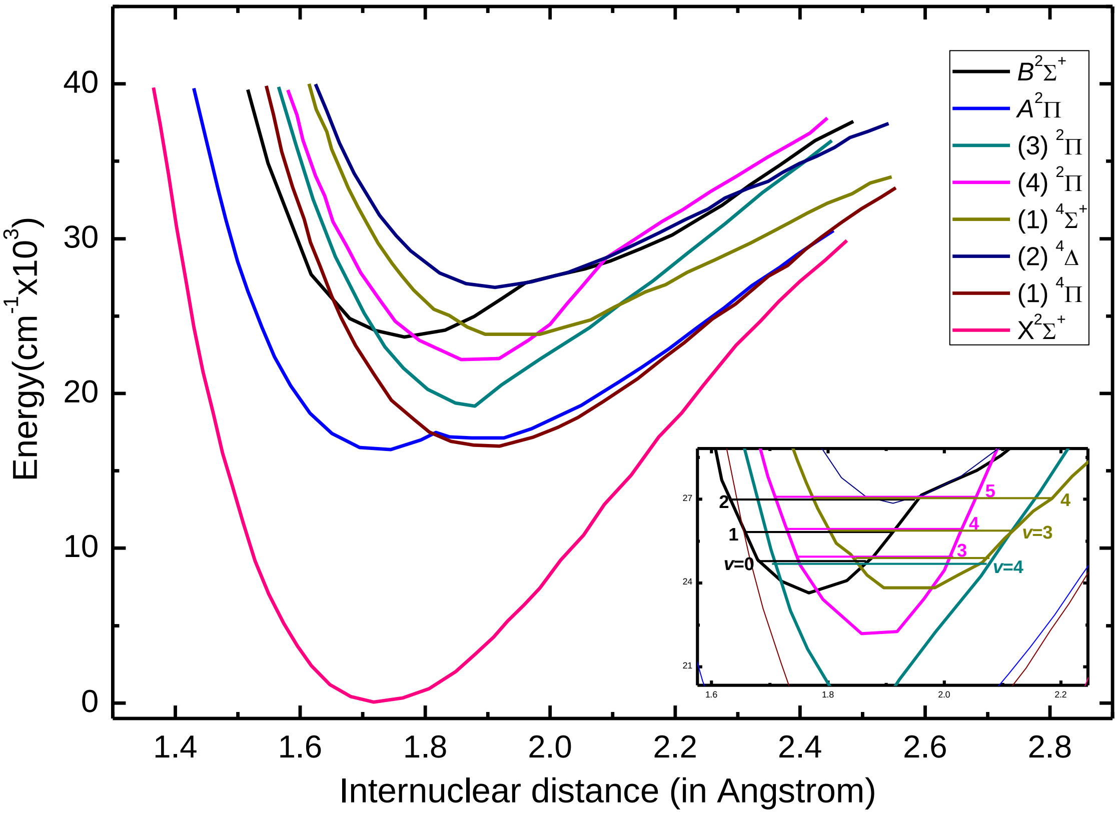

Figure 5.3. Reconstructed potential energy curves for ^{90}ZrN molecules. Vibrational levels of relevant electronic states are shown in inset figure with color code.

did not find the theoretical $^4\Sigma^-$ state at 27297 cm^{-1} reported by Chen *et al* [141]. Even though the potential energy curves of (2)$^4\Delta$ and (1)$^4\Pi$ states intersect that of $B^2\Sigma^+$ state, the interaction between them should be weak and cannot cause perturbations of this magnitude. The predicted ω_e values of (4)$^2\Pi$ and (1)$^4\Sigma^+$ states being similar with that of $B^2\Sigma^+$ state, the successive vibrational levels of these states, i.e., ν = 4 of (4)$^2\Pi$ and ν = 3 of (1)$^4\Sigma^+$ with ν = 1 of $B^2\Sigma^+$ and ν = 5 of (4)$^2\Pi$ and ν = 4 of (1)$^4\Sigma^+$ with ν = 2 of $B^2\Sigma^+$ will be close in energy and are shown in inset Fig.5.3. However, the levels being away from crossing point of their potential energy curves, a small rotational perturbation is expected in the (1,0) and (2,0) bands. The predicted ω_e = 1408.5 cm^{-1} of (3)$^2\Pi$ state brings ν = 5 energetically closer to ν = 2 of $B^2\Sigma^+$ state but again being away from the crossing point may cause a small rotational perturbation. The intersection of potential energy curves of $(1)^4\Pi$ with $B^2\Sigma^+$ state lie higher in energy compared to the relevant vibrational levels of $B^2\Sigma^+$ state and thus no perturbation is expected from this state. We observed 8-10 groups of doublet like peaks of intensity ~1/4 of the main *P*-branch appearing approximately at the middle of F_1 and F_2 component from N = 12-19 in the (2,0) band. These features could be present for N<12 also, but could not be identified from the main *P*-branches. Similarly, a few extra weak lines are observed in the *P*-branch of (1,0) band as well. But these features are not as regular and prominent as observed in the (2,0) band. However, our best efforts did not yield any result towards the identification of these peaks. In view of this, it was not possible at this stage to conclude confidently the exact nature of the perturbing states and deperturb the rotational spectra. These additional lines are listed in the Appendix B. The radiative lifetimes of the excited state $B^2\Sigma^+$ were also determined. No systematic variation in radiative lifetime of the rotational levels within different vibrational levels was observed.

The DF spectra were recorded in the wavelength region 360-900 nm by exciting a single rotational level within ν′ = 0-2 of the *B* state via various observed excitation bands of the *B*-*X* system. A typical DF spectrum from $P_2(6.5)$ rotational line of the $B^2\Sigma^+$-$X^2\Sigma^+$ (2,0) transition showing the vibrational progression up to ν″ = 0-5 of the $X^2\Sigma^+$ ground state, is shown in Fig. 5.4. The DF lines terminating to the ground state split into *PR*-doublets when either *P*- or *R*-lines were excited, the lower levels were confirmed as the vibrations of the ground electronic state. The equilibrium vibrational constants for the ground state were obtained by fitting the vibrational term values using least squares method to an anharmonic oscillator formula,

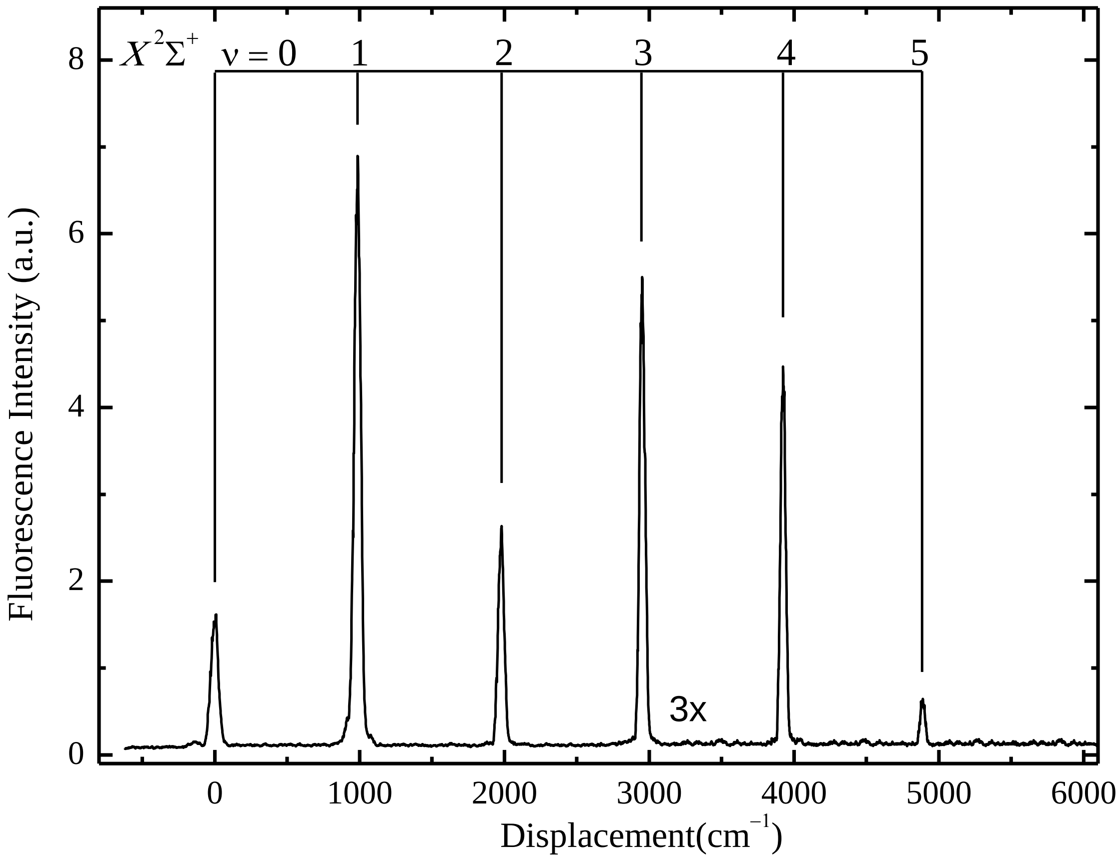

Figure 5.4. Dispersed fluorescence (DF) spectra of ^{90}ZrN observed from ν' = 2, J' = 5.5 of $B^2\Sigma^+$ state; the x-axis shows the displacement in cm^{-1} from the excitation line.

$$\Delta G = G(\nu) - G(0) = \omega_e \nu - \omega_e x_e \nu(\nu + 1), \tag{5.3}$$

where ν is a vibrational quantum number, $G(\nu)$ is term value of νth vibrational level and ω_e and $\omega_e x_e$ are harmonic and anharmonic vibrational constants. To determine ω_e and $\omega_e x_e$, term values of six vibrational levels (ν = 0-5) were included in the fit in which term values for ν = 1, 3 were taken from band origin. Previously, the equilibrium vibrational constants for $X^2\Sigma^+$ were determined from a limited set of dispersed fluorescence data ν = 0-2 [139]. The vibration term values and the equilibrium constants ω_e and $\omega_e x_e$ are listed in Table 5.2 and compared with the previous results.

Table 5.2. Term values and equilibrium vibrational constants (cm^{-1}) of the $X^2\Sigma^+$ ground state of ^{90}ZrN.

v	T_v	ω_e	$\omega_e x_e$
0	0.0	1002.5(16)[a]	4.01(30)
1	994.69(2) 995.0(9)[b]	1002.6[b]	3.8[b]
2	1980(5) 1982.4(13)[b]		
3	2961.53(3)		
4	3930(4)		
5	4891(3)		

[a] Numbers in parentheses are one standard deviation in the last digits.
[b] Ref. [139].

5.3.2 $A^2\Pi$-$X^2\Sigma^+$ system

We have observed (3,3) band of $A^2\Pi$-$X^2\Sigma^+$ system along with the previously reported [176,137,138,140] (0,0), (1,1), and (2,2) bands. The two sub-bands of $A^2\Pi$-$X^2\Sigma^+$ (3,3) transition were identified with band origins at 16988 and 17554 cm^{-1} which corresponds to $A^2\Pi_{1/2}$-$X^2\Sigma^+$ and $A^2\Pi_{3/2}$-$X^2\Sigma^+$ sub-band transitions respectively. Six branches P_2, Q_2 , R_2 and P_{21}, Q_{21} and R_{21} expected from $^2\Pi_{3/2}$ (a) -$X^2\Sigma^+$ (b) transition was identified (see Fig. 5.5). However, the branches Q_2 from P_{21} and R_2 from Q_{21} were not resolved. The branches of $^2\Pi_{3/2}$-$^2\Sigma^+$ sub-band were found to be normal and no perturbations were observed with presently employed spectral resolution of ~0.1 cm^{-1}, whereas $^2\Pi_{1/2f}$ -$^2\Sigma^+$ sub-band was found to be perturbed. In the least squares fit, B constants 0.47281(53) and 0.47489(48) cm^{-1} respectively for $\nu = 3$ of $^2\Pi_{3/2}$ and $^2\Sigma$ state and $T_3 = 20232.7(1)$ cm^{-1} were determined with A-constant fixed to 566.01 cm^{-1}. This fixed value for A-constant was determined from the difference in band origins of the two

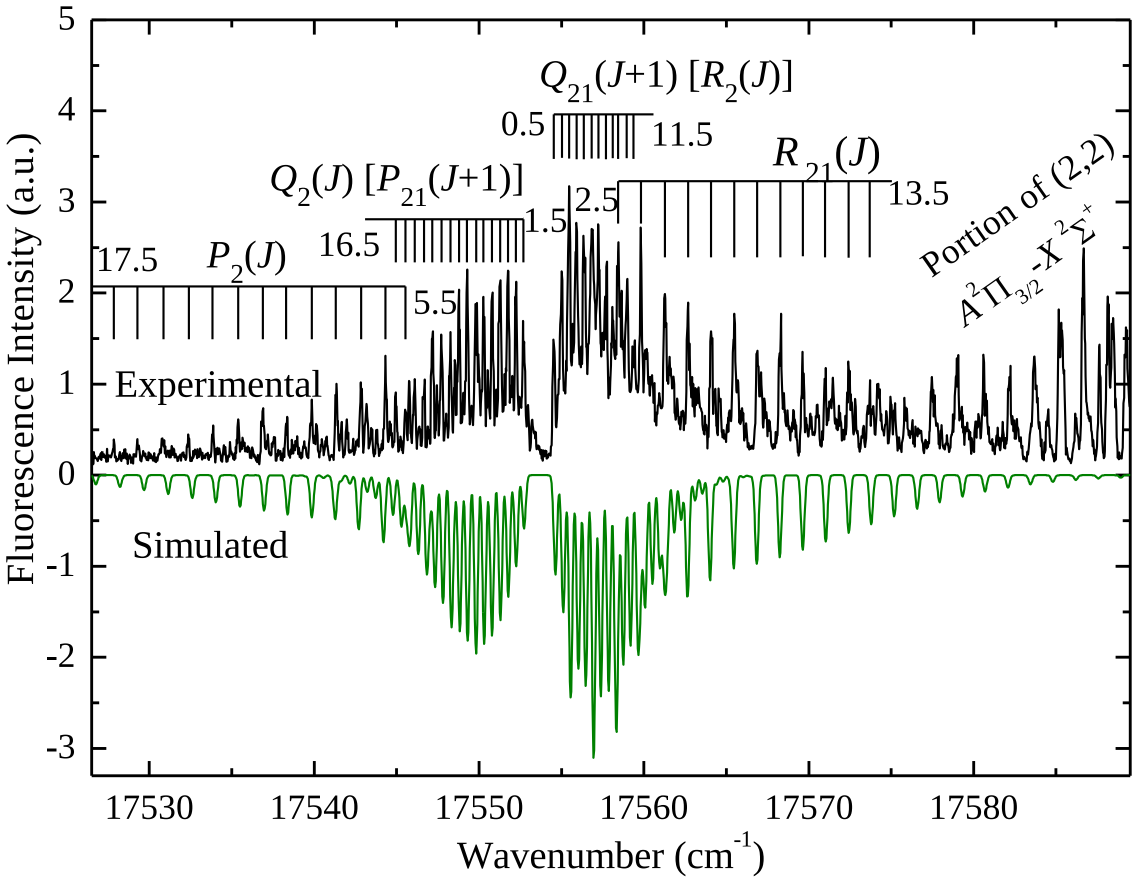

Figure 5.5. The excitation and simulated spectra of the (3,3) band of $A^2\Pi_{3/2}$-$X^2\Sigma^+$ transition.

Table 5.3. Molecular constants for ν = 3 of $X^2\Sigma^+$, $A^2\Pi_{3/2}$ and $A^2\Pi_{1/2e}$ states of ^{90}ZrN.

Constants	$X^1\Sigma^+$	$A^2\Pi_{1/2e}$	$A^2\Pi_{3/2}$
T_v	2961.53(3)[a]	20232.92(3)	20232.68(3)
A	-	566.01[b]	
B_v	0.4749(5)	0.4704(3)	0.4728(5)
10^7D_v	-	196(7)	-

[a] Numbers in parentheses are one standard deviation in the last digits.
[b] Fixed in the fit.

given in Table 5.3. The line position fitting was carried out by fitting 53 line positions of P_2 (J = 5.5-17.5), Q_2 (2.5-17.5), R_2 (0.5-11.5) and R_{21} (2.5-13.5) to an energy level sub-bands of A-X system. The molecular constants for $\nu = 3$ of $X^2\Sigma^+$, $A^2\Pi_{3/2}$ and $A^2\Pi_{1/2e}$ states are expression for a $^2\Pi$ and $^2\Sigma$ state in the Pgopher program [106]. The energy level expression for $^2\Pi$ state is,

$$T_v(N)\binom{e}{f} = T_v + A_v L.S + B_v\left[N(N+1)\right] - D_v\left[N(N+1)\right]^2 \pm \tfrac{1}{2}\left[q_v N(N+1)\right] \qquad (5.4)$$

where $N = J - 1/2$ and $N = J + 1/2$ respectively for $^2\Pi_{1/2}$ and $^2\Pi_{3/2}$ spin-orbit components of $^2\Pi$ state, B_ν and D_ν are the rotational constant and its higher-order correction, A_v is spin-orbit constant and q_v is λ-doubling constant. The meaningful value of $D_{\nu=3}$ for both the states, $\gamma_{\nu''}$ and Λ-doubling parameter $q_{\nu'}$ could not be determined in the fit.

Six branches P_1, Q_1, R_1 and P_{12}, Q_{12} and R_{12} expected from $^2\Pi_{1/2}$ (a) -$X^2\Sigma^+$ (b) transition were identified as shown in Fig.5.6. However, the branches Q_1 from R_{12} and P_1 from Q_{12} were not resolved. Since the $^2\Pi_{1/2}$ ($\nu = 3$) spin component of the excited $A^2\Pi$ state is affected by perturbation, our attempt to fit both the sub-bands of A-X (3,3) together was unsuccessful. Our attempt to fit $^2\Pi_{1/2e}$ and $^2\Pi_{1/2f}$ components of $A^2\Pi_{1/2}$- $X^2\Sigma^+$ together also did not provide satisfactory results. The e-parity levels were found to be free from perturbation and the rotational constants were determined by fitting only e levels from R_1(2.5)-R_1(19.5), P_1(1.5) [Q_{12}(0.5)]- P_1(16.5) [Q_{12}(15.5)] (see Table B6 of Appendix B). The molecular constants are listed in Table 5.3. However, a meaningful rotational analysis of f levels was not possible for the reasons explained below. The isolated rotational lines in Q_1(R_{12}) branch corresponding to the not be separated from each other and a band head like structure appeared at 16992.2 cm^{-1} (see Fig. 5.6). In the P_{12} branch, isolated lines from the f-parity levels were observed from J' = 5.5-13.5. Below J'<5.5, P_{12} lines could not be resolved from the P_1(Q_{12}) lines and an excited f-parity levels were observed from J' = 0.5-7.5. Beyond this, the rotational lines could unambiguous assignment was not possible. We could fit the above mentioned rotational lines of Q_1(R_{12})

and P_{12} together but this produced the band head position at 16992.7 cm^{-1}, which is 0.5 cm^{-1} higher in energy than the observed one. The similar values of rotational constants and simulated band head position were obtained while fitting only P_{12} lines. However, while fitting only $Q_1(R_{12})$ lines, the simulated band head appeared at 16991.6 cm^{-1} and the line positions of P_{12} were not reproduced as well. The assignments of rotational lines could not be confirmed from the lower state combination differences. In lower J, while

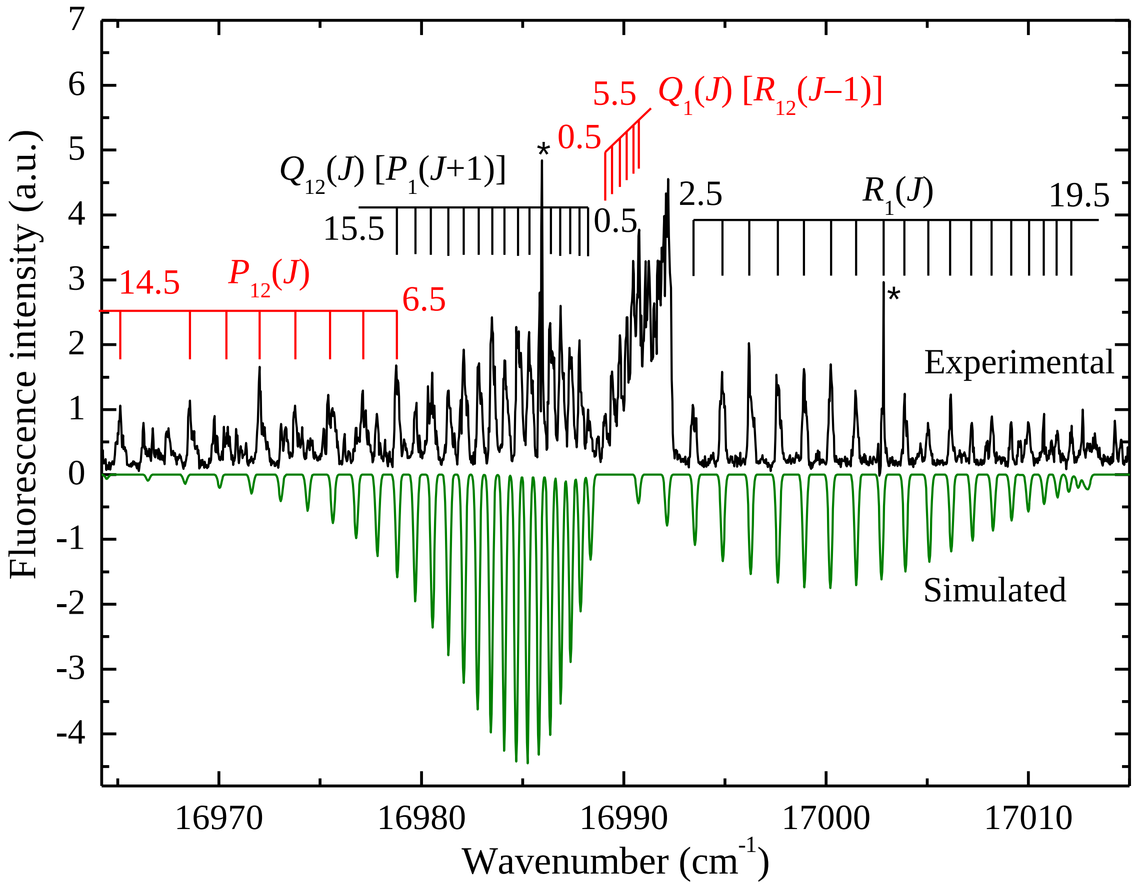

Figure 5.6. The excitation spectrum of the (3, 3) band of $A^2\Pi_{1/2}$-$X^2\Sigma^+$ transition. The simulated spectrum is shown for unperturbed $A^2\Pi_{1/2e}$-$X^2\Sigma^+$ transition. Zirconium atomic lines marked with ‘*’.

isolated $Q_1(R_{12})$ lines were observed, the corresponding P_{12} lines could not be assigned unambiguously as it was blended with the $P_1(Q_{12})$ branch lines. Similarly, in higher J, while isolated P_{12} lines were observed, the corresponding $Q_1(R_{12})$ lines could not be resolved and assigned unambiguously. In view of this, conclusive rotational analysis of $A^2\Pi_{1/2f}$ - $X^2\Sigma^+$ band was not possible. Moreover, the $Q_1(R_{12})$ band head was observed at 17009.81 cm^{-1} by Moskvitina and Kuzyako [178]. Nevertheless, the details of fit of the $A^2\Pi_{1/2f}$ - $X^2\Sigma^+$ band are included in the Appendix B. Our efforts to analyze the band head like structure (Fig.5.6) further by obtaining high resolution dispersed fluorescence (DF) spectra did not yield any result as it fluoresced back only to the excitation line. The DF obtained from different isolated rotational lines in various branches of this A-X subband also fluoresced back to the excitation line only. Our rotational analysis indicates the presence of perturbation in $A^2\Pi_{1/2f}$ - $X^2\Sigma^+$ (3,3) band. However, neither the exact location nor the nature of perturber in the excited state could be established. Severe rotational perturbations in the $A^2\Pi_{3/2}$-X subbands of (0,0), (1,1) and (2,2) of A-X system were reported by previous authors [137,138,140,176]. They suggested the perturbing states as $^2\Delta$ and $^4\Pi$. Farhat *et al.* [179] had shown that the theoretical potential energy curves of $A^2\Pi$ [(1)$^2\Pi$ in notation of Ref. [179]] has avoided crossing with the (2)$^2\Pi$ state at $r = 1.83$ Å and the crossing with the (1)$^2\Phi$. They concluded that this crossing and avoided crossing might be responsible for the experimental vibrational perturbations occurring in the spectra of the $A^2\Pi$ electronic state.

5.4 Conclusions

In revisiting ZrN, $B^2\Sigma^+$-$X^2\Sigma^+$ and $A^2\Pi$-$X^2\Sigma^+$ systems, rotational constants were obtained for $v = 1, 2$ of the $B^2\Sigma^+$ state. In view of perturbations, these rotational constants were determined by fitting a limited number of rotational lines in the P_1 and P_2 branches, and a few *R*-branch lines of (1,0) and (2,0) bands of *B*-*X* system. Earlier authors also reported perturbations in the $\nu = 0$ of $B^2\Sigma^+$ state. They proposed these perturbations could be due to $A^2\Pi$ or a $^4\Sigma^-$ state from the similarities of isoelectronic TiN molecule. However, in view of the recent theoretical work of Farhat *et al.* [179], the plausible perturbing states could be $(3)^2\Pi$, $(4)^2\Pi$ and $(1)^4\Sigma^+$. Term energies determined from the band origin data of $\nu = 1$, 3 and DF data for $\nu = 2$, 4, 5 were used to determine equilibrium vibrational constants of the ground state. In the $A^2\Pi$-$X^2\Sigma^+$ system, degenerate and non-degenerate rotational perturbations were identified at several places in the (0, 0), (1, 1) and (2, 2) bands of $A^2\Pi_{3/2}$-$X^2\Sigma^+$ system in the previous works [137,138,140,176]. The (3, 3) band of $A^2\Pi_{3/2}$-$X^2\Sigma^+$ system was found to be unperturbed in the present work and rotational constants and term energies of both states were determined. However, rotational perturbations were observed in the (3, 3) band of $A^2\Pi_{1/2f}$-$X^2\Sigma^+$ system.

Chapter 6

Radiative lifetime measurements of neutral Lanthanum (La I) atom

6.1 Introduction

The electronic structure of rare earth atoms is very complex. Large number of low-lying overlapping configurations due to the presence of open 4*f*, 5*d*, 6*s* and 6*p* shells give rise to rich and complex spectra throughout the optical region. The present work focus on the Lanthanum (La I, Z = 57) atom having $5d6s^2$, $^2D_{3/2}$ ground state electronic configuration.

6.1.1 Need for Atomic Data

The use of lanthanides in the commercial products is on the rise. Use of lanthanides can be seen in magnetic devices such as strong household magnets, as a contrast reagent in Magnetic Resonance Imaging (MRI), Cellular phones, Rechargeable batteries, CD players, Phosphor Televisions, and even in the Night vision goggles. Global rise in the conventional fuel prices along with the environmental issues are encouraging the use of alternate energy sources. Cars and other automobiles are also being operated on batteries. The many uses of lanthanides in magnetic materials are due to the unpaired *f*-shell electrons. In addition, radiative data on rare earth elements is of commercial importance due to their usage as additives in metal halide-high intensity discharge (MH-HID) lamps which provide pleasing white light with higher luminous efficacy than conventional incandescent light sources [186]. Den Hartog *et al.* [186] pointed that, transition probabilities of both the first and second spectra of the rare earths are needed by lighting industry for diagnostics and modelling of these lamps. Measurements of the radiative lifetimes of the excited atomic levels, combined with branching fractions, provide one of the most reliable, direct and efficient means of measuring large set of transition probabilities [187].

Rare-Earth (RE) elements are among the most spectroscopically accessible of the *n*-capture elements. The open *f*-shell of the RE neutral atoms and ions yields many strong lines in the visible and near-IR where spectral line blending is less of a problem than in the UV, and where ground-based observations are possible. Observations with a high signal-to-noise (S/N) ratio and a high spectral resolving power on an increasing number of stars are now available from large ground-based telescopes. The quality of these new astronomical data can be fully exploited only if similar quality basic spectroscopic data, especially data on transition probabilities, are available. The combination of improved astronomical data and improved laboratory data has reduced line-to-line and star-to-star scatter in abundance values for many RE elements. Accurate laboratory atomic data is necessary in order to correct elemental abundance discrepancies in stars, to help in resolving the anomalies in nucleosynthesis models such as the even-odd effect (where *even* atomic numbered elements appear to have higher abundances in stars than the *odd* numbered elements), to compute stellar matter opacities, and to predict abundances for element-specific emitting species within a star [188,189]. There are even some unexplained phenomena observed by astrophysicists where stellar abundances are much larger than the theoretical solar models can account for, called *chemically peculiar* (CP) stars. It is within these CP stars that lanthanides are often observed in large over-abundances [190]. Furthermore, some of the oldest stars in our galaxy found in the galactic halo of the Milky Way, the metal deficient halo stars, show increased lanthanide abundances [191,192,193].

6.1.2 Literature survey

Measurement of transition probabilities in La I were first published by Corliss and Bozman [194]. These measurements have large systematic errors, particularly for the weak transitions. Hese and co-workers in 1970 [195-197] have used level-crossing and double resonance techniques to measure radiative lifetimes of four low-lying odd-parity levels. Later Bulos *et al.* [198] have measured lifetimes for four levels, of which two were known earlier, by employing time-resolved laser-induced fluorescence (TRLIF) technique in effusive atomic beam. Lifetimes of the 12 odd-parity levels, in the range of 18000-31000 cm^{-1}, were determined by Penkin and co-workers [199] using pulsed-electron delayed coincidence technique. Lifetimes and transition probabilities for resonance transitions in La I were reviewed respectively by Blagoev and Komarovskii [200] and Doidge [201]. Recently, the work on lifetime measurements on La I levels was extended further by Biémont *et al.* [202]. They have employed TRLIF technique in laser produced lanthanum plasma to measure short lifetimes of 20 odd-parity levels and compared them with the theoretical values and found to be in fairly good agreement. Karaçoban and Özdemir [203] have calculated energies, Landé factors and lifetimes for some of the levels by multiconfiguration relativistic Hartree-Fock method. During the course of the present work Feng and co-workers [204] have published measurements on lifetimes of 32 odd parity levels up to 38000 cm^{-1} using the same experimental technique used by Biémont *et al.* [202]. From the so far published results, it appears that the lifetimes for most of the levels measured by different techniques like pulsed-electron delayed coincidence [199] and selective laser excitations [198,202,204] are consistent with each other except for the values measured by level-crossing and double resonance techniques [195-197] which appears systematically lower than all other measurements.

In spite of these efforts, there is still a need for measurement of radiative lifetime data for many levels, particularly below 18000 cm^{-1}. This present work reports radiative lifetime measurements on 63 levels of La I, including 45 for the first time, in the 13260 - 30965 cm^{-1} region using TRLIF in supersonic free-jet. Majority of the previous lifetime data in La I is from the work published [202,204] where lifetimes were measured in atomic vapor generated in laser-induced plasma. In this method, care has to be taken to measure lifetimes free from the effects like collisional depopulation and radiation trapping [205]. In the present work, we have used the technique of laser vaporization in conjunction with supersonic expansion for generating a supersonic free-jet of lanthanum atom. In supersonic free-jet, the excitation of atoms takes place in collision-free environment at a low atom number density and thus measured radiative lifetimes are free from collisional and radiation trapping effects. However, this method suffers from the disadvantage of shortening of lifetime due to flight-out-of view effect [206], generally for the longer lifetimes of the order of 1 μs.

Just after the publication of our work, Feng *et al.* [207] again published another article on lifetime measurements of 24 high-lying odd parity levels of La I in the energy range from 34213 to 40910 cm^{-1} using TFLIF spectroscopy. Very recently in 2014, Shang *et al.* [208] measured natural lifetime for 60 excited levels of La I and La II using TRLIF in laser-induced plasma. They have measured lifetimes of 40 excited levels of La I, in the energy range from 24507.87 to 52030.4 cm^{-1} and 20 levels of La II, from 26414.01 to 56035.70 cm^{-1}. The continued recent measurements of radiative lifetimes in La show the interest in the field and need for the radiative data.

6.2 Experiment

The lifetime measurements in La I are carried out in a supersonic free-jet apparatus, discussed in the Chapter 2. The essential part for producing the lanthanum metal plasma and forming translational cooled La atoms is same as given in Chapter 3. The translationally cooled La atoms are excited to a energy level of interest orthogonally to the supersonic expansion axis about 50 mm downstream of the nozzle by an excimer pumped pulse dye laser having pulse duration and bandwidth respectively of 11 ns and 0.1 cm^{-1}. Several dyes are used to cover wavelengths from 344 to 754 nm. Laser-induced fluorescence (LIF) is collected along the axis orthogonal to both the atomic and laser beams by a biconvex 50 mm *f*/1 lens and imaged on the entrance slit of the monochromator with magnification of 4 and subsequently detected by a Peltier cooled photomultiplier tube (PMT). The monochromator is used as a broad band filter. Lifetimes of levels more than 150 ns are re-measured by imaging the fluorescence spot directly on the 10 mm x 10 mm photocathode of PMT by the same fluorescence collection optics. Combinations of various optical filters are used to minimize the scattered laser and plasma emission falling on the PMT. An output signal from the photomultiplier is amplified by a 1 GHz bandwidth amplifier. A 200 MHz digital storage oscilloscope with 2 Giga samples/s sampling rate, triggered by the excitation laser with a fast photodiode is used to record the time-resolved fluorescence decay signal detected by the PMT. The decay signal is averaged for 128 shots in order to obtain a good signal-to-noise ratio before transferring it to a personal computer for further analysis.

6.3 Measurements

We have observed excitation lines of La I of reasonably good intensity originating from the ground and the low lying metastable levels up to energy 4121.5 cm^{-1} [209]. The population of La atom in these metastable states which stayed in the beam after supersonic expansion was due to thermal excitation processes in laser-induced plasma. In view of the rich spectra associated with the rare earth elements care must be taken to correctly identify the transitions associated with excited level of interest. In order to make sure that a correct level was excited; wavenumber calibration of excitation spectra to the accuracy <0.2 cm^{-1} was carried out by using Ne optogalvanic spectral lines. In addition to this the fluorescence decay channels were also observed by recording the dispersed fluorescence (DF) spectra. The transitions to be studied can thus be identified with high degree of confidence by comparing wavelength and the intensity of the excitation as well as the DF lines with spectral line list of Meggers *et al.* [104]. This way a few excitation as well as dispersed fluorescence lines which are not listed in [104] were observed and classified.

Fluorescence decay signals for lifetime determination of a level under investigation were usually recorded in more than one suitable excitation as well as decay channels. Care was taken to minimize the influence on the lifetime measurements due to various effects like flight-out-of view, radiation trapping, saturation, and collisional depopulation. The flight-out-of-view effect was investigated rigorously in the our present and previous works [210] by recording long lifetimes in the order of 300 to 400 ns at different delay time between the ablation and excitation lasers and also at lower backing pressures up to 140 kPa (1.4 bar). Longer delay time probe the slower atoms than that of those excited at short delay time and low backing pressure reduce the average atomic beam velocity. No obvious systematic variation in the lifetimes was observed with the variation in delay and the backing pressure, at least to the longest lifetime that is reported in the present work. In order to confirm, with a high degree of confidence, that long lifetimes were not affected by flight-out-of-view effect, the lifetimes of levels showing more than 150 ns were re-measured by imaging the fluorescence directly on PMT as described in section 6.2, thereby increasing the observation spot size. No systematic trend was observed for lifetime values measured with and without a monochromator and were found to be scattered randomly around a mean value. The effect of saturation and radiation trapping was also investigated by measuring the lifetimes under different intensities of the excitation laser and the number densities of La atoms. The number density of La atoms was changed by varying ablation laser intensity. The lifetime values determined for a level with the variation in excitation laser intensity and number density were also scattered randomly around a mean value. In order to avoid the error in the measurement caused due to the nonlinear response of the photomultiplier tube, the fluorescence intensity was kept low either by inserting a combination of neutral density filters in front of the entrance slit of the monochromator or by using low pulse energy from the dye laser. The collisional depopulation was insignificant in the present work as it has been carried out in the supersonic free-jet operating at a low base pressure < 10^{-7} mbar. There could be modulations in the observed fluorescence intensity due to Zeeman and hyperfine quantum beats. However, we have not observed any modulations in the fluorescence decay signal due to these effects. The large hyperfine splitting of the prevalent ^{139}La isotope (99.91%) in most of the excited states [211] compared to the spread in the frequency ($1/\Delta\tau$) corresponding to the duration of the excitation pulse ($\Delta\tau = 11$ ns) used in this work could be the reason for not exhibiting the modulations in the fluorescence decay signal [212]. In the present work lifetimes in the range 9.5 to 313 ns have been determined. For levels that have lifetimes longer than 80 ns, lifetimes were evaluated using a least-squares exponential fitting procedure to the recorded fluorescence decay curve. Initial part of the acquired decay curve of about 20 to 30 ns was not considered for exponential fitting in order to avoid the influence of exciting laser pulse. A typical time-resolved fluorescence decay curve along with the exponential fit which yielded a lifetime value of 224.5 ns for the 13631.04 cm^{-1} level is shown in Fig. 6.1. For short-lived excited states, lifetimes were evaluated by fitting the observed fluorescence decay curve with a convolution between a Gaussian function which represented the detected excitation laser pulse very closely and an exponential function with adjustable parameters. The temporal shape of the excitation laser pulse was recorded with the same photomultiplier tube by observing the scattered light from the laser pulse. A typical time resolved fluorescence

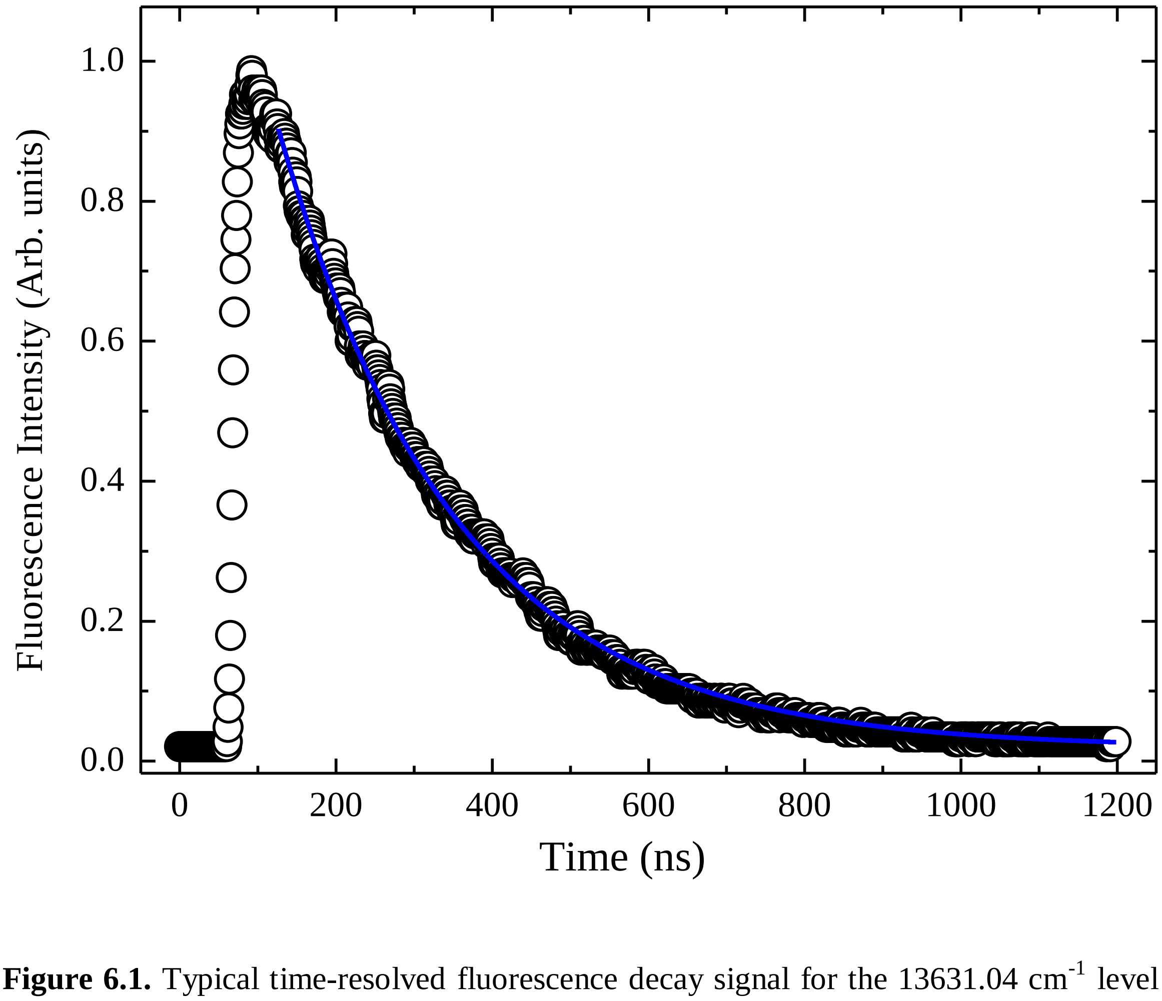

Figure 6.1. Typical time-resolved fluorescence decay signal for the 13631.04 cm^{-1} level (circles). The solid curve represents an exponential fit that gave a lifetime value of 224.5 ns.

decay curve along with the excitation laser pulse and the convolution of Gaussian function fitted to excitation laser pulse with exponential function which gave a lifetime value of 17.0 ns for the 20018.99 cm^{-1} level is shown in Fig. 6.2.

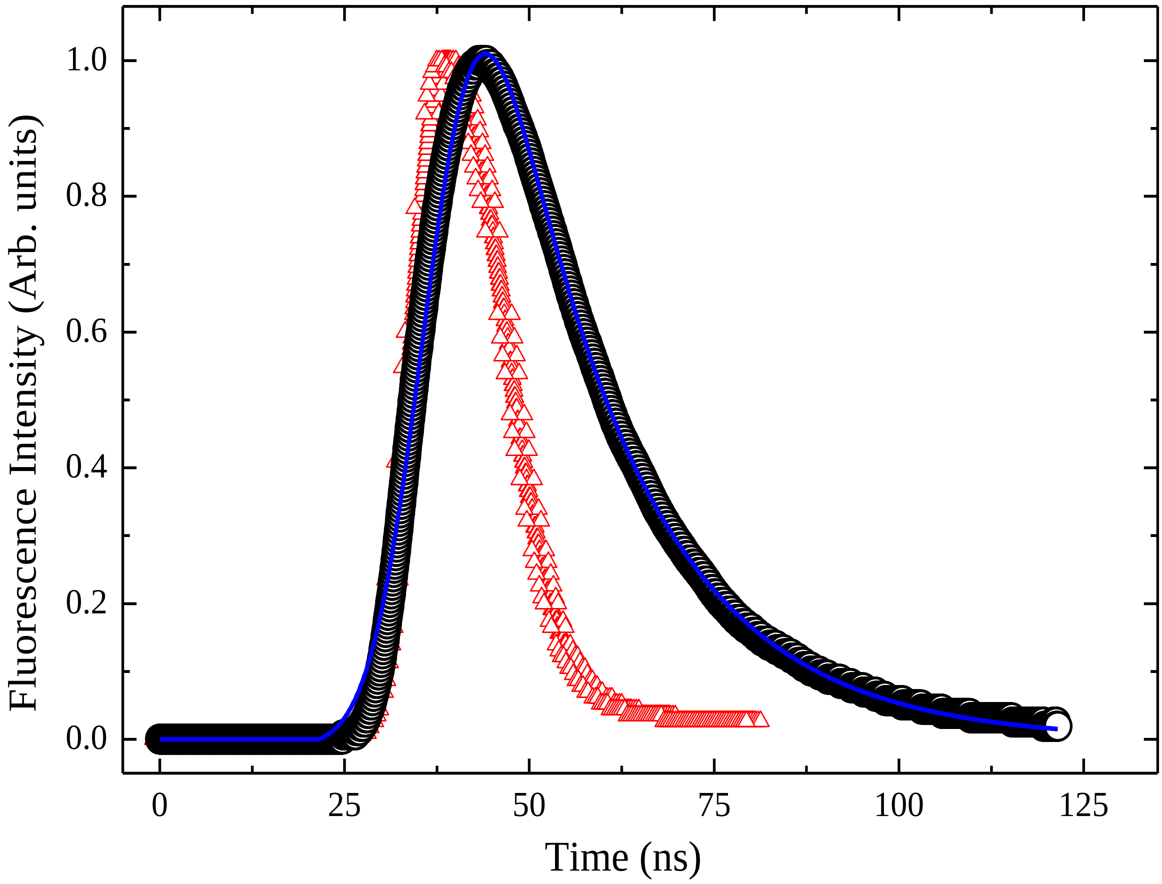

Figure. 6.2. Typical time-resolved fluorescence decay signal for the 20018.99 cm^{-1} level (circles). Triangles show recorded excitation laser pulse and the solid curve represents the convolution fit of the laser pulse and exponential decay function that gave a lifetime value of 17.0 ns.

The following expressions were used for the deconvolution fit, Exponential function $$y_{exp} = exp - \left(\frac{t-t'}{\tau}\right) \qquad (6.1)$$

Excitation laser pulse, $$y_{gauss} = y_0 + \frac{A}{w\sqrt{\pi/2}}\, exp - 2\left(\frac{t-t'}{w}\right)^2 \qquad (6.2)$$

Convoluted decay curve = $$y_{exp} * y_{gauss} \qquad (6.3)$$

The reported lifetime of a level is an average of about 10 lifetime values measured under different experimental conditions. These lifetimes were measured at different excitation and ablation laser intensities as well as delay times. Lifetimes were also recorded in more than one decay as well as excitation channels, if they are strong.

6.4 Results and Discussion

The results of the radiative lifetime measurements, with estimated uncertainties, for 63 odd-parity levels of La I in the energy range 13260 - 30965 cm^{-1} are presented in Table 6.1. The quoted uncertainty in a reported lifetime is one standard deviation of the average lifetime value from about 10 measurements. The reported uncertainties include both statistical error and an error due to possible systematic effects. The lifetimes reported in the present work are accurate to ±10%. A comparison of lifetimes determined in this work with the earlier reported theoretical as well as experimental values is also presented. In this work lifetimes of 63 levels have been reported. Out of these to the best of our knowledge lifetimes of 45 levels have been reported for the first time. An agreement, within an experimental error, is observed when comparing our experimental results with previously reported data except for the 16538.39, 17947.13, 20197.34, 24088.54, and 25453.95 cm^{-1} levels. The lifetimes for the 20197.34 and 25453.95 cm^{-1} levels were determined by Penkin *et al.* [199] utilizing the delayed coincidence method with nonselective electron excitation. However, lifetime for the level at 16538.39 cm^{-1} was reported by Hese *et al.* [195,196] by level- crossing and double resonance techniques. Previously reported lifetime values for these three levels are 35 to 40% lower than our values. A comparison of experimental lifetime data reported by different techniques shows that most of the lifetime measurements of Hese *et al.* [195-197] and a few of Penkin *et al.* [199] are systematically lower than selective laser excitation measurements [198,202,204], including the present work (see Table 6.1) and is indicated also by Biémont *et al.* [202]. The lifetime reported for 17947.13 cm^{-1} by Bulos *et al.* [198] is shorter by 25% than our value. The probable reason for this discrepancy could be just two number of measurements for this level by Bulos *et al.* [198]. However, we have made total eleven measurements which include three excitations and four disperse fluorescence channels. The lifetime for 24088.54 cm^{-1} level, reported by Feng *et al.* [204], is longer than our value by 19%. Feng *et al.* [204] have carried out measurements in laser ablation plasma where atom density in metastable states is expected to be higher than that in our experiment where collisional depopulation of metastable states occurs just before supersonic expansion. The plausible reason for higher lifetime reported in [204] for 24088.54 cm^{-1} level than ours could be due to the radiation trapping effects because of the high atom number density in the metastable level at 1053.164 cm^{-1} [209] from where the excitation was carried out. Recently Shang *et al*. [208] re-measured the lifetime values for 24507.87 and 25997.17 cm^{-1} levels and are in good agreement with our values as shown in Table 6.1.

Table 6.1. Radiative lifetimes for 63 odd-parity levels of La I.

configuration^a	Term^a	J^a	Energy^a (cm^{-1})	λ_{exc}^{b} (nm)	λ_{obs}^{b} (nm)	Lifetime (ns)			
						Theory		Experimental	
						Ref.[202]^c	Ref.[203]^d	This work	Previous work
5d6s(^{3}D)6p	^{4}F^o	3/2	13260.38	753.923	753.9		301.5	256.9 (123)	
5d6s(^{3}D)6p	^{4}F^o	5/2	14804.08	675.304	675.3,727.0,823.8^e		770.68	257.9(215)	
				727.030	675.3				
5d6s(^{3}D)6p	^{4}F^o	7/2	15019.51	715.808	715.8,832.4^e		794.09	313.0 (178)	
5d6s(^{3}D)6p		5/2	13631.04	733.418	733.4,794.8^e			224.5(138)	
5d6s(^{3}D)6p	^{4}D^o	1/2	14095.69	709.243^e	874.8		295.18	220.9(143)	
5d6s(^{3}D)6p	^{4}D^o	3/2	14708.92	679.673	679.6,732.0		330.63	166.3(93)	
				732.091	679.6				
5d6s(^{3}D)6p	^{4}D^o	5/2	15503.64	691.830	691.8,644.8^e		196.80	131.8(68)	
5d6s(^{3}D)6p	^{4}D^o	7/2	16099.29	664.441	664.4		270.92	156.7(142)	
5d6s(^{3}D)6p		3/2	15031.64	665.081	665.0, 715.2^e			183.7(128)	165.0(80)^f
4f6s^2	^{2}F^o	5/2	15196.83	657.851	657.8, 706.8			127.0(70)	98.0(60)^g, 120.0(60)^f
4f6s^2	^{2}F^o	7/2	16538.39	645.599	645.5, 766.4			112.9(95)	74.0(70)^g
5d6s(^{3}D)6p		1/2	15219.89	656.856^e	656.8,796.4			205.4(169)	
6s^{2}6p		3/2	16280.26	656.544	656.5, 734.4^e			271.6(192)	
5d^2(^{3}F)6p		5/2	16856.80	632.591	704.5			68.4(51)	
				593.068	632.5, 704.5				

configuration[a]	Term[a]	J[a]	Energy[a] (cm^{-1})	λ_{exc}[b] (nm)	λ_{obs}[b] (nm)	Lifetime(ns)			
						Theory		Experimental	
						Ref.[202][c]	Ref.[203][d]	This work	Previous work
5d6s(^{3}D)6p	$^4P^o$	3/2	17797.29	660.798[e]	660.7[e]		218.88	130.3(115)	
5d6s(^{3}D)6p	$^4P^o$	5/2	18156.97	550.600	645.4		59.60	68.4(31)	
				660.017	645.4				
5d^2(^{3}F)6p		7/2	17910.17	670.950	593.0			64.6(27)	
5d^2(^{3}F)6p	$^4G^o$	5/2	17947.13	591.763	654.3		39.68	68.3(31)	51.0(40)
				654.316	669.2				
				557.038	654.3, 691.7				
5d^2(^{3}F)6p	$^4G^o$	7/2	18603.92	569.619	641.0, 661.6		44.89	54.8(35)	
5d^2(^{3}F)6p	$^4G^o$	9/2	19129.31	639.423	639.4, 666.1		32.37	46.0(26)	
5d^2(^{3}F)6p	$^4G^o$	11/2	20117.38	624.993	624.9		36.56	32.0(22)	
5d^2(^{3}F)6p	$^2D^o$	5/2	19379.40	515.869	598.2, 610.7	13.21	21.56	15.9(10)	17.2(10)[h], 15.2(9)[g], 16.0(15)[i]
5d6s(^{1}D)6p		3/2	20018.99	499.388	527.1			17.0(8)	
				576.184	576.1, 527.1				
5d^2(^{3}F)6p	$^4F^o$	3/2	20082.98	497.795	525.3		17.05	17.5(16)	
				574.066	574.0, 525.3				
5d^2(^{3}F)6p	$^4F^o$	5/2	20338.25	565.772	576.9		21.66	20.0(9)	
				576.934	565.7				
5d^2(^{3}F)6p	$^4F^o$	7/2	20763.21	563.122	600.7		22.23	25.8(14)	
				578.924	578.9, 563.1				

configuration[a]	Term[a]	J[a]	Energy[a] (cm^{-1})	λ_{exc}[b] (nm)	λ_{obs}[b] (nm)	Lifetime(ns)			
						Theory		Experimental	
						Ref.[202][c]	Ref.[203][d]	This work	Previous work
$5d^2(^3F)6p$	$^4F^o$	9/2	21384.00	579.134	579.1, 558.8		19.18	23.0(21)	
				558.834	579.1				
$5d6s(^1D)6p$		1/2	20197.34	494.977	494.9, 570.3[e]			17.2(8)	11.0(6)[i]
$5d^2(^3F)6p$		5/2	20972.17	572.002	476.6		62.28	35.0(35)	
				556.572	556.5				
$5d^2(^3F)6p$		7/2	21447.86	490.187	556.8, 490.1		41.55	34.1(33)	
$5d^2(^3F)6p$	$^2G^o$	7/2	21662.51	485.082	485.0, 550.2		40.81	39.8(21)	
$5d^2(^3F)6p$	$^4D^o$	1/2	22246.64	510.623	510.6	9.11	9.40	9.1(6)	10.1(9)[h]
$5d^2(^3F)6p$	$^4D^o$	3/2	22439.36	505.646	514.5, 445.5[e]	9.39	10.31	9.5(7)	10.2(5)[h]
$5d^2(^3F)6p$	$^4D^o$	5/2	22804.25	505.057	517.7, 459.6[e], 496.4[e]	9.79	9.07	10.4(3)	10.7(10)[h]
$5d^2(^3F)6p$	$^4D^o$	7/2	23303.26	504.688	449.3, 521.1	10.32	9.20	16.5(11)	16.1(10)[h]
$5d6s(^3D)6p$		7/2	23221.10	506.790	523.4			27.5(27)	22.0(14)[h]
				523.427	506.7				
$5d^2(^3P)6p$	$^2S^o$	1/2	23260.92	429.788e	623.6,738.2			18.1(15)	
$4f5d(^1G^\circ)6s$	$^2G^o$	9/2	23466.84	516.779	516.7			67.9(38)	
$5d^2(^3P)6p$	$^4D^o$	1/2	23528.45	424.902[e]	424.9[e],479.2[e],613.4		20.97	27.8(18)	
$5d^2(^3P)6p$	$^4D^o$	3/2	23704.81	421.740[e]	421.7[e],441.3[e],475.2[e]		20.74	31.2(25)	

configuration[a]	**Term**[a]	**J**[a]	**Energy**[a] **(cm^{-1})**	**λ_{exc}**[b] **(nm)**	**λ_{obs}**[b] **(nm)**	**Lifetime(ns)**			
						Theory		**Experimental**	
						Ref.[202][c]	**Ref.[203]**[d]	**This work**	**Previous work**
5d^2(^{3}P)6p	^{4}D^o	5/2	24046.10	415.752	415.7,467.6[e]		17.37	16.1(10)	
4f5d(^{3}H^o)6s	^{4}H^o	7/2	24088.54	433.997[e]	433.9[e],485.4[e]		341.18	207.5(145)	247.0(120)[j]
4f5d(^{3}F^o)6s	^{4}F^o	3/2	24173.83	464.865	464.8,472.3[e]		6.04	37.7(14)	
4f5d(^{3}F$^\circ$)6s	^{4}F^o	5/2	24507.87	407.918	407.9	13.44	6.24	22.2(1.9)	21.9(10)[h], 14.5(15)[i], 19.2(15)[j], 20.0(8)[k]
4f5d(^{3}F^o)6s	^{4}F^o	9/2	25997.17	444.271[e] 457.002	457.0 444.2[e]		7.11	21.8(9)	21.6(10)[k]
5d^2(^{3}P)6p?	^{2}D^o?	3/2	24762.60	403.721	403.7		13.73	12.4(11)	12.5(15)[i]
4f5d(^{1}D^o)6s?		3/2	24910.38	449.471	449.4,573.9[e],565.4			32.4(18)	
5d^2(^{3}P)6p?		5/2	24984.29	465.208 417.748	400.1[e] 454.9,465.2			27.2(19)	
5d^2(^{3}P)6p		5/2	25218.27	413.704	413.7			15.7(11)	
5d6s(^{3}D)6p		1/2	25453.95	392.756	392.7			19.4(8)	11.0(10)[i]
5d^2(^{3}P)6p	^{4}P^o	3/2	25643.00	389.860	389.8, 406.5		14.66	16.2(8)	
4f5d(^{3}G^o)6s	^{4}G^o	5/2	27022.62	410.487	410.4,416.3[e]		4.77	20.9(13)	18.9(14)[j]
4f5d(^{3}G$^\circ$)6s	^{4}G^o	9/2	28089.17	406.479	406.4		10.93	21.8(18)	
4f5d(^{3}G$^\circ$)6s	^{4}G^o	11/2	28743.24	406.033	406.0		1.36	23.8(16)	
5d^2(^{3}P)6p	^{2}P^o	1/2	27748.97	360.276[e]	398.6[e],487.2[e],493.5[e]		13.73	27.0(26)	

configuration^{a}	**Term**^{a}	**J**^{a}	**Energy**^{a} **(cm**$^{-1}$**)**	λ_{exc}^{b} **(nm)**	λ_{obs}^{b} **(nm)**	**Lifetime(ns)**			
						Theory		**Experimental**	
						Ref.[202]^{c}	**Ref.[203]**^{d}	**This work**	**Previous work**
4f5d(^{3}D^{o})6s		3/2	27968.54	357.443 371.434^{e}	400.5^{e},395.1^{e} 400.5^{e}			9.5(9)	8.5(5)^{i}
4f5d(^{3}D^{o})6s	^{4}D^{o}	1/2	28893.51	346.004^{e}	381.2^{e},461.5		1.22	20.0(17)	
4f5d(^{3}D^{o})6s		3/2	28971.84	345.069^{e} 358.086^{e}	380.0^{e},,459.8^{e} 459.8^{e}		1.21	17.2(12)	
		7/2	29466.67	351.849^{e}	458.9^{e}			28.3(9)	
		5/2	30788.45	355.519^{e}	429.1^{e},447.4^{e}			14.4(12)	
4f5d(^{3}P^{o})6s	^{4}P^{o}	5/2	30896.84	354.153^{e}	427.1^{e},460.4^{e}			18.6(17)	
		7/2	30964.71	357.624^{e}	475.0^{e}			11.9(6)	11.5(10)^{i}

[a] Level energies and assignments are from Martin *et al.* [209]. The ordering of levels follows Martin *et al.* The levels assigned to the same term within same configuration are grouped and terms or unassigned levels are ordered by increasing energy.; [b] Wavelengths in air from Meggers *at al*. [104] except those marked with superscript “e”.; [c] Relativistic Hartree-Fock calculations by Biemont *et al.* [202].; [d] Multiconfiguration Hatree-Fock calculations by Karaçoban and Özdemir [203].; [e] Transition wavelengths in air not listed in Meggers *at al*.[104]. Computed from energies of levels involved in the transitions, confirmed by dispersed fluorescence.; [f] Time-resolved laser-induced fluorescence (TRLIF) measurements by Bulos *al al*. [198].; [g] Level-crossing and double resonance mesurements by Hese *et al.* [195,196,197].; [h] TRLIF measurements by Biemont *et al.* [202].; [i] Pulsed-electron delayed coincidence measurements by Penkin *et al.* [199].; [j] TRLIF measurements by Feng *el al.* [204].; [k] TRLIF measurements by Shang *et al.*[208].

6.5 Conclusions

This chapter provided radiative lifetime data, accurate within ±10%, for 63 odd-parity levels belonging to the odd 5*d*6*s*6*p*, $4f6s^2$, $6s^26p$, $5d^26p$, 4*f*5*d*6*s* electronic configurations in La I in the energy range 13260 - 30965 cm^{-1} was obtained using time-resolved laser-induced fluorescence in supersonic free-jet. The measured lifetime values fall in the range 9.5 to 313 ns. To the best of our knowledge, lifetimes for the 45 levels among the obtained results were reported for the first time. With few exceptions, reasonable agreement within experimental errors was observed between the present and the earlier reported lifetimes. To the best of our knowledge, there is no published experimental data on branching fraction for La I except the tabulation of relative spectral line intensities in the wavelength region 218 - 884 nm [104]. Transition probabilities of the several spectral lines can be calculated by evaluating branching ratios using the data of relative intensities and the lifetimes reported in the present work. Transition probability data is useful for determination of elemental abundances in stellar atmosphere, validating the atomic structure calculations and also for understanding of the radiative properties of La I needed for few applications like that in the lighting industry.

References:

---

[1] G. Herzberg, Molecular Spectra and Molecular Structure, I. Spectra o f Diatomic Molecules, 2nd Edition, D. Van Nostrand, New York, 1950.

[2] H.Lefebvre-Brion, R.W.Field, The spectra and Dynamics of Diatomic Molecules, revised and enlarged edition, Elsevier Academic Press, New York, 2004.

[3] J.Brown, A.Carrington, Rotational Spectroscopy of Diatomic Molecules, Cambridge University Press, United Kingdom, 2003.

[4] I.Kovacs, Rotational Spectroscopy in the spectra of Diatomic Molecules Elsevier Publishing, New York, 1969.

[5] P. F. Bernath, Spectra of Atoms and Molecules, Oxford University Press, New York, 2nd edition, 2005.

[6] N. Koga and K. Morokuma, Chem. Rev. **91**, 823 (1991).

[7] A. Veillard, Chem. Rev. **91**, 743 (1991).

[8] W. A. Brown, R. Kose and D. A. King, J. Mol. Catal. A **141**, 21 (1999).

[9] W. Weltner, Jr., Science **155**, 155 (1967).

[10] A.J. Merer, Annu.Rev. Phys. Chem. **40**, 407 (1989).

[11] M. Fioroni, Phys. Chem. Chem. Phys. **16**, 24312 (2014).

[12] J. Tennyson and S. N. Yurchenko, Proceedings of the International Astronomical Union / Volume 9 / Symposium S297 / May 2013 pp 330-338. doi: 10.1017/S1743921313016074; http://www.exomol.com.

[13] P.G. Wilkinson, Astrophys. J. **138**,778 (1963).

[14] N. M. White and R. F. Wing, Astrophys. J. **222**, 209 (1978).

[15] D. L. Lambert and E. A. Mallia, Mon. Not. R. Astron. Soc. London **151**, 437 (1971).

[16] O. Engvold, H. Wohl, and J. W. Brault, Astron. Astrophys. Supp. Series **42**, 209 (1980).

---

[17] B. Viswanathan, R. Shanmugavel, S.P. Bagare, N. Rajamanickam, and P. Sriramachandran, Solar Physics **257**, 261 (2009).

[18] A. Burrows, R.S. Ram, Peter Bernath, C.M. Sharp, and J.A. Milsom, Astrophys. J. **577**, 986 (2002).

[19] Y.V. Pavlenko, Astronomy Reports, **43**, 748 (1999).

[20] P.K. Carroll, P. McCormack, and S. O'Connor, Astrophys. J. **208**, 903 (1976).

[21] S. Wende, A. Reiners, A. Seifahrt, and P. F. Bernath, Astron. Astrophys. **523** A58 (2010).

[22] R. Yerle, Astron. Astrophys. **73**, 346 (1979).

[23] A. Burrows, M. Dulick, C. W. Bauschlicher, Jr., P. F. Bernath, R. S. Ram, C. M. Sharp, and J. A. Milsom, Astrophys. J. **624** 988 (2005).

[24] M.R.A. Blomberg, P. E. M. Siegbahn, and M. Svensson, Inorg. Chem. **32**, 4218 (1993).

[25] A. C. Tsipis, J. Chem. Soc., Faraday Trans. **94**, 11 (1998).

[26] G.J. Leigh, Science **279**, 506 (1998).

[27] Y. Nishibayashi, S. Iwai, M. Hidai, Science **279**, 540 (1998).

[28] F. A. Cotton and G. Wilkinson, Advanced Inorganic Chemistry, 5th Edition, John Wiley & Sons, New York, 1988.

[29] N.N. Greenwood and A. Eamshaw, The Chemistry of the Elements, 2nd Edition, Butterworth-Heinemann, Boston, 1997.

[30] A. Vojvodic, A.J. Medford, F. Studt, F.A. Pedersen, T.S. Khan, T. Bligaard and J.K. Nørskov, Chem. Phys. Lett., **598**, 108 (2014).

[31] J.F. Harrison, Chem. Rev. **100**, 679 (2000).

[32] M. D. Morse, Chem. Rev. **86**, 1049 (1986).

[33] K. Balasubramanian, J. Phys. Chem. **93**, 6585 (1989).

[34] R. E. Smalley, L. W. Wharton, and D. H. Levy, Accounts of Chemical Research **10**, 139 (1977).

[35] M. D. Morse, Methods of Experimental Physics: Atomic, Molecular, and Optical Physics, Vol. II Atoms and Molecules, edited by F. B. Dunning and R. Hulet (Academic Press, Inc., Orlando, Florida, 1996), pp. 21-47.

[36] B. Simard, P. A. Hackett, and W. J. Balfour, Chem. Phys. Lett. **230**, 103 (1994).

[37] S.G. Nakhate, and S. Mukund, Chem. Phys. Lett. **496**, 243 (2010).

[38] S. Mukund, and S.G. Nakhate, Chem. Phys. Lett. **501**, 221 (2011).

[39] S. Mukund, S. Yarlagadda, S. Bhattacharyya and S.G. Nakhate, J. Quant. Spectrosc. Radiat. Transfer**.** **113**, 2004 (2012).

[40] S. Mukund , S. Bhattacharyya and S.G. Nakhate, J. Quant. Spectrosc. Radiat. Transfer**.** **147**, 274 (2014).

[41] S. Mukund, S. Yarlagadda, S. Bhattacharyya and S.G. Nakhate, Chem. Phys. Lett. **591**, 43 (2014).

[42] L. Lodi and J. Tennyson, J. Phys. B: At. Mol. Opt. Phys. **43**, 133001 (2010).

[43] M. Born and J. R. Oppenheimer, Ann. Phys. **84**, 457 (1927).

[44] J.L. Dunham, Phys. Rev. **41,** 721 (1932).

[45] P.M. Morse, Phys. Rev. **34,** 57 (1929).

[46] J. L. Dunham, Phys. Rev. **41**, 713 (1932).

[47] J.M. Brown, E.A. Colbourn, J.K.G. Watson and R.D. Wayne, J. Mol. Spectrosc. **74**, 294 (1979).

[48] J.M. Brown, and A.J. Merer, J. Mol. Spectrosc. **74**, 488 (1979).

[49] J.M. Brown, A.S.C. Cheung and A.J. Merer, J. Mol. Spectrosc. **124**, 464 (1987).

[50] A.S.C. Cheung, A.W. Taylor, and A.J. Merer. J. Mol. Spectrosc. **92**, 391 (1982).

[51] F. Hund, Handbuch der Physik **24**, 561 (1933).

---

[52] P. F. Bernath, Spectra of Atoms and Molecules, Oxford University Press, Oxford, 1995.

[53] I. Kopp and J. T. Hougen, Can. J. Phys. **45**, 2581 (1967).

[54] C. Linton, M. Dulick, R.W. Field and P. Caratte, J. Mol. Spectrosc. **102**, 441 (1983).

[55] H. Lefebvre-Brion and R. W. Field, Perturbations in the Spectra of Diatomic Molecules, Academic Press, New York, 1986.

[56] A. Lagerqvist, R. Scullman, ArkivFys. **32**, 479 (1966).

[57] P.R. Scott, W.G. Richards, J. Phys. B **7,** 1679 (1974).

[58] A. Bernard and R. Bacis, Can. J. Phys. **55**, 1322 (1977).

[59] R. Bacis, A. Bernard, and A. Zgainsky, C. R. Acad. Sci. B **280**, 77 (1975).

[60] A. Bernard, C. Effantin, and R. Bacis, Can. J. Phys. **55**, 1654 (1977).

[61] B. Simard, W. J. Balfour, H. Niki, and P. A. Hackett, “45th Ohio State University International Symposium on Molecular Spectroscopy,” Columbus, Ohio, 1990, Abstracts RC11 and RC12.

[62] S. R. Langhoff, L. G. M. Pettersson, C. W. Bauschlicher, and H. Partridge, J. Chem. Phys. **86,** 268 (1987).

[63] K. Balasubramanian and J. Z.Wang, J. Mol. Spectrosc. **133,** 82 (1989).

[64] T. G. Dietz, M. A. Duncan, D. E. Powers, and R. E. Smalley, J. Chem. Phys. **74,** 6511 (1981).

[65] B. Simard, S. A. Mitchell, L. M. Hendel and P. A. Hackett Faraday Discuss. Chem. Soc. **86**, 163 (1988).

[66] M.A. Duncan, Rev. Sci. Instrum**. 83**, 041101 (2012).

[67] H.W Kroto, J.R.Health, S.C.O’Brien, R.F.Curl, and R.E.Smalley, Nature **318,** 162 (1985).

[68] S.G. Nakhate, BARC Report No. BARC/2004/E/033 (2004).

[69] J.B. Hopkins, P.R.R. Langridge-Smith, M.D. Morse, and R.E. Smalley, J. Chem. Phys. **78,** 1627 (1983).

[70] D.Proch and T.Trickl, Rev. Sci. Instrum. **60**, 713 (1989).

[71] A. Schults, H.W. Crue, and R.N. Zare, J. Chem. Phys. **57**, 1354 (1972).

[72] W. Demtroder, Laser Spectroscopy, Springer, Berlin, 1982.

[73] D. L. Andrews (Editor), Applied Laser Spectroscopy: Techniques, Instrumentation, and Applications, VCH, New York, 1992.

[74] E.B. Saloman, C.J. Sansonetti, J. Phys. Chem. Ref. Data **33**, 1113 (2004).

[75] J. Shinar, B. Dehner, B. J. Beaudry, and D. T. Peterson, Phys. Rev. B **37**, 2066 (1988).

[76] J. N. Huiberts, R. Griessen, J. H. Rector, R. J. Wijngaarden, J. P. Dekker, D. G. de Groot, and N. J. Koeman, Nature (London) **380**, 231 (1996).

[77] C. Rao and J. Gopalakrishanan, New Directions in solid state Chemistry, CUP, London, 3rd edition ,1986.

[78] A.J. Sauval, Astron. Astrophys. **62,** 295 (1978).

[79] M. Grunze, Synthesis and decomposition of ammonia, in: D.A. King and D.P. Woodruff (Eds.), The Chemical Physics of Solid Surfaces and Heterogeneous Catalysis, Vol. 4, Elsevier, New York, 1982, pp.143–194.

[80] F.A. Cotton, G. Wilkinson, Advanced Inorganic Chemistry, A comprehensive Text, fifth ed.,Wiley, NewYork, 1988

[81] M. B. Airola and M. D. Morse, J. Chem. Phys. **116**, 1313 (2002).

[82] A. M. James, P. Kowalczyk, B. Simard, J. C. Pinegar, and M. D. Morse, J. Mol. Spectrosc. **168**, 248 (1994).

[83] A. Bernard and R. Bacis, Can. J. Phys. **54,** 1509 (1976).

[84] B. Simard, S.A. Mitchell, M.R. Humphries, and P.A. Hackett, J. Mol. Spectrosc. **129,** 186 (1988).

[85] K.K. Das, K. Balasubramanian, Chem. Phys. Lett. **172,** 372 (1990).

[86] R.S. Ram, P.F. Bernath, J. Chem. Phys. **104,** 6444 (1996).

[87] R.S. Ram, P.F. Bernath, J. Chem. Phys. **101,** 9283 (1994).

[88] H. Schall, M. Dulick, and R.W. Field, J. Chem. Phys. **87,** 2898 (1987).

[89] L.A. Kaledin, J.E. McCord, and M.C. Heaven, J. Opt. Soc. Am. B **11**, 219 (1994).

[90] A. Bernard, J. Chevillard, J. Mol. Spectrosc. **208,** 150 (2001).

[91] S. Koseki, Y. Ishihara, D.G. Fedorov, H. Umeda, M.W. Schmidt, and M.S. Gordon, J. Phys. Chem. A **108,** 4707 (2004).

[92] S. Mahmoud and M. Korek, Can. J. Phys. **92,** 855 (2014).

[93] S.G. Wang and W.H.E. Schwarz, J. Phys. Chem. **99,** 11687 (1995).

[94] C. Wittborn and U. Wahlgren, Chem. Phys. **201,** 357 (1995).

[95] W. Küchle, M. Dolg, and H. Stoll, J. Phys. Chem. A **101,** 7128 (1997).

[96] J.K. Laerdahl, K. Fægri, Jr., L. Visscher, and T. Saue, J. Chem. Phys. **109,** 10806 (1998).

[97] M. Casarrubios, L. Seijo, J. Chem. Phys. **110,** 784 (1999).

[98] G. Hong, M. Dolg, and L. Li, Chem. Phys. Lett. **334,** 396 (2001).

[99] R.S. Ram, P.F. Bernath, J. Chem. Phys. **105,** 2668 (1996).

[100] R.S. Ram, P.F. Bernath, J. Mol. Spectrosc. **183,** 263 (1997).

[101] Z.J. Jakubek, S.G. Nakhate, B. Simard, and W.J. Balfour, J. Mol. Spectrosc. **211,** 135 (2002).

[102] Z.J. Jakubek. B. Simard, and W.J. Balfour, Chem. Phys. Lett. **351**, 365 (2002).

[103] R.S. Ram, G. Li, and P.F. Bernath, J. Chem. Phys. **135**, 194308 (2011).

[104] W. F. Meggers, C.H. Corliss, and B.F. Scribner, Tables of Spectral Line Intensities, Part-I-Arranged by Elements, Monograph No. 145, Washington, DC: NBS, 1975, pp. 128-133.

[105] S.G. Fougère, W.J. Balfour, J. Cao, and C.X.W. Qian, J. Mol. Spectrosc. **199,** 18 (2000).

[106] Western CM. PGOPHER, a program for simulating rotational structure, University of Bristol.2010; http://pgopher.chm.bris.ac.uk.

[107] J. Anglada, P.J. Bruna, and S.D. Peyerimhoff, Mol. Phys. **66,** 541 (1989).

[108] M. Grau, A. E. Leanhardt, H. Loh, L. C. Sinclair, R. P. Stutz, T. S. Yahn, and E. A. Cornell, J. Mol. Spectrosc. **272**, 32 (2012).

[109] X. Wang, G. V. Chertihin, and L. Andrews, J. Phys. Chem. A **106**, 9213 (2002).

[110] A. B. Kunz, M. P. Guse, and R. J. Blint, J. Phys. B **8**, L358 (1975).

[111] C. W. Bauschlicher, Jr. and S. P. Walch, J. Chem. Phys. **76,** 4560 (1982).

[112] J. Anglada, P. J. Bruna, S. D. Peyerimhoff, and R. J. Buenker, J. Mol. Struct. **93,** 299 (1983)

[113] P. J. Bruna and J. Anglada, Quantum Chemistry: The Challenge of Transition metals and Coordination Chemistry (A. Veillard, Ed.),p. 67, Reidel, Dordrecht, 1986.

[114] A. Kant and K.A. Moon, High Temp. Sci., **14**, 23 (1981).

[115] A. Le and T.C. Steimle, J. Phys. Chem. A**115**, 9370 (2011).

[116] H. Machara and Y.Y. Yamashita, Pub. Astron. Soc. Jpn **28,** 135 (1976).

[117] D.L. Lambert and R.E.S. Clegg, Mon. Not. R. Astron. Soc. **191,** 367 (1980).

[118] B. Lindgren and G. Olofsson, Astron. Astrophys. **84,** 300 (1980).

[119] O. Engvold, H. Wohl and J.W. Brault, Astron. Astrophys. Suppl. Ser. **42,** 209 (1980).

[120] R.S. Ram and P.F. Bernath, J. Chem. Phys. **96,** 6344 (1992).

[121] T.M. Dunn, L.K. Hanson, and K.A. Rubinson, Can. J. Phys. **48,** 1657 (1970).

[122] J.K. Bates, N.L. Ranieri, and T.M. Dunn, Can. J. Phys. **54,** 915 (1976).

[123] A.E. Douglas and P.M. Veillette, J. Chem. Phys. **72,** 5378 (1980).

[124] C. Athe´nour and J.-L. Fe´me´nias, Can. J. Phys. **60,** 109 (1982).

[125] K. Brabaharan, J.A. Coxon, and A.B. Yamashita, Can. J. Phys. **63,** 997 (1985).

[126] B. Simard, H. Niki, and P.A. Hackett, J. Chem. Phys. **92,** 7012 (1990).

[127] D.A. Fletcher, C.T. Scurlock, K.Y. Jung, and T.C. Steimle, J. Chem. Phys. **99,** 4288 (1993).

[128] B. Simard, C. Masoni, and P.A. Hackett, J. Mol. Spectrosc. **136,** 44 (1989).

[129] S.L. Peter and T.M. Dunn, J. Chem. Phys. **90,** 5333 (1989).

[130] W.J. Balfour, A.J. Merer, H. Niki, B. Simard, and P.A. Hackett, J. Chem. Phys. **99,** 3288 (1993).

[131] T.C. Steimle, J.S. Robinson, and D. Goodridge, J. Chem. Phys. **110,** 881 (1999).

[132] W.J. Balfour, C.X.W. Qian, and C. Zhou, J. Chem. Phys. **106,** 4383 (1997).

[133] C. Zhou, W.J. Balfour, and C.X.W. Qian, J. Chem. Phys. **107,** 4473 (1997).

[134] K. Aiuchi, and K. Shibuya, J. Mol. Spectrosc. **204,** 235 (2000).

[135] R.S. Ram and P.F. Bernath, J. Mol. Spectrosc. **165,** 97 (1994).

[136] H. Li, C.M.T. Chan and A.S.C. Cheung, J. Mol .Spectrosc. **176**, 219 (1996).

[137] C.M.T. Chan, H. Li, N.S.K. Sze and A.S.C. Cheung, J. Mol. Spectrosc. **180**, 145 (1996).

[138] C.M.T. Chan, H. Li and A.S.C. Cheung, Chem .Phys .Lett. **269**, 49 (1997).

[139] H. Jiang, C. Ma and A.S.C. Cheung, Chem. Phys. Lett. **295**, 535 (1998).

[140] A.S.C. Cheung, H. Li and H. Jiang, Chen, J. Mol. Spectrosc. **210**, 84 (2001).

[141] H. Chen,Y. Li, D.K.W. Mok and A.S.C. Cheung, J. Mol. Spectrosc. **218**, 213 (2003).

[142] H. Jiang, Q. Shi and A.S.C. Cheung, J .Mol. Spectrosc. **200**, 283 (2000).

[143] R.S. Ram and P.F. Bernath, J. Mol. Spectrosc. **201,** 267 (2000).

[144] R.S. Ram and P.F. Bernath, J. Mol. Spectrosc. **243,** 62 (2007).

[145] R.C. Carlson, J.K. Bates and T.M. Dunn, J. Mol. Spectrosc. **110**, 215 (1985).

[146] A.B. Berezin, S.A. Dmitruk and D.I. Kataev, Opt. Spectrosc. (USSR) **68**, 310 (1990).

[147] D.A. Fletcher, K.Y. Jung and T.C. Steimle, J. Chem. Phys. **99**, 901 (1993).

[148] K.Y. Jung, D.A. Fletcher and T.C. Steimle, J. Mol. Spectrosc. **165**, 448 (1994).

[149] A. S-K. Sze and A.S-C. Cheung, J. Mol. Spectrosc. **173,** 194 (1995).

[150] R.S. Ram, J. Lievin, and P.F. Bernath, J. Chem. Phys. **109**, 6329 (1998).

[151] R.S. Ram and P.F. Bernath, J. Mol. Spectrosc. **213,** 170 (2002).

[152] R.S. Ram and P.F. Bernath, J. Mol. Spectrosc. **184,** 401 (1997).

[153] R.S. Ram. J. Lievin, and P.F. Bernath, J. Mol. Spectrosc. **215,** 275 (2002).

[154] R.S. Ram and P.F. Bernath, J. Opt. Soc. Am. B **11,** 225 (1994).

[155] W.J. Balfour. J. Cao, C.X.W. Qian, and S.J. Rixon, J. Mol. Spectrosc. **183,** 113 (1997).

[156] R.S. Ram, P.F. Bernath. and W.J. Balfour, J. Mol. Spectrosc. **246,** 192 (2007).

[157] R.S. Ram. J. Lievin, and P.F. Bernath. J. Chem. Phys. **111.** 3449 (1999)

[158] M.A. Garcia and M.D. Morse, J. Chem. Phys. **135**, 114304 (2011).

[159] R.S. Ram. J. Lievin, and P.F. Bernath, J. Mol. Spectrosc. **197,** 133 (1999).

[160] A.J. Marr, M.FI Flores, and T.C. Steimle, J. Chem. Phys. **104,** 8183 (1996).

[161] T.C. Steimle. A.J. Marr. S.A. Beaton, and J.M. Brown, J. Chem. Phys. **106,** 2073 (1997).

[162] B.J. Friedman-Hill and R.W. F'ield, J. Chem. Phys. **100,** 6141 (1994).

[163] T.C. Steimle. K.Y. Jung, and B.-Z. Li, J. Chem. Phys. **103,** 1767 (1995).

[164] S.T. Oyama, The Chemistry of Transition Metal Carbides and Nitrides; Oyama, S. T., Ed.; Blakie Academic and Professional: London, 1996.

[165] H.A. Pierson, Handbbok of Refractory Carbides and Nitrides; Noyes: Westwood, NJ, 1996.

[166] B.H. Weiller, J. Am. Chem. Soc. **118**, 4975 (1996).

[167] T.R. Cundari and Y. Li, Int. J. Quantum Chem. **55**, 315 (1995).

[168] J. Ha¨glund, A. Fernandez-Guillermet, G. Grimvall, and M. Ko¨rling, Phys. Rev. B **48**, 11685 (1993).

[169] B. V. Reddy and S. N. Khanna, Phys. Rev. B **54**, 2240 (1996).

[170] F.H . Mei, N. Shao, L. Wei, Y.S. Dong and G.Y. Li, Appl. Phys. Lett. **87**, 011906 (2005).

[171] M. Hock, E. Schäffer, W. Döll and G. Kleer, Surf. Coat. Tech. **689**, 163 (2003).

[172] D.J. Li, M.X. Wang and J.J. Zhang, Mater. Sci. Eng. A **116**, 423 (2006).

[173] C.H. Hsu, M.L. Chen and K.L. Lai, Mater. Sci. Eng. A **182**, 421 (2006).

[174] C. E. Kennedy**,** 14th Biennial CSP Solar PACES (Solar Power and Chemical Energy Systems) Symposium, 4-7 March 2008, Las Vegas, Nevada (CD-ROM) (NREL/CD-550-42709).

[175] M.J. Winter, d-Block Chemistry, Oxford University Press, New York, 1994.

[176] J.K. Bates and T.M. Dunn, Can. J. Phys. **54**, 1216 (1976).

[177] J.K. Bates and D.M. Gruen, High. Temp. Sci. **18**, 27 (1978).

[178] E.N. Moskvitina and Y.Y. Kuzyakov, Moscow University Chemistry Bulletin **65**, 315 (2010).

[179] A. Farhat, M. Korek, M.A.L. Marques and S.N. Abdul-Al, Can. J. Chem. **90**, 631 (2012).

[180] W.J. Childs, O. Poulsen and T.C. Steimle, J. Chem. Phys. **88**, 598 (1988).

---

[181] A. Adams, W. Klemperer and T.M. Dunn, Can. J. Phys. **46**, 2213 (1968).

[182] L.A. Akerlind, Ark. Fys. **22**, 41(1962).

[183] R. Stringat, C. Athénour and J.-L. Féménias, Can. J. Phys. **50**, 395 (1972).

[184] S. Huzinaga, M. Klobukowski and Y. Sakai, J. Phys. Chem. **88**, 4880 (1984).

[185] W.F. Meggers, C.H. Corliss and B.F. Scribner, Tables of spectral line intensities, Part1-Arranged by elements, Monograph No. 145 Washington DC NBS. 378 (1975).

[186] E. A. Den Hartog, K. A. Bilty and J.E. Lawler, J.Phys. B: At. Mol. Opt. Phys. **44**, 055001 (2011).

[187] J. E. Lawler, "Laser and Fourier transform techniques for the measurement of atomic transition probabilities," in Lasers, Spectroscopy and New Ideas: A Tribute to Arthur L. Schawlow, W.M. Yen and M.D. Levenson, eds., Vol. 54 of Springer Series in Optical Sciences (Springer, New York, 1988), pp. 125-140.

[188] C. Sneden and J.E. Lawler, J.J. Cowan, Phys. Scr. **T 100**, 15 (2002).

[189] E. Biémont and P.Quinet, Phys. Scr. **T 105**, 38 (2003).

[190] G.W. Wahlgren, Phys. Scr. **T 100**, 22 (2002).

[191] C. Sneden, Astrophys. J. **533**, L139 (2000).

[192] J. Westin, C. Sneden, B. Gustafsson and J.J. Cowan, Astrophys. J. **530**, 783 (2000).

[193] J.J. Cowan, Astrophys. J. **572**, 861 (2002).

[194] C. H. Corliss and W. R. Bozman, Experimental Transition Probabilities for Spectral lines of Seventy Elements, Vol. 53 of U.S. National Bureau of Standards Monograph (U.S. Government Printing Office, 1962), pp. 168-173.

[195] A. Hese, Z. Phys. **236**, 42 (1970).

[196] A. Hese and H.P. Weise, Z. Angew. Phys. **30**, 170 (1970).

[197] A. Hese and G. Büldt, Z. Naturforsch. A **25**, 1537 (1970).

[198] B. R. Bulos, A. J. Glassman, R. Gupta, and G. W. Moe, J. Opt. Soc. Am. **68**, 842 (1978).

[199] N. P. Penkin, V. N. Gorshkov, and V. A. Komarovskii, Opt. Spectrosc. **58**, 840 (1985).

[200] K. B. Blagoev, and V. A. Komarovskii, At. Data Nucl. Data Tables **56**, 1 (1994).

[201] P. S. Doidge, Spectrochim. Acta B **50**, 209 (1995).

[202] E. Biémont, P. Quinet, S. Svanberg, and H.L. Xu, Eur. Phys. J. D **30**, 157 (2004).

[203] B. Karaçoban, and L. Özdemir, Acta Physica Polonica A **113**, 1609 (2008).

[204] Y. Feng, W. Zhang, B. Kuang, L. Ning, Z. Jiang, and Z. Dai, J. Opt. Soc. Am. B **28**, 543 (2011).

[205] Z. -S. Li, J. Norin, A. Persson, C. -G. Wahlström, and S. Svanberg, Phys. Rev. A **60**, 198 (1999).

[206] B. Meng, J. Quant.Spectrosc. Radiat.Transfer. **41**, 303 (1989).

[207] Y.Feng , Q. Wang, L. Jiang, Z. Jiang, and Z.Dai, Eur. Phys. J. D **65**, 299 (2011).

[208] X. Shang, Y.Tian, Q.Wang, S. Fan, W. Bai, and Z. Dai, Mon. Not. R. Astron. Soc. **442**, 138 (2014).

[209] W. C. Martin, R. Zalubas, and L. Hagan, Atomic Energy Levels-The Rare-Earth Elements, Vol. 60 of National Standard Reference Data Series, National Bureau of Standards (U.S. Department of Commerce, National Bureau of Standards, 1978), pp. 27-35.

[210] S. G. Nakhate, S. Mukund and S. Bhattacharyya, J. Quant. Spectrosc. Radiat.Transfer. **111**, 394 (2010).

[211] Gü. Başar, Gö. Başar, and S. Kröger, Opt. Commun. **282**, 562 (2009).

[212] P. Hannaford, and R.M. Lowe, Opt. Eng. **22**, 532 (1983).

APPENDIX A

Table A1: Observed rotational line positions (in cm^{-1}) in the (0-0) band of $0^+(^3\Sigma^-)$-$X^1\Sigma^+$ system of LaH

J	*R(J)*	*O-C* [†]	*P(J)*	*O-C*
0	15630.32	-0.01		
1	15637.15	0.02	15614.82	0.04
2	15643.19	0.01	15606.07	-0.01
3	15648.32	-0.02	15596.65	-0.08
4	15652.26*	-0.18	15586.69	0.05
5	15653.21*	-2.04	15575.69	0.00
6			15563.47*	-0.23
			15558.10[P]	
7			15548.21*	-2.25
			15544.32[P]	
8			15531.00*	-4.72

[†] observed minus calculated wavenumbers.

*Perturbed lines excluded from the fit.

[P] Perturber.

Table A2: Observed rotational line positions (in cm^{-1}) in the (0-0) band of $D^1\Pi$-$X^1\Sigma^+$ system of LaH

J	*R(J)*	*O-C*	*Q(J)*	*O-C*	*P(J)*	*O-C*
0	17405.69	0.08				
1	17412.80	-0.06	17397.58	0.12		
2	17419.61	-0.05	17396.57	0.04	17381.45	0.09
3	17425.97	-0.01	17395.08	0.00	17372.45	-0.01
4	17431.79	0.01	17393.04	-0.07	17363.05	-0.07
5	17436.95	-0.05	17390.48	-0.10	17353.32	-0.01
6	17441.61	0.02	17387.34	-0.09	17343.05	0.01
7	17445.51	0.04	17383.58	-0.03	17332.22	0.01
8	17448.65	0.08	17379.07	0.03	17320.80	0.01
9	17450.71	-0.08	17373.70	0.03	17309.01*	0.30
10	17452.09	0.06	17368.79*	1.40	17296.18*	0.27
			17366.35^{P}			
11	17452.21	0.02	17360.72*	0.60		
12			17352.46*	0.80		
13	17448.68	-0.05	17342.09	0.02		

*Perturbed lines excluded from the fit.
^{P}Perturber.

Table A3: Observed rotational line positions (in cm^{-1}) in the (0-0) band of $E^1\Pi$-$X^1\Sigma^+$ system of LaH†

J	*R(J)*	*O-C*	*Q(J)*	*O-C*	*P(J)*	*O-C*
0	17556.58	-0.01				
1	17563.73	0.13	17548.87*	0.38		
2	17570.14	0.06	17547.68*	0.29	17532.20	-0.14
3	17576.10	0.04	17545.96	0.20	17523.42	0.22
4	17581.45	-0.13	17543.70	0.08	17513.41	-0.13
5	17586.56	-0.10	17540.99	-0.02	17503.29	-0.12
6	17591.34	0.00	17537.96	0.00	17492.72	-0.12
7	17595.86	0.13	17534.52	-0.02	17481.69	-0.20
8	17599.96	0.13	17530.81	0.01	17470.34	-0.22
9	17603.71	-0.04	17526.86	0.05	17459.17	0.20
10	17607.27	-0.27	17522.56	-0.07	17447.30	0.13
11	17610.45*	-0.87	17517.79*	-0.57	17435.31	0.08
12			17512.52*	-1.56	17423.14	-0.11
13					17410.40*	-0.92

*Perturbed lines excluded from the fit.

†Extra lines having longer lifetimes observed at 17549.20, 17545.57, 17440.31, 17532.62, 17529.30, 17515.93, 17507.55 and 17506.16 cm^{-1}.

Table A4: Observed rotational line positions (in cm^{-1}) in the (0-0) band of 18509 cm^{-1} system of LaH

J	*R(J)*	*O-C*	*Q(J)* *	*O-C*	*P(J)*	*O-C*
1	18523.71	0.09	18508.66	-0.06	18501.20	-0.05
2	18530.90	-0.13	18508.66	0.02	18493.67	0.05
3	18538.57	0.05	18508.66	0.05	18485.98	0.04
4	18546.07	-0.02	18508.66	-0.03	18478.18	-0.10
5	18553.64	0.03			18470.80	0.10
6					18463.19	-0.01
7					-	-
8					18447.62	-0.09
9					18438.72	0.03

**Q* branch members not resolved.

Table A5: Observed rotational line positions (in cm^{-1}) in the ((0-0) band of [20.0]Ω = 1- $X^1\Sigma^+$ system of LaH

J	*R(J)*	*O-C*	*Q(J)*	*O-C*	*P(J)*	*O-C*
0	20049.807	0.0233				
1	20057.379	0.0444	20041.844	0.0268		
2	20064.59	-0.0217	20041.547	0.0273	20025.592	0.0545
3	20071.591	-0.0176	20041.053	-0.0133	20016.91	-0.0249
4	20078.346	0.0283	20040.41	-0.0388	20008.036	-0.0387
5	20084.721	-0.0091	20039.619	-0.0368	19998.974	0.0173
6	20090.808	-0.0279	20038.582	-0.0912	19989.576	-0.0036
7	20096.672	0.0477	20036.111	0.0424	19979.933	-0.0082
8	20102.092	0.0091	20034.431	0.0267	19969.973	-0.0647
9	20107.216	0.0175	20032.504	0.0386	19959.851	-0.0136
10	20111.944	-0.0125	20030.233	0.0095	19949.476	0.0600
11	20116.32	-0.0212	20027.616	-0.0313	19938.706	0.0214
12	20120.31	-0.0257	20024.704	0.0016	19927.686	0.0237
13	20123.892	-0.0296	20021.348	-0.0034	19916.321	-0.0185
14	20127.04	-0.0397	20041.844	0.0268	19904.66	-0.0452
15					19892.817	0.0696
16					19880.50	0.0475

Table A6: Observed rotational line positions (in cm^{-1}) in the (1-1) band of [20.0]Ω = 1- $X^1\Sigma^+$ system of LaH

J	*R(J)*	*O-C*	*Q(J)*	*O-C*	*P(J)*	*O-C*
0	19979.6670	0.0035				
1	19987.0680	0.0234	19971.7890	-0.0162		
2	19994.1510	0.0099	19971.3960	-0.0054	19955.8800	-0.0016
3	20000.9930	0.0509	19970.8070	0.0177	19947.4190	0.0001
4	20007.3460	-0.0885	19969.9230	-0.0385	19938.7060	0.0186
5	20013.5070	-0.0954	19968.8930	-0.0148	19929.7070	0.0240
6			19967.5680	-0.0479	-	-
7			19966.1940	0.1236	19910.7500	-0.0751
8			19964.2310	-0.0230	19901.0520	0.1015
9			19962.1220	-0.0243	19890.9180	0.1577

Table A7: Observed rotational line positions (in cm^{-1}) in the (0-0) band of [21.9]Ω = 0^+- $X^1\Sigma^+$ system of LaH

J	*R(J)*	*O-C*	*P(J)*	*O-C*
0	21977.72	-0.003		
1	21983.67	-0.0122	21962.65	0.0194
2	21988.62	0.0118	21953.49	0.0082
3	21992.52	-0.0138	21943.27	-0.0136
4	21995.55	0.024	21932.03	-0.0362
5	21997.59	-0.0456	21919.90	0.0191
6	21998.96	0.0105	21906.82	0.031
7			21891.51	0.024

Table A8: Observed rotational line positions (in cm^{-1}) in the (0-0) band of [22.1]Ω = 0^{+}- $X^{1}\Sigma^{+}$ system of LaH

J	*R(J)*	*O-C*	*P(J)*	*O-C*
0	22106.96	0.0437		
1	22112.10	-0.0462	22092.32	0.0878
2	22116.18	-0.0505	22082.67	0.0059
3	22119.45	0.027	22071.69	-0.0586
4	22122.07	0.0898	22059.60	-0.0915
5	22124.11	0.0423	22046.75	-0.0201
6	-	-	22033.25	0.0148
7	22127.12	0.0011	22019.29	0.0111
8	22128.01	0.0113	-	-
9	22128.62	0.093	21990.30	-0.0552
10	22129.28	0.0371	21975.25	-0.0768
11			21960.00	-0.0042
12			21944.89	-0.0618

APPENDIX B

Table B1: Observed rotational line positions (in cm^{-1}) of the $B^2\Sigma^+$–$X^2\Sigma^+$ (1, 0) band of ^{90}ZrN

J	$P_2(J)$	*O-C*	$P_1(J)$	*O-C*	$R_2(J)$	*O-C*	$R_1(J)$	*O-C*
0.5					25548.557	-0.0024	25547.588	-0.017
1.5	25544.585	-0.209	25545.694	-0.075	25549.461	0.1001	25548.360	-0.054
2.5	25543.64	-0.088	25544.585	-0.125	25550.222	0.1239	25548.988	-0.170
3.5	25542.567	-0.031	25543.421	-0.167	25550.886	0.115	25549.932	0.0940
4.5	25541.413	0.0091	25542.250	-0.150	25551.471	0.0912	25550.563	0.1093
5.5	25540.199	0.0534	25541.023	-0.126	25552.014	0.0896	25551.044	0.0388
6.5	25538.843	0.0197	25539.771	-0.062	25552.409	0.0041	25551.501	0.0084
7.5	25537.479	0.0421	25538.452	-0.002	25552.968	0.1466	25552.014	0.0981
8.5	25536.038	0.0514	25537.029	0.0187	25553.275	0.101	25552.328	0.0528
9.5	25534.497	0.0245	25535.595	0.0923	25553.524	0.0612	25552.510	-0.061
10.5	25532.948	0.0534	25534.026	0.0946	25553.585	-0.1029	25552.968	0.1658
11.5	25531.247	-0.006	25532.417	0.1206	25553.842	-0.0074	25552.995	0.0250
12.5	25529.457	-0.091	25530.614	0.0163	25553.962	0.0145	25552.517	-0.557
13.5	25527.695	-0.085	25528.671	-0.165	25553.962	-0.0202	25552.966	-0.149
14.5	25525.869	-0.080	25526.597	-0.413			25552.966	-0.127
15.5	25523.996	-0.058	25525.226	0.1044				
16.5			25523.262	0.0920				

Table B2: Observed rotational line positions (in cm^{-1}) of the $B^2\Sigma^+$–$X^2\Sigma^+$ (2, 0) band of ^{90}ZrN

J	$P_2(J)$	*O-C*	$P_1(J)$	*O-C*	$R_2(J)$	*O-C*	$R_1(J)$	*O-C*
0.5					26426.341	-0.0486	26425.223	-0.1840
1.5	26422.565	-0.0571	26423.487	-0.0963	26427.256	0.0665	26426.187	-0.0127
2.5	26421.529	-0.0293	26422.419	-0.0933	26428.057	0.1354	26426.901	-0.0236
3.5	26420.399	-0.0277	26421.279	-0.0945	26428.547	-0.039	26427.590	0.0083
4.5	26419.26	0.0325	26420.084	-0.0830	26429.399	0.2164	26428.217	0.0459
5.5	26418.028	0.0674	26418.822	-0.0708	26429.710	-0.0017	26428.747	0.0541
6.5	26416.716	0.0899	26417.525	-0.0259	26430.170	-0.0032	26429.287	0.1400
7.5	26415.326	0.1018	26416.087	-0.0545	26430.493	-0.0742	26429.399	-0.1345
8.5	26413.888	0.1331	26414.626	-0.0386	26430.952	0.0583	26429.790	-0.0625
9.5	26412.358	0.1398	26413.083	-0.0373	26431.099	-0.054	26430.037	-0.0671
10.5	26410.659	0.0447	26411.488	-0.0207	26430.753*	-0.5921	26430.493	0.2045
11.5	26408.884	-0.0594	26409.783	-0.0469	26430.973*	-0.4971	26430.480	0.0744
12.5	26406.729*	-0.4765	26408.110	0.0260	26430.973*	-0.5552		
13.5	26404.930*	-0.4708	26406.320	0.0488				
14.5	26402.883*	-0.6465	26404.526	0.1345				
15.5	26401.099*	-0.4927	26402.866*	0.4208				
16.5	26399.245*	-0.3425	26401.099*	0.6665				
17.5	26397.203*	-0.3142	26397.366*	-0.9874				
18.5	26395.204	-0.1770	26395.468*	-0.7401				
19.5	26393.100	-0.0791	26393.405*	-0.5919				
20.5	26390.899	-0.0126	26391.275*	-0.4450				
21.5	26388.540	-0.0389	26389.089*	-0.2886				
22.5	26386.179	-0.0021	26386.805	-0.1649				
23.5	26383.735	0.0165	26384.472	-0.0252				
24.5	26381.225	0.0337	26382.095	0.1354				
25.5	26378.633	0.0330	26379.690*	0.3324				

* Perturbed lines not included in the fit.

Table B3: Observed rotational line positions (in cm^{-1}) of the $B^2\Sigma^+$–$X^2\Sigma^+$ (2, 1) band of ^{90}ZrN

J	$P_2(J)$	*O-C*	$P_1(J)$	*O-C*
1.5	25428.312	-0.0502	25429.301	0.0105
2.5	25427.318	-0.0077	25428.213	-0.0056
3.5	25426.242	0.0149	25427.001	-0.0837
4.5	25425.081	0.0145	25425.898	0.0092
5.5	25423.889	0.0451	25424.666	0.0352
6.5	25422.620	0.0605	25423.309	-0.0019
7.5	25421.181	-0.0323	25421.969	0.0398
8.5	25419.811	0.0057	25420.484	-0.0016
9.5	25418.296	-0.0398	25419.007	0.0267
10.5			25417.367	-0.0464
11.5			25415.773	-0.0119
12.5			25414.114	0.0189

Table B4: Observed rotational line positions (in cm^{-1}) of the $B^2\Sigma^+–X^2\Sigma^+$ (2, 3) band of ^{90}ZrN

J	$P_1(J)$	*O-C*	$P_2(J)$	*O-C*	$R_1(J)$	*O-C*	$R_2(J)$	*O-C*
0.5					23463.87	0.05	23464.8	-0.01
1.5	23462.07	0.05	23461.13	0.11	23464.72	0.06	23465.68	0.03
2.5	23461.13	0.13	23460.09	0.09	23465.42	-0.03	–	–
3.5	23460.09	0.16	23458.9	-0.03	23466.04	-0.15	–	–
4.5	23458.90	0.08	23457.72	-0.08	–	–	23467.86	-0.02
5.5	23457.68	0.03	–	–	–	–	23468.41	-0.12
6.5	23456.46	0.03	23455.3	-0.12	–	–	–	–
7.5	23455.17	-0.01	–	–	–	–	23469.7	0.01
8.5	23453.83	-0.05	23452.86	0.00	–	–	23470.13	-0.07
9.5	23452.47	-0.06	23451.38	-0.13	23469.70	0.02		
10.5	23451.04	-0.09	–	–	23470.13	0.03		
11.5	23449.68	0.00	–	–				
12.5	23448.19	0.00	23447.12	-0.04				
13.5	23446.64	-0.01	–	–				
14.5	–	–	–	–				
15.5	23443.54	0.11	–	–				
16.5	23441.78	0.02	23440.53	-0.20				
17.5	23440.04	0.01	23438.79	-0.21				
18.5	23438.29	0.03	23437.12	-0.11				
19.5	23436.48	0.04	23435.33	-0.07				
20.5	23434.65	0.08	23433.58	0.05				
21.5	23432.76	0.10	23431.69	0.07				
22.5	23430.78	0.08	23429.72	0.06				
23.5	23428.72	0.03	23427.71	0.06				
24.5	23426.61	-0.03	23425.7	0.10				
25.5	23424.41	-0.13	23423.54	0.05				
26.5	23422.13	-0.26	23421.51	0.16				

Table B5: Observed rotational line positions (in cm^{-1}) of the $A^2\Pi_{3/2}$–$X^2\Sigma^+$ (3, 3) band of ^{90}ZrN

J	$R_2(J)[Q_{21}(J+1)]$	$O-C$	$P_2(J)$	$O-C$	$Q_2(J)[P_{21}(J+1)]$	$O-C$	$R_{21}(J)$	$O-C$
0.5	17554.536	-0.0863						
1.5	17555.024	-0.0628						
2.5	17555.463	-0.0842			17552.694	-0.0287	17558.435	0.0384
3.5	17555.905	-0.0985			17552.235	-0.0025	17559.812	0.0094
4.5	17556.367	-0.0885			17551.751	0.003	17561.274	0.0695
5.5	17556.852	-0.0515	17545.541	-0.0147	17551.266	0.0115	17562.673	0.0708
6.5	17557.240	-0.1072	17544.325	0.2168	17550.789	0.0322	17564.089	0.0932
7.5	17557.702	-0.0849	17542.845	0.1885	17550.278	0.0231	17565.487	0.1017
8.5	17558.107	-0.1154	17541.336	0.1353	17549.824	0.0751	17566.881	0.1105
9.5			17539.856	0.1153	17549.271	0.0323	17568.282	0.1303
10.5	17558.970	-0.1109	17538.333	0.0564	17548.779	0.0546	17569.635	0.1063
11.5	17559.378	-0.1259	17536.874	0.0656	17548.269	0.0631	17570.994	0.0925
12.5			17535.389	0.053	17547.725	0.0417	17572.435	0.1648
13.5			17533.854	-0.0054	17547.166	0.0094	17573.682	0.0473
14.5			17532.372	-0.0067	17546.648	0.0223		
15.5			17530.842	-0.0519	17546.084	-0.0066		
16.5			17529.297	-0.1079	17545.541	-0.0104		
17.5			17527.854	-0.0577	17544.948	-0.0601		

Table B6: Observed rotational line positions (in cm^{-1}) of the $A^2\Pi_{1/2e}$–$X^2\Sigma^+$ (3, 3) band of ^{90}ZrN

J	$R_1(J)$	*O-C*	$Q_{12}(J)[P_1(J+1)]$	*O-C*
0.5			16988.237	-0.1404
1.5			16987.813	-0.0755
2.5	16993.455	-0.0725	16987.372	-0.0174
3.5	16994.877	-0.0267	16986.863	-0.016
4.5	16996.206	-0.0589	16986.398	0.0423
5.5	16997.618	0.0096	16985.946	0.1288
6.5	16998.923	-0.0081	16985.341	0.0798
7.5	17000.237	0.0073	16984.780	0.0956
8.5	17001.475	-0.025	16984.120	0.0367
9.5	17002.842	0.1044	16983.496	0.0419
10.5	17003.896	-0.0416	16982.850	0.0579
11.5	17005.043	-0.0516	16982.100	0.0074
12.5	17006.164	-0.0387	16981.346	-0.004
13.5	17007.199	-0.0565	16980.464	-0.0945
14.5	17008.200	-0.0463	16979.713	0.0013
15.5	17009.162	-0.0057	16978.787	-0.0159
16.5	17010.011	-1E-3		
17.5	17010.759	-0.012		
18.5	17011.372	-0.0641		
19.5	17012.129	0.1311		

Table B7: Observed rotational line positions (in cm^{-1}) of the $A^2\Pi_{1/2f}$–$X^2\Sigma^+$ (3, 3) band of ^{90}ZrN

J	$P_{12}(J)$	O-C	$R_{12}(J)[Q_1(J+1)]$	O-C
0.5			16989.418	0.018
1.5			16989.817	0.0026
2.5			16990.152	-0.0523
3.5			16990.477	-0.0923
4.5			16990.752	-0.1569
5.5				
6.5	16978.787	0.2253		
7.5	16977.119	0.1432		
8.5				
9.5				
10.5				
11.5	16970.375	0.016		
12.5	16968.550	-0.0819		
13.5				
14.5	16965.111	0.0285		

Extra lines (in cm^{-1}) appeared in 1-0 band of the *B*-*X* transitions of ^{90}ZrN:

25545.47, 25545.29, 25544.02, 25542.93, 25541.96, 25541.75, 25540.78, 25540.57, 25539.57, 25539.04, 25537.95, 25537.77, 25536.44, 25535.12, 25534.98, 25533.60, 25533.43, 25533.14, 25531.91, 25530.13, 25527.44; Near Band Origin: 25546.97, 25546.18

Extra lines (in cm^{-1}) appeared in 2-0 band of the *B*-*X* transitions of ^{90}ZrN:

26416.33, 26415.57, 26414.97, 26414.44, 26414.22, 26412.59, 26411.87, 26411.18, 26407.56, 26407.25, 26406.30, 26405.99, 26405.58, 26403.95, 26403.45, 26402.22, 26401.75, 26400.53, 26400.09, 26398.68, 26398.36, 26396.82, 26396.51, 26394.85, 26394.66

List of publications included in the thesis

Journals:

1. “Radiative lifetime measurements in neutral lanthanum using time-resolved laser-induced fluorescence spectroscopy in supersonic free-jet”,

Suresh Yarlagadda, Sheo Mukund, S.G. Nakhate, *J. Opt. Soc. Am. B* **28** ,1928 (2011).

2. “Jet-cooled laser-induced fluorescence spectroscopy of LaH: Observation of new excited electronic states”,

Suresh Yarlagadda, Sheo Mukund, S.G. Nakhate, *Chem. Phys. Lett*. **537**, 1 (2012).

3. “Energy linkage between the singlet and triplet manifolds in LaH, and observation of new low-energy states”,

Sheo Mukund, **Suresh Yarlagadda**, Soumen Bhattacharyya, S. G. Nakhate, *J. Chem. Phys*. **137**, 234309 (2012).

4. “Observation of a new $\Omega = 1$ excited state in LaH”,

Suresh Yarlagadda, Sheo Mukund, Soumen Bhattacharyya, S.G. Nakhate, *J. Mol. Spectrosc*. **289**, 1 (2013).

5. “Observation of two $\Omega = 0^+$ excited states of jet cooled LaH”,

Suresh Yarlagadda, Sheo Mukund, Soumen Bhattacharyya, S.G. Nakhate, *J. Quant. Spectrosc. Radiat. Transfer*. **145**, 17 (2014).

6. “Extended analysis of the $B^2\Sigma^+$-$X^2\Sigma^+$ and $A^2\Pi$-$X^2\Sigma^+$ systems of ZrN”,

Soumen Bhattacharyya, Sheo Mukund, **Suresh Yarlagadda,** S.G. Nakhate, *J. Quant.Spectrosc. Radiat. Transfer*. **148**, 13 (2014).